Annulate Lamellae biogenesis is essential for nuclear pore function

Junyan Lin[1,2,3,4], Arantxa Agote-Arán[1,2,3,4,5], Yongrong Liao[1,2,3,4], Rafael Schoch [1,2,3,4,6], Paolo Ronchi[7], Victor Cochard[8], Rui Zhu[1,2,3,4,6], Charlotte Kleiss[1,2,3,4], Marc Ruff[1,2,3,4,6], Guillaume Chevreux[8], Yannick Schwab[7], Bruno P. Klaholz[1,2,3,4,6] and Izabela Sumara[1,2,3,4, *].

[1] Institute of Genetics and Molecular and Cellular Biology (IGBMC), Illkirch, France.
[2] Centre National de la Recherche Scientifique (CNRS), UMR 7104, Strasbourg, France.
[3] Institut National de la Santé et de la Recherche Médicale (INSERM), U964, Strasbourg, France.
[4] Université de Strasbourg, Strasbourg, France.
[5] Current address: Institute of Biochemistry, Department of Biology, ETH Zürich, Zürich, Switzerland.
[6] Centre for Integrative Biology (CBI), Illkirch, France.
[7] European Molecular Biology Laboratory, Electron Microscopy Core Facility, Heidelberg, Germany.
[8] Université Paris Cité, CNRS, Institut Jacques Monod, F-75013 Paris, France.

Contact: * To whom correspondence should be addressed: Izabela Sumara, Institute of Genetics and Molecular and Cellular Biology (IGBMC), Illkirch, France, Phone: +33 3 88 65 35 21, Fax: +33 3 88 65 32 01, Email: sumara@igbmc.fr

Abstract

Nuclear pore complexes (NPCs), large protein assemblies embedded into the nuclear envelope (NE), are crucial for bidirectional transport between the nucleus and cytoplasm, a process often disrupted in human diseases. Besides their presence within the NE, NPCs are also found in stacked cytoplasmic endoplasmic reticulum (ER) membranes called annulate lamellae (AL)[1,2]. Despite being discovered in the mid-20th century[3], the function and biogenesis mechanisms of AL have remained largely mysterious. While AL were thought to be restricted to germ, embryonic and malignant cells[4–12], we find that AL also exist in the cytoplasm of somatic cells under normal physiological conditions and that they can expand upon specific stimuli. We show that AL merge with the NE, supplying the nucleus with new pores which maintains nuclear pore function and nuclear growth during early interphase. NPC protein RanBP2 (Nup358) and ER-associated Climp63 (CKAP4) trigger AL assembly and their NE-integration. The N-terminal phenylalanine-glycine (FG) repeats of RanBP2 drive the oligomerization of Y-complexes (the NPC outer ring units), and AL-NPCs formation and Climp63 ensures the localization of AL-NPCs to ER sheets and their fusion with the nucleus. These findings uncover a fundamental mechanism of AL biogenesis and highlight the critical role of cytosolic NPCs in the nuclear function and mammalian cellular homeostasis.

Main

Annulate lamellae (AL) are specialized subdomains within the endoplasmic reticulum (ER), characterized by a variable array of parallel-arranged layers. These assemblies feature a regular distribution of pore structures embedded in the membranes, which closely resemble nuclear pore complexes (AL-NPCs)[1,2]. AL were commonly observed in rapidly developing, differentiating, and malignant cells[4–12] and cellular infections can lead to biogenesis of AL[13–22]. Despite their early discovery by McCullough in 1952[3] and designation by Swift in 1956[23], and subsequent reports suggesting the importance of AL in specific cell types[4,8,24–31], the universal function and direct biogenesis mechanisms of AL have remained enigmatic.

It can be hypothesized that AL might be utilized by rapidly growing cells or cells challenged with external or pathological stimuli to increase the pool of nuclear envelope (NE) NPCs (NE-NPCs) and sustain optimal levels of nucleocytoplasmic transport. This process is vital for normal cellular function, and abnormal expression or localization of nucleoporins (Nups), the building units of NPCs, have been observed in cancer and neurodegenerative disorders[32–35]. However, it is currently unknown if the Nups localization defects, often visualized by low-resolution microscopy techniques as foci or granules, are linked to the presence of AL and if they affect nuclear function. To address this gap and develop a means to study AL, alternative microscopy methods are urgently needed that can be easily applied to healthy and diseased cells. Given that many studies lack electron microscopy (EM) or structural analysis of Nups foci under stress and disease conditions[36–46], it is possible that, at least in some cases, pathological states could be characterized by accumulation of AL.

Single molecule localization microscopy identifies the presence of AL in a variety of normally proliferating mammalian cells

To determine whether cytoplasmic Nup foci represent AL, we used cellular models that have linked microtubules (MTs), fragile X-related proteins (FXRPs) (FXR1, FXR2 and FMRP), and ubiquitin-associated protein 2-like (UBAP2L) to aberrant Nup accumulation in the cytoplasm. Indeed, previous findings demonstrated an important role of dynein-mediated MT-based transport as well as chaperoning proteins FXRPs and UBAP2L in the localized assembly of Nups at the NE during interphase[35,47,48]. Nup foci were also seen in the context of human disease, the fragile-X syndrome (FXS)[35], characterized by the absence of FMRP.

As expected, acute MT depolymerization or deletion of UBAP2L in mCherry-Nup133 knock-in (KI) HeLa cells (Extended Data Fig. 1a-d) led to the formation of cytoplasmic mCherry-Nup133 foci that also contained Nup62 (Extended Data Fig. 1e). Correlative light and electron microscopy (CLEM) analysis showed these foci to be localized to parallel-aligned ER membrane structures containing stacked pore-like complexes, suggesting that they represent AL (Fig. 1a).

To overcome existing limitations in the microscopy analysis of AL, we utilized single molecule localization microscopy[49,50] (SMLM) to generate super-resolution images of the AL foci. In particular, we applied a multi-color variant based on a dichroic image splitter and spectral demixing (splitSMLM[51]). Via the simultaneous imaging of multiple species of fluorophores, the method enables high-precision observations of the structural

organization of NPCs and other multi-component complexes, reaching a resolution of 20 nm[51]. This approach is also easily applicable under various experimental conditions. We confirmed the presence of highly organized cytosolic assemblies containing tightly packed NPC structures, likely corresponding to AL identified by CLEM, upon disruption of the FXRPs-UBAP2L pathway (Fig. 1b, Extended Data Fig. 2a-c). Surprisingly, small AL containing fewer NPCs (on average 1,65) (Fig. 3i) could be observed in the cytoplasm of wild-type (WT) HeLa cells (Fig. 1b, Extended Data Fig. 2d) whereas in cells treated with nocodazole AL were larger (average 13,8 NPCs) (Fig. 3i). Small AL structures were also observed in normally proliferating human fibroblasts, while large AL were found in FXS patient-derived fibroblasts (Fig. 1c)

Accordingly, when imaged with conventional (diffraction-limited) fluorescence microscopy, AL-foci also appeared smaller for WT HeLa interphase cells (average size 0,0896 μm^2) compared to cells with depolymerized MTs (average size 0,2132 μm^2) (Extended Data Fig. 3a-b). We observed a relatively broad distribution range of AL foci sizes (Extended Data Fig. 3a-b) and the number of NPC complexes in a single AL-NPC structure (Fig. 3i) in both WT and nocodazole-treated cells, confirming the reported diversity of AL morphologies and distribution[52]. Hereinafter, AL foci that were considered “large” have a size bigger than 0,3 μm^2. Small and large AL foci were composed of most of the Nups, with the exception of the nuclear basket Nup153 and ELYS, under various analyzed conditions (Fig. 1d, Extended Data Fig. 3c-f), in accordance with findings in the Drosophila blastoderm embryo[8] and in Xenopus egg extracts[53,54]. Small and large AL foci could be detected in a variety of common cancer cell lines including U2OS, DLD-1, HCT116, and in the non-transformed cell line RPE-1 (Extended Data Fig. 4a-d). Nucleocytoplasmic transport factors Exportin-1, Importin β, and Ras-related nuclear protein (Ran) likewise localized to AL foci (Extended Data Fig. 5a), as previously reported[26], suggesting that the dynamics of AL may affect nucleocytoplasmic transport. NE-resident proteins SUN1 and SUN2, but not Lamin A, Lamin B1, Nesprin, Emerin, and Lap2β, co-localized with AL foci (Extended Data Fig. 5b).

The existence of small and large AL structures prompted us to investigate their dynamics. Spinning disk confocal live video microscopy of WT mEGFP-Nup107 Hela cell, synchronized in interphase, revealed a progressive increase in size and fusion of AL foci over time following MT depolymerization by nocodazole (Fig. 1e and Supplementary Video 1). Similar fusion events were observed upon depletion of FXR1 or in UBAP2L knockout (KO) cells (Extended Data Fig. 6a, b). These fusion events are in agreement with our data on a broad distribution range of AL foci sizes detected by fluorescence microscopy, small and large NPCs clusters observed by splitSMLM analysis, and by CLEM results which likewise demonstrated existence of both small (containing a single ER membrane) and larger AL structures (Fig. 1a). Collectively, these results demonstrate that unexpectedly, the existence of AL is widespread in normally proliferating mammalian cells and that small AL present in WT cells become bigger when exposed to specific stimuli or in pathological states.

AL merge with NE in early interphase under normal growth conditions

NE-NPC density can be modulated in proliferating cells and increases in growing

128 interphase nuclei during the G1 and S phases[55]. We thus examined the abundance of AL
129 structures during different cell cycle stages. Analysis of phosphorylated retinoblastoma (p-
130 Rb) (G1/S phase transition marker) and cyclin B (G2 marker) revealed that small AL foci
131 are present throughout interphase, but predominantly in the G1 and S phases (Fig. 2a, b,
132 Extended Data Fig. 7a-d), similar to the pattern of the NE-NPCs. Large AL foci induced by
133 acute MT depolymerization followed the same cell cycle distribution tendency (Extended
134 Data Fig. 7e-j). To understand the fate of AL foci during early interphase of WT cells, we
135 followed their dynamics by spinning disk confocal live video microscopy and found a
136 tendency for them to migrate towards and merge with the NE (Fig. 2c and Supplementary
137 Video 2). In contrast, cells with disrupted MTs displayed growing AL foci through fusion
138 events that remained in the cellular periphery (Supplementary Video 1, Fig.1d, Extended
139 Data Fig. 11d).
140 Given that cytosolic ER membranes are continuous with the outer NE and contribute to its
141 formation[56], and that AL are specialized sub-compartments of the ER, it was important to
142 demonstrate if the observed GFP-Nup107-positive AL foci localize to ER membranes.
143 Spinning disk confocal live video microscopy of the ER marker mScarlet-ER confirmed that
144 small AL foci move along the ER to merge with the NE in WT interphase cells (Fig. 2d and
145 Supplementary Video 3). MT depolymerization induced fusion events of AL foci on ER
146 membranes, as shown above (Supplementary Video 1, Fig.1d), and AL foci lost their
147 tendency to integrate with the NE (Fig 2e, Extended Data Fig. 8a). MT depolymerization is
148 predicted to modulate ER dynamics[57], damaging reticulated ER tubules and leading to
149 vesiculation and thickening of cisternal sheets (Extended Data Fig. 8b), which could
150 explain the inhibition of AL foci integration into the NE in nocodazole-treated cells.
151 Interestingly, AL foci and AL-NPCs were also often localized near microtubules (Extended
152 Data Fig. 8c), suggesting that they may utilize MT-ER interactions to merge with the NE
153 and to increase the pool of NE-NPCs, as shown in embryonic cells[8]. Accordingly, the
154 density of NE-NPCs (Fig. 2f, g) and the level of Nups at NE (Extended Data Fig. 8d, e)
155 decreased upon short (90 minutes) nocodazole treatment. MT depolymerization inhibited
156 nuclear growth in G1/S arrested WT cells (Fig. 2h-j), excluding possible indirect effects of
157 nocodazole treatment on mitotic progression. Although nuclear growth is sustained by a
158 constant supply of many proteins and lipids from the ER to the NE[58], a process which could
159 also be disrupted by MT depolymerization, insertion of new pores of AL origin may
160 additionally support nuclear expansion by potentiating nucleocytoplasmic transport rates.
161 Thus, the widespread existence of AL in normally proliferating cells could be explained by
162 their role in merging with the NE and increasing the pool of NE-NPCs, thereby supporting
163 the nuclear expansion during early interphase.
164

165 **Direct function of RanBP2 in AL biogenesis in somatic cells**

166 Having demonstrated a universal cellular function of AL in normally growing cells, we next
167 aimed to uncover the mechanisms driving AL biogenesis. The component of NPC
168 cytoplasmic filaments RanBP2 (also known as Nup358) has been shown to localize to AL
169 structures and it has been proposed to regulate a Nup condensate fusion mechanism
170 supporting AL biogenesis during Drosophila oogenesis[11]. However, direct evidence for
171 RanBP2's role in AL formation is missing. It is also unknown if the role of RanBP2 is

conserved in somatic cells and in other species, and what the molecular basis for possible RanBP2 function on AL is.

RanBP2 was required for the formation of large AL foci induced by MT depolymerization and by inactivation of FXRPs-UBAP2L-dynein pathway in several human cell lines tested (Fig. 3a, d, Extended Data Fig. 9a-n). Likewise, RanBP2 was required for the formation of small AL foci in WT cells in all interphase stages (Extended Data Fig. 9o, p). Another component of NPC cytoplasmic filaments, Nup214, was not required for the formation of AL foci (Extended Data Fig. 10a-c).

Higher eukaryotes utilize two NE-NPC assembly pathways, each associated with different cell cycle stages: the postmitotic and the interphase pathways[59]. We found that downregulation of Nup153 or POM121 (driving interphase NE-NPC assembly), or ELYS (required for postmitotic NE-NPC assembly) did not inhibit AL foci formation induced by acute nocodazole treatment (Extended Data Fig. 10a-f). In contrast, defects in NE-NPC biogenesis were reported to induce AL[34] and as expected, downregulation of Nup153 or ELYS led to the formation of large AL foci (Extended Data Fig. 10a-f) and AL-NPCs (Extended Data Fig. 10g) in untreated cells. Downregulation of RanBP2 strongly inhibited the formation of AL foci induced by Nup153 or ELYS depletion (Fig. 3b, c, e, f), suggesting its universal and widespread role in AL biogenesis.

Is RanBP2 required for the formation of individual AL-NPCs or their coming together at the ER? The splitSMLM analysis revealed that both the number of individual AL-NPCs per cell as well as their clustering into single AL-foci increased upon acute MT depolymerization (Fig. 3g-i). RanBP2 was required for the assembly of individual AL-NPCs, (defined as structures with Nup133-positive outer ring shapes surrounding Nup62-positive central channel signal as seen in Fig. 1b), as well as their clustering both in WT and in nocodazole-treated cells (Fig. 3g-i). AL-NPCs were reported to lack nuclear basket components[8,53,54], whereas RanBP2 appears to be localized symmetrically on both sides of AL-NPCs[48] (Extended Data Fig. 2a) and RanBP2 can oligomerize to form multimers[60], providing a possible explanation for its ability to cluster individual AL-NPCs. These results demonstrate a direct role of RanBP2 in multiple steps of AL assembly.

Can RanBP2 also maintain the AL structures? Downregulation (Extended Data Fig. 11a-f) or auxin-inducible deletion (Extended Data Fig. 12a-e) of RanBP2[61] after MT depolymerization inhibited the number of AL foci and their expansion observed upon nocodazole treatment (Fig. 1e and Supplementary Video 1). Thus, RanBP2 is required for the formation and maintenance of AL. This process is likely to be independent of reported NPC degradation mechanisms involving autophagy[62,63], since RanBP2 downregulation inhibited AL foci formation also in the presence of lysosomal inhibitors (Extended Data Fig. 13a-h). Moreover, deletion or downregulation of RanBP2 did not affect protein levels of multiple Nups analyzed in whole cell extracts (Fig. 4h, Extended Data Fig. 16a-c). Collectively, RanBP2 plays direct and widespread roles in AL formation and maintenance in multiple somatic cells.

RanBP2 promotes oligomerization of scaffold components and assembly of AL-NPCs through its N-terminal domain

To understand if the function of RanBP2 is specific and which functional domains of this

large protein are required for AL formation, we performed rescue experiments using RanBP2 fragments. The full-length (FL) (aa 1-3224) and the N-terminal (NT) fragment of RanBP2 (aa 1-1171) efficiently reversed the inhibition of nocodazole-induced AL foci observed in the absence of RanBP2, and the phenylalanine-glycine (FG) repeat region (832-1171) was essential for RanBP2 AL function (Fig. 3j-m, Extended Data Fig. 14a-d). Ectopic expression of NT RanBP2 (aa 1-1171) (Fig. 4a, b, Extended Data Fig. 15a, b) but not of FL Nup85 or FL Nup133 (Extended Data Fig. 15c), was also sufficient to induce AL foci where multiple Nups, with the exception of Nup153 and ELYS, could co-localize, relative to controls. CLEM analysis (Fig. 4c) and splitSMLM (Fig. 4d-e) confirmed that these foci represent AL. Ectopic expression of NT RanBP2 increased the number of individual NPCs per cell and the size of AL (8,3 NPCs relative to 1,7 NPCs in control cells), similar to the observations in cells with depolymerized microtubules (Fig. 1b, Extended Data Fig. 2d). We conclude that RanBP2 is specifically required for AL formation through its FG repeat region, and that the NT RanBP2 fragment is sufficient to induce AL under normal growth conditions.

Since RanBP2 was important for the assembly of individual AL-NPCs in the cytoplasm (Fig. 3g-i, Fig. 4f) and intrinsically disordered FG repeats have been reported to stabilize subcomplexes within NE-NPC[64], we examined interactions between the RanBP2 NT fragment and other relevant Nups. The outer ring of the NPC is mainly composed of the evolutionarily conserved Nup107-Nup160 complex (also named Y complex). We find that the N-terminal fragment of RanBP2 can bind the Y complex, as well as Nup205 and Nup93 (Fig. 4g, h), which belong to the inner ring but have recently been reported to also reside on the cytoplasmic face of NPCs[60]. The interaction between these Nups with NT RanBP2 turns out to be dependent on the FG repeat domain (Fig. 4g), suggesting that it facilitates the assembly of AL-NPCs.

Deletion of RanBP2 did not affect the formation of the Y complex (Extended Data Fig. 16a, b) both in the cytoplasm and in the nucleus (Extended Data Fig. 16b), but it restricted the binding of the Y complex to Nup93 specifically in the cytoplasm (Extended Data Fig. 16a, c). This suggests that RanBP2 may stabilize the interactions between the outer and inner rings in agreement with reported high-resolution structures of NPC[60], and thereby promote AL-NPC assembly. Indeed, Nup93 was required for the formation of small and large AL-foci (Extended Data Fig. 16d-f), and the increase of AL foci by ectopic expression of NT RanBP2 was dependent on Nup93 (Extended Data Fig. 16h, i, k, l, m). Downregulation of Nup93 also led to the formation of Nup62-positive nuclear foci (Extended Data Fig. 16d, j), which did not co-localize with other Nups, suggesting that they may not represent AL. Co-localization of NT RanBP2 with Nup133 (Extended Data Fig. 16j) and Nup62 (Extended Data Fig. 16m) in the cytoplasm required Nup93, in line with reports showing that Nup93 helps to connect the central channel to the NPC scaffold[65]. We conclude that the function of the NT part of RanBP2 on AL-NPCs can be attributed to its reported interactions with Nup93 and its ability to stabilize connections between NPC subcomplexes.

Interestingly, structural analysis of the NPC demonstrated that five RanBP2 and one Nup93 molecule bind to the overlapping region of two Y complexes in the scaffold's outer ring[60], and deletion of RanBP2 resulted in an outer ring that lacked Y complexes on the cytoplasmic side[66]. To test if RanBP2 can promote the oligomerization state of scaffold

260 components, we analyzed the cytoplasmic and nuclear cellular fractions by gel-filtration
261 chromatography. Deletion of RanBP2 inhibited the formation of Y complex oligomers in the
262 cytoplasm (Fig. 4i) but surprisingly not in the nucleus (Extended Data Fig. 17a, b). These
263 findings are in line with the role of RanBP2 in ensuring the binding of the Y complex to
264 Nup93 specifically in the cytoplasm (Fig. 4h, Extended Data Fig. 16a, c).
265 Taken together, these results identify the precise molecular mechanism of AL-NPC
266 formation and show that RanBP2 promotes the interaction between the Y complex and
267 Nup93, as well as the oligomerization of scaffold AL-NPC components.
268

269 RanBP2 preserves nuclear pore function and nuclear growth during early 270 interphase

271 Our data in normally proliferating cells demonstrated a universal role for AL in merging with
272 the NE and increasing the pool of NE-NPCs, thereby supporting the nuclear expansion
273 during early interphase. We thus analyzed the effect of RanBP2 on nuclear pore function.
274 RanBP2 deletion resulted in reduced NPC density (Fig. 4j, k) and RanBP2 downregulation
275 decreased levels of Nups at the NE (Extended Data Fig. 18a, b). Short-term depletion of
276 RanBP2 by auxin-inducible degron reduced levels of several Nups in isolated nuclear
277 fractions and increased their abundance in the cytoplasm in DLD-1 (Extended Data Fig.
278 18c) and HTC116 cells (Extended Data Fig. 18d), consistent with the idea that RanBP2
279 does not regulate the total protein levels of Nups (Fig. 4h, Extended Data Fig. 16a-c) but
280 their localization to the NE. Small AL foci and the levels of Nups at the NE decreased
281 throughout interphase upon deletion of RanBP2 (Extended Data Fig. 18e-i), suggesting
282 that RanBP2-mediated AL formation is a prerequisite for their merging with NE and
283 increasing the pool of NE-NPCs. These observations could not be explained by the
284 previously reported[67] moderate delay in mitotic exit (Extended Data Fig. 18j), as the levels
285 of mitotic cyclins were already largely decreased in RanBP2-deficient cells during the early
286 interphase stages analyzed in our experiments (Extended Data Fig. 7i, g, l, Extended Data
287 Fig. 18e, j). Likewise, the levels of FXR1 and UBAP2L, the factors driving spatial assembly
288 of Nups during early interphase[48], were not affected by auxin-inducible depletion of
289 RanBP2 in DLD-1 (Extended Data Fig. 18k) and HTC116 cells (Extended Data Fig. 18l). If
290 ELYS-dependent postmitotic pathway[34] was not fully completed in RanBP2-depleted cells,
291 one would expect accumulation of AL (Extended Data Fig. 10d-f) between early (Extended
292 Data Fig. 18f) and late interphase stages (Extended Data Fig. 18g), which is in contrast to
293 our observations that show the requirement of RanBP2 for AL biogenesis. These results
294 further confirm that AL-NPCs are a likely source of NE-NPCs and that RanBP2-mediated
295 AL-NPC assembly contributes to nuclear pore density during interphase.
296 Can RanBP2 also preserve the nuclear pore function? We analyzed the gradient of
297 endogenous Ran, a guanine nucleotide triphosphatase, as previously reported[38,48], owing
298 to the fact that Ran protein is actively imported to the nucleus with the help of transport
299 factors. Short-term (Extended Data Fig. 19a, b) and long-term depletion of RanBP2
300 (Extended Data Fig. 19c, d) in DLD-1 and HTC116 cells, as well as downregulation of
301 RanBP2 (Extended Data Fig. 19e, f) increased the nuclear-cytoplasmic (N/C) ratio of Ran,
302 suggesting significant defects in the nuclear export rate of Ran protein. The use of the light-
303 inducible nuclear export system (LEXY)[68], confirmed these export defects upon acute

304 depletion of RanBP2 (Extended Data Fig. 19g, h). Moreover, short-term depletion of
305 RanBP2 was sufficient to reduce nuclear size (Fig. 4l, m), in line with our observations in
306 nocodazole-treated cells (Fig. 2h-j). We conclude that RanBP2-mediated AL-NPC
307 assembly can preserve nuclear pore density and function, as well as nuclear growth during
308 interphase, confirming the critical role of cytosolic NPCs in the nuclear function
309

310 Climp63 facilitates the localization of AL-NPCs to ER sheets and their 311 integration with the NE

312 Our data on molecular mechanism of AL assembly and the direct role of RanBP2 in this
313 process create unique opportunity to identify additional factors involved in AL biology. Since
314 the NT RanBP2 fragment was sufficient for the formation of AL (Fig. 4a-f), we analyzed the
315 proteins interacting with HA-tagged NT RanBP2 (aa 1-1171) compared to HA-tag only,
316 using liquid chromatography-mass spectrometry (LC–MS). Of total 97 protein specifically
317 bound to NT RanBP2, 20 were associated with the NPC, as expected, but numerous ER-
318 associated proteins were also identified (Extended Data Fig. 20a, b). Among them,
319 Climp63 (also known as CKAP4), a type II membrane protein, emerged as an interesting
320 candidate for the regulation of AL. Climp63 has been implicated in maintaining ER
321 morphology, being important for the biogenesis of ER sheets and regulation of their width,
322 and for coordinating the formation and dynamics of ER nanoholes[69,70]. Moreover, its N-
323 terminus binds to MTs, linking the ER to the cytoskeleton[71].
324 We indeed detect the interaction between the HA-tagged NT RanBP2 and endogenous
325 RanBP2 and Climp63 (Fig. 5a-c). In interphase cells, RanBP2-labeled AL foci preferentially
326 localized to ER regions positive for Climp63 (Fig. 5d-f), residing closer to the nucleus
327 relative to the entire ER network (Extended Data Fig. 20d). These Climp63-positive regions
328 likely correspond to ER sheets, in line with published findings[70]. This suggests that, under
329 normal growth conditions, AL may primarily reside within sheet-like regions of the ER rather
330 than in its tubules. The tendency of the ER sheets to localize close to the nucleus may
331 facilitate AL merging with the NE under physiological conditions.
332 Downregulation of Climp63 (Fig. 5g) led to the dispersion of ER sheets throughout the
333 cytoplasm (Fig. 5h), in accordance with previous reports[70], and strongly altered the
334 morphology and distribution of AL foci. AL foci increased in both abundance (Fig. 5i) and
335 size (Fig. 5j), relocating to the cell periphery, regions that originally corresponded to ER
336 tubules (Fig. 5h, l), in Climp63 downregulated cells. One can speculate that the reported
337 Climp63 ability to connect ER to MTs could explain the observed phenotype and Climp63
338 absence would inhibit MT-mediated transport of AL towards NE. Alternatively, Climp63-
339 mediated regulation of ER dynamics and nanomorphology could explain these effects.
340 These observations also suggest that RanBP2-mediated biogenesis of AL-NPCs in the
341 cytosol can be separated from their proper localization at ER membranes, a process
342 directly dependent on Climp63 and that in the absence of Climp63 cells attempt to
343 compensate these defects by increasing the formation of AL-NPCs.
344 Irrespectively of underlying mechanisms, which should remain the topic of future
345 investigations, downregulation of Climp63 decreased Nup levels at the NE (Fig. 5h, k) and
346 inhibited nuclear growth (Fig. 5l, m), suggesting that Climp63-mediated ER dynamics is an
347 important prerequisite for the integration of AL-NPCs into the NE in normal cells. Taken

together, our results identified RanBP2 to be crucial for the formation of AL-NPCs and Climp63 as a factor targeting AL-NPCs to the proper membrane compartment, the ER sheets, thereby supporting AL nuclear function.

Discussion

In this study, we demonstrate a universal function and biogenesis mechanism of Annulate Lamellae, a mysterious cellular structure known for decades to exist in the cytoplasm[3,23]. Using advanced super-resolution microscopy approaches including SMLM and image analysis, we show that AL are more abundant than previously anticipated and exist in the cytoplasm of a variety of somatic cells under normal physiological conditions. SMLM analysis therefore emerges as an important tool in the future investigation of AL distribution in healthy and diseased cells, as exemplified by our data in the fragile-X syndrome patient-derived cells (Fig. 1c).

We demonstrate that during interphase, AL can merge with the NE and supply it with formed nuclear pore complexes, a process that is particularly active during periods of rapid nuclear growth (Fig. 5n). Inhibition of AL merging with the NE, either by blocking their MT-based movement using nocodazole or by interfering with their biogenesis through RanBP2 deletion or by preventing their Climp63-mediated localization at ER membranes proximal to the nucleus, reduces the density of nuclear pores and inhibits nuclear growth. These findings could explain why, in the past, AL have been commonly observed in rapidly developing, cancerous, or challenged cells, which are likely to more crucially depend on efficient nuclear export and rapid nuclear growth[4–12] and thereby may increase the pool of AL in the cytoplasm. Blocks of AL structures inserted into the NE have been previously observed in Drosophila blastoderm embryos[8], while our study suggests that this process is widespread and operates in somatic cells in general. AL have been also implicated to merge with NE in postmitotic cells[25], however this phenomenon seemed independent of ER membranes and rather involved direct interactions with decondensing chromosomes. The existence of small AL structures shown in our study may, in fact, be advantageous for normally proliferating cells. It may help to avoid topological constraints associated with the simultaneous NE insertion of numerous AL-NPCs, which are arranged in several parallel ER membranes in the cytoplasm. While we show that small AL are clearly beneficial for cellular homeostasis by preserving the nuclear function, the accumulation of large AL structures could be the outcome of a compensatory effect and continued AL biogenesis due to inhibition of their integration with NE. It is also possible that compromised NPC function and accumulation of large AL, as seen in fragile-X syndrome cells, have other downstream toxic effects.

In addition to elucidating the universal cellular function of AL, the direct molecular mechanisms of AL formation identified in our study explain how AL-NPCs are made and how they localize to the proper compartment of the ER (Fig. 5n). RanBP2 is indispensable for the assembly of cytosolic AL-NPCs across cells and conditions, serving as an assembly platform that specifically regulates the oligomerization of Y complexes within the AL-NPC scaffold. While this process may involve other structurally important Nups, such as Nup93, the N-terminal region of RanBP2 containing FG repeats is required and sufficient for AL biogenesis. Intrinsically disordered FG repeats have been shown to stabilize

subcomplexes within NE-NPC[64], providing a possible explanation for their function on AL-NPCs. The role of cohesive FG repeats could also help to understand previous observations in fly embryos, where RanBP2 was implicated in recruiting various condensed precursor Nup particles, possibly leading to AL biogenesis[11]. Here, we provide direct evidence for the role of RanBP2 in AL biogenesis and clarify the detailed molecular requirements for AL-NPC formation.

On the membrane side, we identify Climp63 as playing a crucial role in localizing AL-NPCs to ER sheets proximal to the nucleus, a process important for their subsequent integration into the NE and nuclear growth. We could not identify any reports directly linking AL to specific ER substructure so far. Since Climp63 ensures not only the formation of ER sheets but also the biogenesis of ER nanoholes[69,70], which were discussed to be similar in size to nuclear pores[69], it would be exciting to study the roles of ER dynamics and nanomorphology in AL biogenesis. It would be also important to understand if the reported role of Climp63 in connecting ER to MTs could explain its role in positioning AL in proximity to the NE and what is the involvement of other ER factors identified in the RanBP2-dependent AL proteome (Extended Data Fig. 20a, b). Likewise, a possible role of NE-resident proteins SUN1 and SUN2 which we found to co-localize with AL foci (Extended Data Fig. 5b) and which are components of linker of nucleoskeleton and cytoskeleton (LINC) complexes[72], playing a role in early steps of NPC interphase assembly[73] should be a subject of future investigation. Undoubtedly, our findings not only clarify the fundamental mechanisms of AL biogenesis but also create an important ground for future investigations aiming to identify AL-specific factors.

Maintaining NPC function is crucial for normal cellular physiology, as disruptions in nucleocytoplasmic transport, mis-localization of Nups, and elevated levels of AL have been observed in various diseased and infected cells[13,33,35–41]. The biological principles of AL biology identified by our study may create a basis for future approaches to restore NPC homeostasis in human diseases such as fragile-X syndrome and numerous other neurological and neurodegenerative diseases as well as cancer[24].

Acknowledgements

We thank members of the Sumara, I. and Ricci, R. laboratories for helpful discussions on the manuscript and IGBMC facilities especially the imaging center for their help. Lin, J. and Liao, Y. were supported by PhD fellowships from the China Scholarship Council (CSC). Agote-Aran, A., was supported by PhD fellowship from the IMCBio graduate school and a fellowship from the “Ligue Nationale Contre le Cancer”. Schoch, R. and Klaholz, B. P. acknowledge support by Institut National du Cancer (INCa) and by the French Infrastructure for Integrated Structural Biology (FRISBI) ANR-10-INSB-05-01, Instruct-ERIC and iNEXT-Discovery. Research in Sumara, I. laboratory was supported by the grant ANR-10-LABX-0030-INRT, a French State fund managed by the Agence Nationale de la Recherche (ANR) under the frame program Investissements d’Avenir ANR-10-IDEX-0002-02, IGBMC, CNRS, ARC, INCa (PLBIO 2022-082), ANR (AAPG2022, NICE4Nups) and AFM-Telethon.

Author contributions

The role of RanBP2 in human cytosolic NPCs was initially discovered by A.A.A. and confirmed by J.L., and the research plan and the conceptualization of the results were based on discussions between J.L., A.A.A. and I.S.. J.L. performed most of the experiments and analyzed the data. Y.L. helped with experiments on UBAP2L, S.R. helped with splitSMLM analyses, P.R. helped with CLEM, R.Z. helped with gel-filtration chromatography and C.K. helped with the reagents and materials. M.R., Y.S. and B.P.K. helped with the design of the experiments and supervision. I.S. supervised the project and J.L. and I.S. wrote the manuscript with input from all authors.

Competing interest

The authors declare no competing interests.

Additional information

The supplementary materials consist of Supplementary Table 1, Supplementary Videos 1-3 and Extended Data Figures 1-20.

References

1. Kessel, R. G. Annulate lamellae: a last frontier in cellular organelles. *Int Rev Cytol* **133**, 43–120 (1992).
2. Kessel, R. G. The annulate lamellae--from obscurity to spotlight. *Electron Microsc Rev* **2**, 257–348 (1989).
3. McCulloch, D. Fibrous structures in the ground cytoplasm of the Arbacia egg. *J. Exp. Zool.* **119**, 47–63 (1952).
4. Rawe, V. Y., Olmedo, S. B., Nodar, F. N., Ponzio, R. & Sutovsky, P. Abnormal assembly of annulate lamellae and nuclear pore complexes coincides with fertilization arrest at the pronuclear stage of human zygotic development. *Hum Reprod* **18**, 576–582 (2003).
5. Zybina, E. V. & Zybina, T. G. Modifications of nuclear envelope during differentiation and depolyploidization of rat trophoblast cells. *Micron* **39**, 593–606 (2008).
6. Caruso, R. A. *et al.* Modifications of nuclear envelope in tumour cells of human gastric carcinomas: an ultrastructural study. *Anticancer Res* **30**, 699–702 (2010).
7. Gil-Perotín, S. *et al.* Adult neural stem cells from the subventricular zone: a review of the neurosphere assay. *Anat Rec (Hoboken)* **296**, 1435–1452 (2013).
8. Hampoelz, B. *et al.* Pre-assembled Nuclear Pores Insert into the Nuclear Envelope during Early Development. *Cell* **166**, 664–678 (2016).
9. Underwood, J. M., Becker, K. A., Stein, G. S. & Nickerson, J. A. The Ultrastructural Signature of Human Embryonic Stem Cells. *J Cell Biochem* **118**, 764–774 (2017).
10. Grandi, G., Astolfi, G., Chicca, M. & Pezzi, M. Ultrastructural investigations on spermatogenesis and spermatozoan morphology in the endangered Adriatic sturgeon, Acipenser naccarii (Chondrostei, Acipenseriformes). *J Morphol* **279**, 1376–1396 (2018).
11. Hampoelz, B. *et al.* Nuclear Pores Assemble from Nucleoporin Condensates During Oogenesis. *Cell* **179**, 671-686.e17 (2019).
12. Dymek, A. M., Pecio, A. & Piprek, R. P. Diversity of Balbiani body formation in internally

and externally fertilizing representatives of Osteoglossiformes (Teleostei: Osteoglossomorpha). *J Morphol* **282**, 1313–1329 (2021).

13. Eymieux, S., Blanchard, E., Uzbekov, R., Hourioux, C. & Roingeard, P. Annulate lamellae and intracellular pathogens. *Cellular Microbiology* **23**, (2021).
14. Caldas, L. A. *et al.* Intracellular host cell membrane remodelling induced by SARS-CoV-2 infection in vitro. *Biol Cell* **113**, 281–293 (2021).
15. Eymieux, S. *et al.* Ultrastructural modifications induced by SARS-CoV-2 in Vero cells: a kinetic analysis of viral factory formation, viral particle morphogenesis and virion release. *Cell Mol Life Sci* **78**, 3565–3576 (2021).
16. Patrizi, G. & Middelkamp, J. N. Development and changes of annulate lamellae complexes in rubella virus-infected RK-13 cells. *J Ultrastruct Res* **31**, 407–423 (1970).
17. Klinger, M. H., Kämmerer, R., Hornei, B. & Gauss-Müller, V. Perinuclear accumulation of hepatitis A virus proteins, RNA, and particles and ultrastructural alterations in infected cells. *Arch Virol* **146**, 2291–2307 (2001).
18. Ahlqvist, J. *et al.* Complete replication cycle and acquisition of tegument in nucleus of human herpesvirus 6A in astrocytes and in T-cells. *J Med Virol* **78**, 1542–1553 (2006).
19. Romero-Brey, I. *et al.* Three-dimensional architecture and biogenesis of membrane structures associated with hepatitis C virus replication. *PLoS Pathog* **8**, e1003056 (2012).
20. Wang, J. J. *et al.* Ultrastructure and localization of E proteins in cultured neuron cells infected with Japanese encephalitis virus. *Virology* **238**, 30–39 (1997).
21. Caldas, L. A., Azevedo, R. C., da Silva, J. L. & de Souza, W. Microscopy analysis of Zika virus morphogenesis in mammalian cells. *Sci Rep* **10**, 8370 (2020).
22. Huber, S. *et al.* Recruitment of Host Nuclear Pore Components to the Vicinity of Theileria Schizonts. *mSphere* **5**, e00709-19 (2020).
23. Swift, H. The fine structure of annulate lamellae. *J Biophys Biochem Cytol* **2**, 415–418 (1956).
24. Lin, J. & Sumara, I. Cytoplasmic nucleoporin assemblage: the cellular artwork in physiology and disease. *Nucleus* **15**, 2387534 (2024).
25. Ren, H. *et al.* Postmitotic annulate lamellae assembly contributes to nuclear envelope reconstitution in daughter cells. *J Biol Chem* **294**, 10383–10391 (2019).
26. Raghunayakula, S., Subramonian, D., Dasso, M., Kumar, R. & Zhang, X.-D. Molecular Characterization and Functional Analysis of Annulate Lamellae Pore Complexes in Nuclear Transport in Mammalian Cells. *PLoS One* **10**, e0144508 (2015).
27. Patterson, J. R., Wood, M. P. & Schisa, J. A. Assembly of RNP granules in stressed and aging oocytes requires nucleoporins and is coordinated with nuclear membrane blebbing. *Dev Biol* **353**, 173–185 (2011).
28. Sahoo, M. R. *et al.* Nup358 binds to AGO proteins through its SUMO-interacting motifs and promotes the association of target mRNA with miRISC. *EMBO Rep* **18**, 241–263 (2017).
29. Rawe, V. Y., Olmedo, S. B., Nodar, F. N., Ponzio, R. & Sutovsky, P. Annulate lamellae assembly in non-inseminated and failed fertilized human oocytes. *Fertility and Sterility* **78**, S163 (2002).
30. Boulware, M. J. & Marchant, J. S. Nuclear pore disassembly from endoplasmic

524 reticulum membranes promotes Ca2+ signalling competency. *J Physiol* **586**, 2873–
525 2888 (2008).
526 31. Boulware, M. J. & Marchant, J. S. IP3 receptor activity is differentially regulated in
527 endoplasmic reticulum subdomains during oocyte maturation. *Curr Biol* **15**, 765–770
528 (2005).
529 32. Jühlen, R. & Fahrenkrog, B. From the sideline: Tissue-specific nucleoporin function in
530 health and disease, an update. *FEBS Letters* **597**, 2750–2768 (2023).
531 33. Coyne, A. N. & Rothstein, J. D. Nuclear pore complexes - a doorway to neural injury
532 in neurodegeneration. *Nat Rev Neurol* **18**, 348–362 (2022).
533 34. Kuiper, E. F. E. *et al.* The chaperone DNAJB6 surveils FG-nucleoporins and is required
534 for interphase nuclear pore complex biogenesis. *Nat Cell Biol* **24**, 1584–1594 (2022).
535 35. Agote-Aran, A. *et al.* Spatial control of nucleoporin condensation by fragile X-related
536 proteins. *EMBO J* **39**, e104467 (2020).
537 36. Lin, Y.-C. *et al.* Interactions between ALS-linked FUS and nucleoporins are associated
538 with defects in the nucleocytoplasmic transport pathway. *Nat Neurosci* **24**, 1077–1088
539 (2021).
540 37. Gleixner, A. M. *et al.* NUP62 localizes to ALS/FTLD pathological assemblies and
541 contributes to TDP-43 insolubility. *Nat Commun* **13**, 3380 (2022).
542 38. Zhang, K. *et al.* The C9orf72 repeat expansion disrupts nucleocytoplasmic transport.
543 *Nature* **525**, 56–61 (2015).
544 39. Suhr, S. T. *et al.* Identities of sequestered proteins in aggregates from cells with
545 induced polyglutamine expression. *J Cell Biol* **153**, 283–294 (2001).
546 40. Grima, J. C. *et al.* Mutant Huntingtin Disrupts the Nuclear Pore Complex. *Neuron* **94**,
547 93-107.e6 (2017).
548 41. Pappas, S. S., Liang, C.-C., Kim, S., Rivera, C. O. & Dauer, W. T. TorsinA dysfunction
549 causes persistent neuronal nuclear pore defects. *Hum Mol Genet* **27**, 407–420 (2018).
550 42. Thomas, L., Taleb Ismail, B., Askjaer, P. & Seydoux, G. Nucleoporin foci are stress-
551 sensitive condensates dispensable for C. elegans nuclear pore assembly. *EMBO J* **42**,
552 e112987 (2023).
553 43. Vihola, A. *et al.* Novel mutation in TNPO3 causes congenital limb-girdle myopathy with
554 slow progression. *Neurol Genet* **5**, e337 (2019).
555 44. Jul-Larsen, A., Grudic, A., Bjerkvig, R. & Bøe, S. O. Cell-cycle regulation and dynamics
556 of cytoplasmic compartments containing the promyelocytic leukemia protein and
557 nucleoporins. *J Cell Sci* **122**, 1201–1210 (2009).
558 45. Chow, K.-H., Elgort, S., Dasso, M., Powers, M. A. & Ullman, K. S. The SUMO
559 proteases SENP1 and SENP2 play a critical role in nucleoporin homeostasis and
560 nuclear pore complex function. *Mol Biol Cell* **25**, 160–168 (2014).
561 46. Scarcelli, J. J., Hodge, C. A. & Cole, C. N. The yeast integral membrane protein Apq12
562 potentially links membrane dynamics to assembly of nuclear pore complexes. *J Cell
563 Biol* **178**, 799–812 (2007).
564 47. Agote-Arán, A., Lin, J. & Sumara, I. Fragile X-Related Protein 1 Regulates Nucleoporin
565 Localization in a Cell Cycle-Dependent Manner. *Front Cell Dev Biol* **9**, 755847 (2021).
566 48. Liao, Y. *et al.* UBAP2L ensures homeostasis of nuclear pore complexes at the intact
567 nuclear envelope. *Journal of Cell Biology* **223**, e202310006 (2024).

49. Andronov, L., Vonesch, J.-L. & Klaholz, B. P. Practical Aspects of Super-Resolution Imaging and Segmentation of Macromolecular Complexes by dSTORM. *Methods Mol Biol* **2247**, 271–286 (2021).
50. Lelek, M. *et al.* Single-molecule localization microscopy. *Nat Rev Methods Primers* **1**, 39 (2021).
51. Andronov, L., Genthial, R., Hentsch, D. & Klaholz, B. P. splitSMLM, a spectral demixing method for high-precision multi-color localization microscopy applied to nuclear pore complexes. *Commun Biol* **5**, 1100 (2022).
52. Kessel, R. G. The structure and function of annulate lamellae: porous cytoplasmic and intranuclear membranes. *Int Rev Cytol* **82**, 181–303 (1983).
53. Rasala, B. A., Ramos, C., Harel, A. & Forbes, D. J. Capture of AT-rich chromatin by ELYS recruits POM121 and NDC1 to initiate nuclear pore assembly. *Mol Biol Cell* **19**, 3982–3996 (2008).
54. Walther, T. C. *et al.* RanGTP mediates nuclear pore complex assembly. *Nature* **424**, 689–694 (2003).
55. Maeshima, K. *et al.* Nuclear pore formation but not nuclear growth is governed by cyclin-dependent kinases (Cdks) during interphase. *Nat Struct Mol Biol* **17**, 1065–1071 (2010).
56. De Magistris, P. & Antonin, W. The Dynamic Nature of the Nuclear Envelope. *Current Biology* **28**, R487–R497 (2018).
57. Chen, S., Novick, P. & Ferro-Novick, S. ER structure and function. *Current Opinion in Cell Biology* **25**, 428–433 (2013).
58. Deolal, P., Scholz, J., Ren, K., Bragulat-Teixidor, H. & Otsuka, S. Sculpting nuclear envelope identity from the endoplasmic reticulum during the cell cycle. *Nucleus* **15**, 2299632 (2024).
59. Weberruss, M. & Antonin, W. Perforating the nuclear boundary - how nuclear pore complexes assemble. *J Cell Sci* **129**, 4439–4447 (2016).
60. Bley, C. J. *et al.* Architecture of the cytoplasmic face of the nuclear pore. *Science* **376**, eabm9129 (2022).
61. Aksenova, V., Arnaoutov, A. & Dasso, M. Analysis of Nucleoporin Function Using Inducible Degron Techniques. *Methods Mol Biol* **2502**, 129–150 (2022).
62. Tomioka, Y. *et al.* TORC1 inactivation stimulates autophagy of nucleoporin and nuclear pore complexes. *J Cell Biol* **219**, e201910063 (2020).
63. Lee, C.-W. *et al.* Selective autophagy degrades nuclear pore complexes. *Nat Cell Biol* **22**, 159–166 (2020).
64. Onischenko, E. *et al.* Natively Unfolded FG Repeats Stabilize the Structure of the Nuclear Pore Complex. *Cell* **171**, 904-917.e19 (2017).
65. Vollmer, B. & Antonin, W. The diverse roles of the Nup93/Nic96 complex proteins – structural scaffolds of the nuclear pore complex with additional cellular functions. *Biological Chemistry* **395**, 515–528 (2014).
66. Von Appen, A. *et al.* In situ structural analysis of the human nuclear pore complex. *Nature* **526**, 140–143 (2015).
67. Hashizume, C., Kobayashi, A. & Wong, R. W. Down-modulation of nucleoporin RanBP2/Nup358 impaired chromosomal alignment and induced mitotic catastrophe.

612 *Cell Death Dis* **4**, e854 (2013).
613 68. Niopek, D., Wehler, P., Roensch, J., Eils, R. & Di Ventura, B. Optogenetic control of
614 nuclear protein export. *Nat Commun* **7**, 10624 (2016).
615 69. Schroeder, L. K. *et al.* Dynamic nanoscale morphology of the ER surveyed by STED
616 microscopy. *Journal of Cell Biology* **218**, 83–96 (2019).
617 70. Shibata, Y. *et al.* Mechanisms Determining the Morphology of the Peripheral ER. *Cell*
618 **143**, 774–788 (2010).
619 71. Klopfenstein, D. R. Ch., Kappeler, F. & Hauri, H.-P. A novel direct interaction of
620 endoplasmic reticulum with microtubules. *The EMBO Journal* **17**, 6168–6177 (1998).
621 72. Hetzer, M. W. The nuclear envelope. *Cold Spring Harb Perspect Biol* **2**, a000539
622 (2010).
623 73. Talamas, J. A. & Hetzer, M. W. POM121 and Sun1 play a role in early steps of
624 interphase NPC assembly. *Journal of Cell Biology* **194**, 27–37 (2011).

625

Methods

Antibodies

The following primary antibodies were used: rabbit monoclonal anti-Nup133 (Abcam, ab155990), mouse monoclonal anti-Nup133 (E-6) (Santa Cruz Biotechnology, sc-376763 AF488), mouse monoclonal anti-Nucleoporin p62 (BD Biosciences, 610497), rabbit polyclonal anti-RanBP2 (Abcam, ab64276), rabbit polyclonal anti-Nup214 (Abcam, ab70497), rabbit polyclonal anti-Nup85 (Bethyl, A303-977A), mouse monoclonal anti-Pericentrin 1 (D-4) (Nup85) (Santa Cruz Biotechnology, sc-376111), rabbit monoclonal anti-SEC13 (R&D systems, MAB9055), rabbit polyclonal anti-Nup214 (Abcam, ab70497), rabbit polyclonal anti- ELYS (Bethyl, A300-166A), mouse monoclonal Nup205 (H-1) (Santa Cruz Biotechnology, sc-377047), mouse monoclonal anti-Nup93 (E-8) (Santa Cruz Biotechnology, sc-374399), rabbit monoclonal anti-Nup98 (C39A3) (Cell Signaling Technology, 2598), rabbit polyclonal anti-POM121 (GeneTex, GTX102128), rabbit polyclonal anti-Nup153 (Abcam, ab84872), rabbit polyclonal anti-CRM1/Exportin 1 (Novus, NB100-79802), rabbit monoclonal anti-NTF97/Importin beta (Abcam, ab2811), mouse monoclonal anti-Ran (BD Biosciences, 610340), rabbit monoclonal anti-SUN1 (Abcam, ab124770), rabbit monoclonal anti-SUN2 (Abcam, ab124916), rabbit polyclonal anti-Lamin A (C-terminal) (Sigma, L1293), rabbit polyclonal anti-Lamin B1 (Abcam, ab16048), rabbit monoclonal anti-Nesprin1 (Abcam, ab192234), rabbit polyclonal anti-Emerin (Abcam, ab40688), rabbit polyclonal anti-LAP2 (Proteintech, 14651-1-AP), rabbit anti-Phospho-Rb (Ser807/811) (Cell Signaling Technology, 9308), mouse monoclonal anti-Cyclin B1 (G-11) (Santa Cruz Biotechnology, sc-166757), rabbit polyclonal anti-Cyclin B1 (GeneTex, GTX100911), rat monoclonal anti-HA (Roche, 11867423001), rabbit polyclonal anti-GAPDH (Sigma, G9545), mouse monoclonal anti-β-Actin (Sigma, A2228), mouse monoclonal anti-mCherry (4B3) (Thermo scientific, MA5-32977), rabbit polyclonal anti-UBAP2L (Abcam, ab138309), rabbit polyclonal anti-Tubulin (Abcam, ab18251), mouse monoclonal anti-α-Tubulin (Sigma, T9026), mouse monoclonal anti-Nuclear Pore Complex Proteins (mAb414) (Abcam, ab24609), rabbit polyclonal anti-LC3B (Novus biological, NB100-2220SS), rabbit polyclonal anti-LC3A (Novus biological, NB100-2331), rat monoclonal anti-GFP (3H9) (ChromoTek, 3h9-100), rabbit polyclonal anti-GFP (Abcam, ab290), rabbit polyclonal anti- Aurora B (Abcam, ab2254), rabbit polyclonal anti-cyclin A (H-432) (Santa Cruz Biotechnology, sc-751), mouse monoclonal anti-PDI (Abcam, ab2792), mouse monoclonal anti-Climp63 (Enzo, ALX-804-604).

Secondary antibodies used were the following: goat anti-mouse IgG antibody (HRP) (GeneTex, GTX213111-01), goat anti-mouse IgG antibody (HRP) (GeneTex, GTX213110-01) and goat anti-rat IgG antibody (HRP) (Cell Signaling Technology, 7077S), goat polyclonal anti-Mouse AF647 (Thermo Fisher Scientific, A-21236), goat polyclonal anti-mouse AF568 (Thermo Fisher Scientific, A-11031), goat polyclonal anti-mouse AF555 (Thermo Fisher Scientific, A-11029), goat polyclonal anti-mouse AF488 (Thermo Fisher Scientific, A-21424), goat polyclonal anti-rabbit AF647 (Thermo Fisher Scientific, A-21245), goat polyclonal anti-rabbit AF568 (Thermo Fisher Scientific, A-11036), goat polyclonal anti-rabbit AF555 (Thermo Fisher Scientific, A-21429), goat polyclonal anti-rabbit AF488 (Thermo Fisher Scientific, A-11034), goat polyclonal anti-mouse CF680 (Sigma,

670 SAB4600199), goat polyclonal anti-chicken CF660C (Sigma, SAB4600458), goat
671 polyclonal anti-rat CF660C (Sigma, SAB4600193).
672
673 **Plasmid and siRNA transfections**
674 The following plasmid were used: pX330-P2A-EGFP/RFP and pUC57 was a generous gift
675 from Zhirong Zhang (Romeo Ricci lab IGBMC). pQCXIP-mScarlet-ER was a generous gift
676 from Julie EICHLER[1] (Catherine-Laure TOMASETTO lab IGBMC). pEF-HA-MCS2, pEF-
677 HA-RanBP2(1-3224), pEF-HA-RanBP2(1-2448), and pEF-HA-RanBP2(1-1171) were
678 generous gifts from Ralph Kehlenbach (University of Göttingen). pEF-HA-RanBP2(1-832)
679 was obtained by inserting the target sequence, obtained by PCR using pEF-HA-RanBP2(1-
680 3224) as a template, into pEF-HA-MCS2. NLS-mCherry-LEXY (pDN122) was purchased
681 from Addgene (Plasmid #72655). The primers used for plasmid generation are provided in
682 Supplementary Table 1.
683 The following siRNA oligonucleotides were used: Non-targeting individual siRNA
684 (Dharmacon), FXR1 siRNA (Dharmacon), UBAP2L siRNA (Dharmacon), RanBP2 siRNA
685 (Dharmacon), Nup153 siRNA (Dharmacon), ELYS siRNA (Dharmacon), POM121 siRNA
686 (Life Technologies), Nup214 siRNA (Eurogenetec) and Nup93 siRNA (Horizon). The
687 sequences of siRNA are provided in Supplementary Table 1.
688 X-tremeGENETM 9 DNA Transfection Reagent (Roche) were used to perform plasmid
689 transient transfection according to the manufacturer's instructions. Lipofectamine
690 RNAiMAX (Invitrogen) was used to deliver siRNAs for gene knock-down (KD) according to
691 the manufacturer's instructions.
692
693 **Generation of cell lines and cell culture**
694 HeLa Kyoto (human cervix carcinoma) cells and U2OS (human bone osteosarcoma) cells
695 were purchased from ATCC. HeLa Kyoto GFP-Nup107 derived stable cell were purchased
696 from CSL cell bank. AID-NUP358 DLD-1 (colorectal adenocarcinoma epithelial cells) cells
697 and AID-NUP358 HTC116 (human colon cancer cells) cells were generous gifts from Mary
698 Dasso (National Institutes of Health). hTERT-RPE1(Human retinal pigment epithelial-1)
699 cells was a generous gift from Juliette Godin (IGBMC). Control human fibroblasts and FXS
700 patient-derived fibroblasts were previously reported[35].
701 mCherry-Nup133 knock-in HeLa Kyoto cell lines were generated using CRISPR/Cas9
702 genome editing system as described previously[2]. The guide RNAs (gRNA) were designed
703 as described previously[3], and cloned into pX330-P2A-EGFP through ligation using T4
704 ligase (New England Biolabs). The donor constructs used as templates for homologous
705 recombination to repair the Cas9-induced double-strand DNA breaks were generated by
706 cloning into a pUC57 vector the Nup133 DNA fragments upstream and downstream of the
707 CRISPR target sequences and the sequence for mCherry, assembled using Exonuclease
708 Ⅲ(Takara) way. HeLa Kyoto cells were transfected for 24h and GFP positive cells were
709 collected by FACS (BD FACS Aria II), cultured for 2 days and seeded with FACS into 96-
710 well plates. Single-cell clones of mCherry-Nup133 knock-in were validated by Western blot
711 and sequencing of PCR-amplified targeted fragment by Sanger sequencing (GATC). The
712 sequences of gRNA and the primers used for plasmid generation are provided in
713 Supplementary Table 1.

714 UBAP2L knock-out (KO) in mCherry-Nup133 knock-in HeLa Kyoto cell lines were
715 generated using CRISPR/Cas9 genome editing system as described previously[2]. Two
716 guide RNAs (gRNA) were designed using the online software Benchling
717 (https://www.benchling.com/), and cloned into pX330-P2A-EGFP/RFP through ligation
718 using T4 ligase (New England Biolabs). mCherry-Nup133 knock-in HeLa Kyoto cells were
719 transfected for 24h and GFP and RFP double positive cells were collected by FACS (BD
720 FACS Aria II), cultured for 2 days and seeded with FACS into 96-well plates. UBAP2L KO
721 single-cell clones were validated by Western blot and sequencing of PCR-amplified
722 targeted fragment by Sanger sequencing (GATC). The sequences of gRNA are provided
723 in Supplementary Table 1.
724 All cell lines were cultured at 37°C in 5 % CO2 humidified incubator. HeLa Kyoto and its
725 derived cell lines were cultured in Dulbecco's Modified Eagle Medium (DMEM) (4.5 g/L
726 glucose) supplemented with 10 % fetal calf serum (FCS), 100 U/ml Penicillin + 100 µg/ml
727 Streptomycin. U2OS cell lines were cultured in DMEM (1 g/L glucose) supplemented with
728 10 % FCS, Non-Essential Amino Acids + Sodium Pyruvate 1 mM + Gentamicin 40 µg/mL.
729 DLD-1 cell lines were cultured in DMEM (1 g/L glucose) supplemented with 10 % FCS, 100
730 U/ml penicillin, and 100 µg/ml streptomycin. HTC116 cell lines were cultured in McCoy's
731 5A medium +10 % FCS +100 U/ml penicillin, and 100 µg/ml streptomycin. hTERT-RPE1
732 cells were cultured in Dulbecco's modified Eagle medium (DMEM) F-12 supplemented with
733 10% FCS, 0.01 mg/ml hygromycin B.
734

735 **Cell treatments and cell cycle synchronization**

736 To induce the formation of the cytoplasmic AL foci by microtubule depolymerization, the
737 cells were incubated with 10 µM nocodazole (Sigma M1404-50MG) in culture media for 90
738 min at 37°C. To inhibit autophagy, the cells were incubated with 30 nM bafilomycin (Sigma,
739 B1793-10UG) in culture media for 12h at 37°C. Cells were synchronized in early G1 by the
740 addition of thymidine (Sigma, T1895) at 2 mM for 16h. Cells were synchronized in mitotic
741 phase by double thymidine block and release (DTBR) protocol. Cells were treated with 2
742 mM thymidine for 16h, washed out (three times with warm thymidine-free medium), then
743 released in fresh thymidine-free culture medium for 8h, treated with 2 mM thymidine for
744 16h again, washed out, and then released in fresh thymidine-free culture medium for 9h.
745

746 **Immunofluorescence**

747 Cells were plated on 9-15 mm glass coverslips (Menzel Glaser) in 12- or 24- well tissue
748 culture plates. For immunofluorescence, cells were washed twice with PBS before being
749 fixed with 4 % paraformaldehyde (PFA, Electron Microscopy Sciences 15710) in PBS for
750 15-20 min at room temperature. Cells were washed three times for 5 min in PBS before
751 permeabilization for 5 min with 0.5 % NP-40 (Sigma) in PBS. Cells were washed three
752 times for 5 min in PBS before blocking for 1h at room temperature with 3 % BSA in PBS-
753 Triton 0.01 % (Triton X-100, Sigma, T8787). Cells were then incubated with primary
754 antibody in blocking buffer (3 % BSA in PBS-Triton 0.01 %) for 1h at room temperature.
755 Cells were washed three times with PBS-Triton 0.01 % gently shaking for 10 min before
756 incubated with secondary antibody in blocking buffer for 1h at room temperature in the dark.
757 After incubation, cells were washed 3 times with PBS-Triton 0.01 % for 10 min each time

758 with shaking in the dark, and then glass coverslips were mounted on glass slides using
759 MOWIOL containing 0.75 µg/ml DAPI (Calbiochem) and imaged with 100X, 63X or 40X
760 objectives using Zeiss epifluorescence microscope or confocal microscope Leica Spinning
761 Disk Andor/Yokogawa.
762
763 **Live-cell imaging**
764 For live-cell microscopy, cells were grown on 35/10 mm 4 compartment glass bottom
765 dishes (Greiner Bio-One, 627871) or µ-Slide 8 well glass bottom (Ibidi, 230928). Before
766 photography, cells were treated with SiR-DNA (Spirochrome, SC007) according to the
767 manufacturer's instructions. Live cell microscopy was performed using a confocal
768 microscope Leica/Andor/Yokogawa spinning disc, Leica CSU-W1 spinning disc, or Nikon
769 PFS spinning disc with a 40X or 63X objectives with Live Data Mode equipped with
770 automated temperature.
771 In particular, for nucleoporin foci' dynamics assays under normal growth conditions, HeLa
772 Kyoto GFP-Nup107 derived stable cell were analyzed by Leica CSU-W1 spinning disk
773 (63X NA 1.4 oil objective) for 9h. Z-stacks (7 µm range, 1 µm step) were acquired every 5
774 min and movies were made with maximum intensity projection images for every time point
775 shown at speed of 7 frames per second. For nucleoporin foci' dynamics assays under
776 microtubule depolymerization, HeLa Kyoto GFP-Nup107 derived stable cell were arrested
777 in S phase by thymidine block and microtubule depolymerization and nucleoporin
778 aggregation were induced by 10 µM nocodazole addition. For nucleoporin foci' dynamics
779 assays under FXR1 knockdown (KD) or UBAP2L KD conditions, HeLa Kyoto GFP-Nup107
780 derived stable cell were treated with the indicated siRNAs for 48 h before imaging.
781 For nucleoporin foci and ER' dynamics assays, HeLa Kyoto GFP-Nup107 derived stable
782 cell were transfected with the pQCXIP-mScarlet-ER for 24 h and analyzed by Nikon PFS
783 spinning disk (100X NA1.4 oil objective) for 5h where images were acquired every 20s
784 (without Z-stacks) or were analyzed for 9h where images were acquired every 2 min
785 (without Z-stacks).
786 For photoactivatable nucleocytoplasmic shuttling, AID-NUP358 DLD-1 were transfected
787 with the NLS-mCherry-LEXY (pDN122) for 24h and analyzed by Leica Sp5 confocal
788 inverted microscope (DMI6000) system (40X NA1.3 oil objective). The circular region of
789 interest (ROI; ~38 µm2) was placed onto single, selected cells. The ROI was scanned with
790 a 458-nm laser beam for 10 min following a 20-min dark-recovery phase. The mCherry
791 signal was imaged in parallel every 10s for 30 min using the 561-nm laser line for excitation.
792
793 **Single molecule localization microscopy**
794 For super-resolution imaging using single molecule localization microscopy (SMLM), cells
795 were plated on 35 mm glass bottom dish with 14 mm micro-well #1.5 cover glass (Cellvis).
796 Samples were prepared as described above for immunofluorescence but were not
797 mounted using MOWIOL and were stored in PBS.
798 The imaging was performed as previously described, using the splitSMLM method[4] for
799 multi-color single molecule localization microscopy (SMLM) based on a dichroic image
800 splitter. In brief, the immunolabeled samples were mounted in imaging buffer containing
801 200 U/ml glucose oxidase (G2133, Sigma), 1000 U/ml catalase (C1345, Sigma), 10 % w/v

802 glucose, 200 mM Tris-HCl pH 8.0, 10 mM NaCl, 50 mM MEA (30080, Sigma), with addition
803 of 2 mM COT (138924, Sigma). The buffer optimizes the performance of the fluorophores
804 AF647, CF660C, and CF680, for three-color direct stochastic optical reconstruction
805 microscopy (dSTORM). Imaging was then performed on a modified Leica SR GSD system,
806 with a HCX PL APO 160X/1.43 Oil CORR TIRF PIFOC objective. The acquisitions began
807 with a pumping phase, during which the sample was illuminated with the 642 nm fiber laser
808 (MBP Communication Inc.) but the fluorescence was not recorded due to a very high
809 density of fluorophores in a bright state. The image collection started when the density of
810 fluorophores dropped to a level that allowed observation of individual molecules and in
811 case of emitter depletion, the sample was additionally illuminated with a 405 nm diode
812 laser (Coherent Inc.) to increase the emitter density (back-pumping). The resulting
813 emission was split with an Optosplit II (Cairn Research) image splitter, attached to a
814 camera port of the microscope, and containing a Chroma T690LPXXR dichroic mirror. This
815 creates a long and short wavelength channel on the Andor iXon Ultra 897 EMCCD camera
816 attached to the image splitter. Each fluorophore thus shows a characteristic brightness
817 ratio between the two channels, enabling the separation of spectrally different fluorophore
818 species (i.e., spectral demixing)[4]. Localization of the single molecules in both channels
819 was performed using the Leica LAS X software with the “direct fit” fitting method. The
820 localization tables were then exported and further processed using the SharpVisu
821 software[5–7] and the SplitVisu plugin[4]. This accounts for spectral demixing, correction of
822 chromatic errors, drift-correction, and the reconstruction of super-resolution images. A pixel
823 size of 10 nm was used to reconstruct the super-resolution images from 2D-histograms of
824 single-molecule coordinates. For the single-color imaging without image-splitter, the
825 images were recorded with an Andor iXon+ EMCCD camera, attached to the second
826 camera port of the microscope. Data was then processed as already described, using the
827 Leica LAS X and SharpVisu software, while omitting the spectral demixing steps in the
828 SplitVisu plugin.
829

830 **Correlative light and electron microscopy**

831 Cells were grown on carbon coated sapphire disks (3 mm diameter, 50 μm thickness,
832 Wohlwend GmbH, art. 405) and high pressure frozen (HPM010, AbraFluid) in their culture
833 medium. Freeze substitution was performed in a Leica EM-AFS2 with 0.1 % uranyl acetate
834 in dry acetone for 24h at -90°C. The temperature was then raised to -45°C over 9h (slope
835 5 degrees / hour) and the samples were further incubated at this temperature for 5h to
836 increase electron contrast. After rinsing in acetone, the samples were infiltrated with
837 increasing concentrations of Lowicryl HM20 (Polysciences Inc.), while raising the
838 temperature to -25°C. Finally, the blocks were polymerized using UV light. After removal of
839 the sapphire disks from the block surface, 300 nm sections were cut parallel to the block
840 surface using an ultramicrotome (UC7, Leica Microsystems). The sections were collected
841 on carbon coated mesh grids (S160, Plano).
842 Fluorescence imaging of the sections was carried out with a widefield microscope
843 (Olympus IX81), equipped with a 100X 1.40 NA Plan-Apochromat objective, placing the
844 grids in water in a glass bottom dish (Mattek). After light microscopy acquisition, the grids
845 were post-stained with 2 % uranyl acetate in 70 % methanol and Reynold’s lead citrate.

Electron microscopy (EM) was performed using a Tecnai F30 transmission electron microscope (Thermo Fisher) at 300kV acceleration voltage. The grid squares that were previously imaged at the light microscope (LM) were mapped at low mag. After registration with the LM image, TEM tomography was performed on the areas of interest using the software package SerialEM[8]. Tomograms were reconstructed with IMOD[9]. Correlation between LM and EM images was done with the plugin ec-CLEM[10] of the software platform Icy[11], using features of the samples that could be identified in both imaging modalities.

Image analysis

Image quantification analysis was performed using ImageJ or CellProfiler software. In particular, the presence of Nups foci was confirmed by eyes from two individuals. For nuclear size or nuclear envelope intensity analysis of Nups, CellProfiler software was used. Briefly, the Prewitt Edge Finder method was used to enhance the edges in a DAPI image, and then a nucleus size threshold is set to automatically identify nuclei. This allowed identification and measurement of nuclei area, morphology factor and mean nuclear intensity for the desired channel. The software's parameter measurements were exported to an Excel file and statistically analyzed. For the size of Nups foci, ImageJ software was used. In brief, the Nups channel was thresholded in ImageJ and then the size of the Nups foci was calculated by analyzing particles (size 1-100). AL foci that were considered “large” had a size bigger than 0,3 μm^2.

For co-localization analysis of RanBP2 and Nups in cytoplasm, CellProfiler software was used. The Prewitt Edge Finder method was used to enhance the edges in a DAPI image, and then Nuclei, RanBP2 and different Nups were identified according to the corresponding channels. The cytoplasmic fraction of RanBP2 and Nups was identified using MaskObjects module. Co-localization analysis of RanBP2 and Nups in cytoplasm was conducted by MeasureObjectOverlap module. The software's parameter measurements were exported to an Excel file and statistically analyzed. For nuclear envelope or cytoplasm intensity of Ran, ImageJ was used. The ROI of cell and nuclei were selected based on tubulin and DAPI channels, and the ROI of cytoplasm was selected by XOR of cell and nuclei. Finally, the mean gray value of the nuclei and cytoplasm was measured.

For AL-NPCs analysis in cytoplasm, AL-NPCs were recognized by Nup133 surrounding Nup62 signals. The number of AL-NPCs was counted by eyes from two individuals. For the measurement of NPCs density on the nuclear membrane, ImageJ software was used. Briefly, the image of the Nup62 channel were converted to 32 bits using ImageJ and then filtered using Gaussin blur (2). The nuclear region was manually selected and then find maxima (10) was performed to obtain the area of the selected region and the number of NPCs.

For protein import and export assay analysis, ImageJ software was used. Briefly, the ROI within uniform distribution of NLS-mCherry-LEXY signal was selected in the nuclear region, and the measurement of the mean gray value of the same ROI in each frame (time sequentially) was performed by multi-measure option.

For calculation of the mean fluorescence intensity of Nups as a function of distance from the nucleus a custom Python script was used with help of the scikit-image module[12]. The

890 nucleus and the nuclear envelope were identified using the RanBP2 channel following well-
891 established procedures[13,14]. Similarly, the region corresponding to the ER was determined
892 from the mScarlet-ER channel. Regions corresponding to RanBP2 foci were detected
893 using the scikit-image method blob_log for blob detection. The analyzed region for Climp63
894 and mScarlet-ER corresponded to the ER region excluding the nucleus. The analyzed
895 region for the RanBP2 foci corresponded to the blob regions that fall within the ER region
896 excluding the nucleus. For each pixel in the analyzed regions, the minimum Euclidean
897 distance to any nuclear envelope pixel was taken as the distance from the nucleus. Given
898 the intensity-distance pairs for each pixel, the pixels were binned for the distance and the
899 mean pixel intensity determined for each bin. The obtained histograms were finally
900 normalized for purpose of comparison.
901

902 **Protein sample preparation and Western blotting**

903 After centrifugation at 250 g for 3 minutes at 4°C, cells were washed twice with cold PBS,
904 and lysates were prepared using 1X RIPA buffer (50 mM Tris-HCl pH 7.5, 150 mM NaCl,
905 1 % Triton X-100, 1 mM EDTA, 1 mM EGTA, 2 mM Sodium pyrophosphate, 1 mM Na3VO4
906 and 1 mM NaF) supplemented with protease inhibitor cocktail (Roche) and incubated on
907 ice for 30-60 min. After centrifugation at 16 000 g for 15 min at 4°C, the supernatant was
908 transferred to the new clean Eppendorf tubes, and the total protein concentration was
909 measured with a Bio-Rad Protein Assay kit (Bio-Rad). Separation of cytoplasm and
910 nucleus was done using the NE-PER nuclear and cytoplasmic extraction reagent kit
911 (Thermo Scientific™, 78833). Protein samples were boiled for 10 min at 95°C in 1X
912 Laemmli buffer (LB) with β-Mercaptoethanol (BioRad, 1610747).
913 SDS-PAGE of proteins was done using pre-cast 4-12 % Bis-Tris gradient gels (Thermo
914 Scientific, NW04120BOX) or pre-cast NuPAGE™ 3-8 % Tris-Acetate gradient Gels
915 (Thermo Scientific, EA0378BOX). Proteins were transferred to a polyvinylidene difluoride
916 (PVDF) membrane (Millipore, IPFL00010) using wet transfer modules (BIO-RAD Mini-
917 PROTEAN® Tetra System). Membranes were blocked in 5 % bovine serum albumin (BSA,
918 Millipore, 160069), or 5% non-fat milk powder mixed with 3 % BSA resuspended in TBS-T
919 for 1h at room temperature, followed by incubation with primary antibodies diluted in TBS-
920 T 5 % BSA/5 % milk overnight at 4°C or 1h at room temperature and secondary antibodies
921 diluted in TBS-T 5 % BSA/5 % milk at room temperature. Membranes were imaged using
922 SuperSignal West Pico (Pierce, Ref. 34580).
923

924 **Immunoprecipitation**

925 Cell lysates were prepared for immunoprecipitations (IP) as described above. Lysates were
926 adjusted to equal volume and concentration. For endogenous IP experiments, lysates were
927 incubated with IgG or target-specific antibodies overnight at 4°C with rotation, and then
928 incubated with protein G sepharose 4 Fast Flow beads (GE Healthcare Life Sciences) for
929 4h at 4°C with rotation. Before using, beads were blocked with 3 % BSA diluted in 1X RIPA
930 buffer and incubated for 2h at 4°C with rotation. The incubated IgG/ specific antibodies-
931 samples-beads were washed with washing buffer (25 mM Tris-HCl pH 7.5, 300 mM NaCl,
932 0.5 % Triton X-100, 0.5 mM EDTA, 0.5 mM EGTA, 1 mM Sodium pyrophosphate, 0.5 mM
933 Na3VO4 and 0.5 mM NaF) or TBS-T 4 to 6 times.

For GFP-IP/HA-IP experiments, GFP-Trap A agarose beads (Chromotek) or Pierce™ anti-HA Magnetic Beads (Thermo Scientific 88836) were used. Cells expressing GFP- or HA-tagged plasmids for at least 24h before lysis were used. Lysates were incubated with beads for 4h at 4°C with rotation, and then washed with washing buffer (25 mM Tris-HCl pH 7.5, 300 mM NaCl, 0.5 % Triton X-100, 0.5 mM EDTA, 0.5 mM EGTA, 1 mM Sodium pyrophosphate, 0.5 mM Na3VO4 and 0.5 mM NaF) or TBS-T 4 to 6 times.

Gel fractionation

To calibrate the Superose 6 Increase 3.2/300 column, the gel filtration standard (Bio-Rad, Catalog # 1511901) was rehydrated and diluted to 1.5 mg/mL according to the instruction of the manufacturer. The column was equilibrated using buffer comprising 15 mM pH 7.5 Tris, 15 mM NaCl, 60 mM KCl, 340 mM sucrose, 0.15 mM spermine, 0.5 mM spermidine, 0.5 % Triton X-100, 1 mM NaF, 10 mM DTT. The standard sample (50 µL) was separated by a flow rate of 0.015 ml/min. Kav values for the standards were calculated. The calibration curve of Kav versus the logarithm of their molecular weights was determined as follows:

$$K_{av} = \frac{Ve - Vo}{Vt - Vo}$$

where Ve= elution volume of the protein

Vo= column void volume = 0.8 mL

Vt = total bed volume = 2.4 mL

HeLa cell cytosolic and nuclear fractions were prepared as described above. For the gel filtration of the Hela cell cytosol extraction sample, a 2.4-mL Superose 6 Increase 3.2/300 column (Cytiva) was equilibrated using buffer comprising 15 mM pH 7.5 Tris, 15 mM NaCl, 60 mM KCl, 340 mM sucrose, 0.15 mM spermine, 0.5 mM spermidine, 0.5 % Triton X-100, 1 mM NaF, 10 mM DTT. For the gel filtration of the Hela cell nuclear fraction sample, a 2.4-ml Superose 6 Increase 3.2/300 column (Cytiva) was equilibrated using buffer comprising 50 mM Tris 7.5, 1 % NP-40, 150 mM NaCl, 1mM EDTA, 0.1 % SDS, 0.5 % sodium deoxycholate. The cytosolic and nuclear fractions (typically 1~3 mg/ml) were clarified by centrifugation for 15 minutes at 12,000 X g before loading to the equilibrated gel filtration column. Samples were separated by a flow rate of 0.017 ml/min, and 50 µL fractions were collected for Western blot analysis (typically collects from 1.2mL to 2.4mL).

LC-MS/MS analysis

MS grade Acetonitrile (ACN), MS grade H2O and MS grade formic acid (FA) were from ThermoFisher Scientific (Waltham, MA, USA). Sequencing-grade trypsin/Lys C mix was from Promega (Madison, WI, USA). Trifluoroacetic acid (TFA) and ammonium bicarbonate (NH4HCO3) were from Sigma-Aldrich (Saint-Louis, MO, USA).

For sample preparation prior to LC-MS/MS analysis beads from immunoprecipitation experiments were incubated overnight at 37°C with 20 µL of 50 mM NH4HCO3 buffer containing 1 µg of sequencing-grade trypsin/Lys C mix. The digested peptides were loaded and desalted on evotips provided by Evosep (Odense, Denmark) according to manufacturer's procedure before LC-MS/MS analysis. For LC-MS/MS acquisition samples

were analyzed on a timsTOF Pro 2 mass spectrometer (Bruker Daltonics, Bremen, Germany) coupled to an Evosep one system (Evosep, Odense, Denmark) operating with the 30SPD method developed by the manufacturer. Briefly, the method is based on a 44-min gradient and a total cycle time of 48 min with a C18 analytical column (0.15 x 150 mm, 1.9µm beads, ref EV-1106) equilibrated at 40°C and operated at a flow rate of 500 nL/min. H2O/0.1 % FA was used as solvent A and ACN/ 0.1 % FA as solvent B. The timsTOF Pro 2 was operated with a DIA-PASEF method comprising 12 pydiAID frames with 3 mass windows per frame resulting in a cycle time of 0.975 seconds as described in Bruker application note LCMS 218.

For data analysis MS raw files were processed using Spectronaut 18 (Biognosys, Switzerland). Data were searched against the SwissProt Homo Sapiens database (downloaded 07 2023, 20423 entries). Specific tryptic cleavages were selected and a maximum of 2 missed cleavages were allowed. The following post-translational modifications were considered for identification: Acetyl (Protein N-term) and Oxidation (M) as variables. Identifications were filtered based on a 1 % precursor and protein Qvalue cutoff threshold. The protein LFQ method was set to automatic and the quantity was set at the MS2 level with a cross-run normalization applied. Multivariate statistics on protein measurements were performed using Qlucore Omics Explorer 3.9 (Qlucore AB, Lund, SWEDEN). A positive threshold value of 1 was set to allow a log2 transformation of abundance data for normalization i.e. all abundance data values below the threshold are replaced by 1 before transformation. The transformed data were finally used for statistical analysis i.e. the evaluation of differentially present proteins between two groups using a bilateral Student's t-test. A p-value better than 0.05 was used to filter differential candidates.

Experimental design, data acquisition and statistical analysis

All experiments were done in a strictly double-blind manner. At least three independent biological replicates were performed for each experiment (unless otherwise indicated) and image quantifications were carried out in a blinded manner. Curves and graphs were made using GraphPad Prism and Adobe Illustrator software. Data was analyzed using one-sample two-tailed T-test or two sample unpaired two-tailed T-test (two-group comparison or folds increase relative to the control, respectively) or one-way ANOVA. A p-value less than 0.05 (typically ≤ 0.05) was considered statistically significant and stars were assigned as follows: *P < 0.05, **P < 0.01, ***P < 0.001, ****P < 0.0001.

References

1. Zouiouich, M. *et al.* MOSPD2 is an endoplasmic reticulum-lipid droplet tether functioning in LD homeostasis. *J Cell Biol* **221**, e202110044 (2022).
2. Ran, F. A. *et al.* Genome engineering using the CRISPR-Cas9 system. *Nat Protoc* **8**, 2281–2308 (2013).
3. Chou, Y.-Y. *et al.* Inherited nuclear pore substructures template post-mitotic pore assembly. *Dev Cell* **56**, 1786-1803.e9 (2021).
4. Andronov, L., Genthial, R., Hentsch, D. & Klaholz, B. P. splitSMLM, a spectral demixing method for high-precision multi-color localization microscopy applied to nuclear pore complexes. *Commun Biol* **5**, 1100 (2022).

5. Andronov, L., Lutz, Y., Vonesch, J.-L. & Klaholz, B. P. SharpViSu: integrated analysis and segmentation of super-resolution microscopy data. *Bioinformatics* **32**, 2239–2241 (2016).
6. Andronov, L. *et al.* 3DClusterViSu: 3D clustering analysis of super-resolution microscopy data by 3D Voronoi tessellations. *Bioinformatics* **34**, 3004–3012 (2018).
7. Andronov, L., Vonesch, J.-L. & Klaholz, B. P. Practical Aspects of Super-Resolution Imaging and Segmentation of Macromolecular Complexes by dSTORM. *Methods Mol Biol* **2247**, 271–286 (2021).
8. Mastronarde, D. N. Automated electron microscope tomography using robust prediction of specimen movements. *J Struct Biol* **152**, 36–51 (2005).
9. Kremer, J. R., Mastronarde, D. N. & McIntosh, J. R. Computer visualization of three-dimensional image data using IMOD. *J Struct Biol* **116**, 71–76 (1996).
10. Paul-Gilloteaux, P. *et al.* eC-CLEM: flexible multidimensional registration software for correlative microscopies. *Nat Methods* **14**, 102–103 (2017).
11. de Chaumont, F. *et al.* Icy: an open bioimage informatics platform for extended reproducible research. *Nat Methods* **9**, 690–696 (2012).
12. van der Walt, S. *et al.* scikit-image: image processing in Python. *PeerJ* **2**, e453 (2014).
13. Boni, A. *et al.* Live imaging and modeling of inner nuclear membrane targeting reveals its molecular requirements in mammalian cells. *J Cell Biol* **209**, 705–720 (2015).
14. Miura, K. Measurements of Intensity Dynamics at the Periphery of the Nucleus. in *Bioimage Data Analysis Workflows* (eds. Miura, K. & Sladoje, N.) 9–32 (Springer International Publishing, Cham, 2020). doi:10.1007/978-3-030-22386-1_2.

1047 ## Figures and figure legends

Figure 1

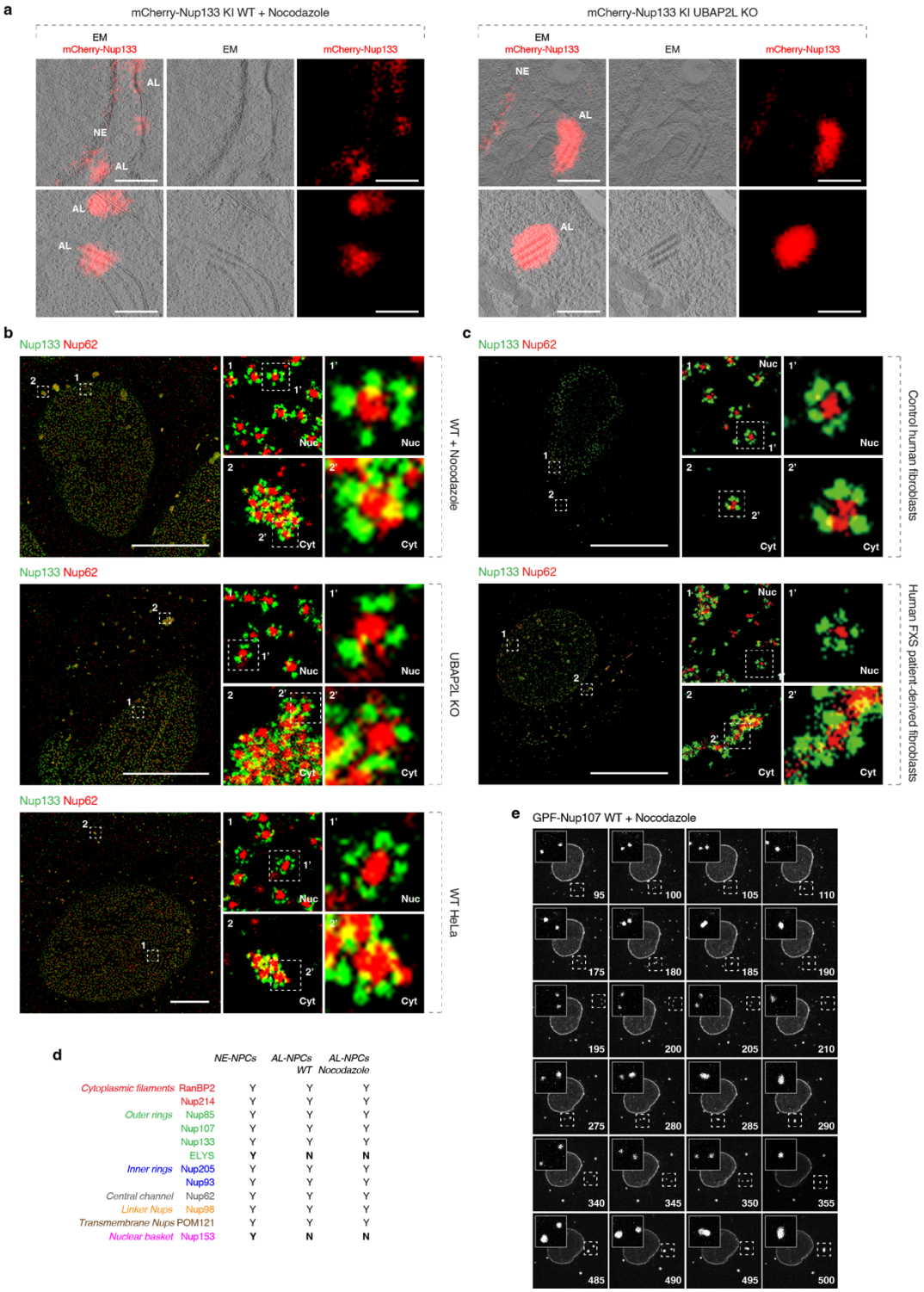

1048

1049

1050 **Fig. 1. Single molecule localization microscopy identifies the presence of AL in a**
1051 **variety of somatic cells**

1052 a, Representative correlative light and electron microscopy (CLEM) of HeLa cells. The left
1053 and right graph represents the condition of nocodazole treatment (10 μM, 90 min) and
1054 UBAP2L knockout (KO), respectively. mCherry fluorescence is concentrated at densely

1055 packed NPCs on stacked ER sheets in the cytoplasm corresponding to AL, and is also
1056 observed at NE. Scale bars, 1 µm.
1057 b, Representative splitSMLM images depicting NPCs on the nuclear (Nuc) surface and
1058 NPCs located in the cytoplasm (Cyt) in HeLa cells treated with nocodazole (10 µM, 90 min),
1059 UBAP2L KO HeLa cells and in WT HeLa cells. Nup133 signal labels the cytoplasmic and
1060 nuclear rings of the NPC, the localization of the central channel is visualized by Nup62.
1061 Note that clusters of AL-NPCs in WT cells are smaller relative to other conditions. The
1062 magnified framed regions are shown in the corresponding numbered panels. Scale bars,
1063 5 µm.
1064 c, Representative splitSMLM images depicting NPCs on the nuclear (Nuc) surface and
1065 NPCs located in the cytoplasm (Cyt) in normal human fibroblasts and in FXS patient-
1066 derived fibroblasts. The magnified framed regions are shown in the corresponding
1067 numbered panels. Scale bars, 5 µm.
1068 d, Summary of composition of NE-NPCs and AL-NPCs. Different colors represent specific
1069 NPC subcomplexes. “Y” indicates presence and “N” indicates absence of indicated Nups.
1070 e, 2xZFN-mEGFP-Nup107 HeLa cells treated with nocodazole were analyzed by live video
1071 spinning disk confocal microscopy. Selected representative frames of the movies are
1072 depicted, and time is shown in minutes after nocodazole addition at the timepoint 0. The
1073 magnified framed regions are shown in the upper left corner. Scale bars, 5 µm.
1074

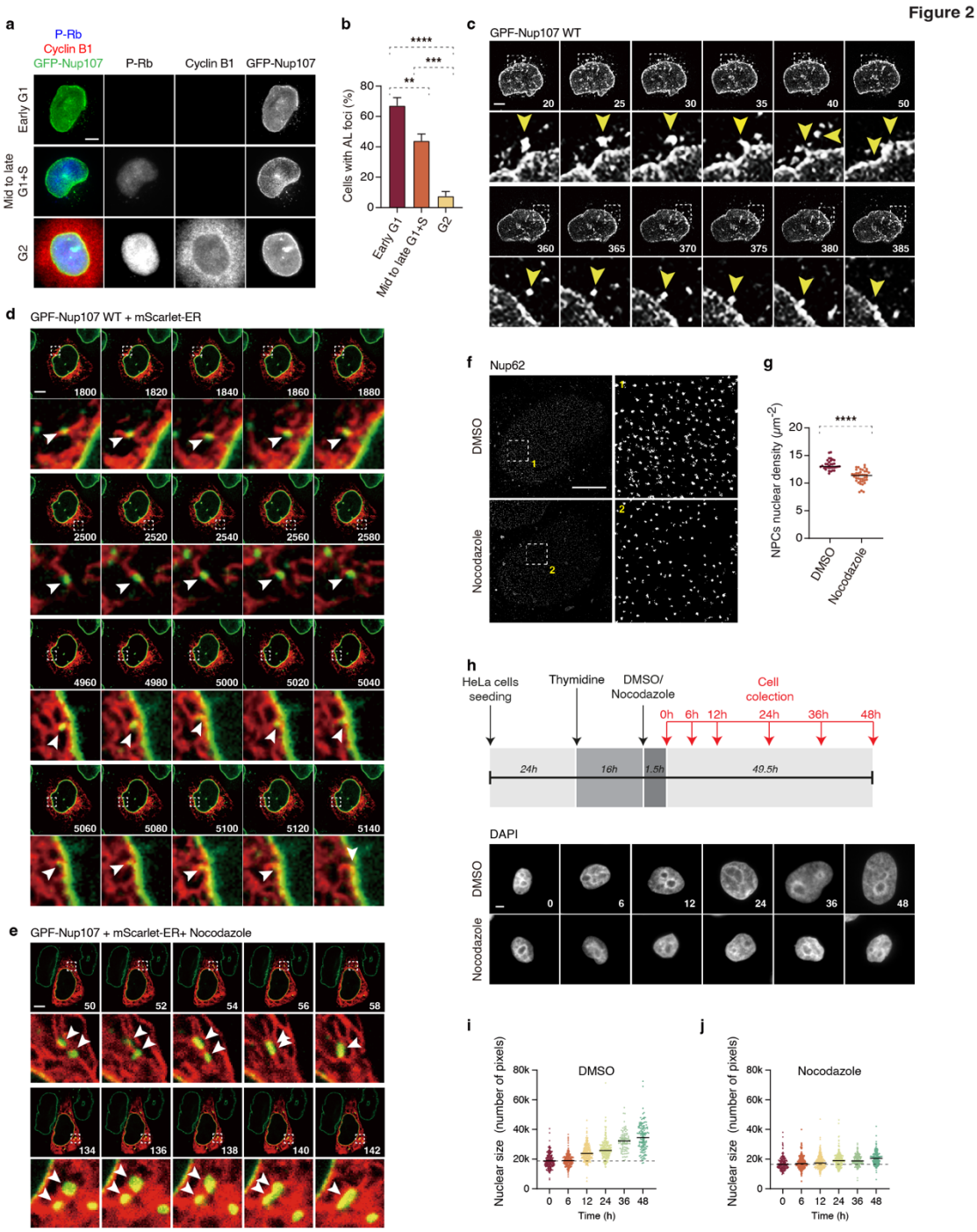

Fig. 2. AL merge with NE in early interphase under normal growth conditions

a, b, Representative images of asynchronously proliferating 2xZFN-mEGFP-Nup107 HeLa cells co-labelled with anti-p-Rb (blue) and anti-cyclin B1 (red) antibodies (a). The percentage of cells with Nup foci in p-Rb and cyclin B1 negative cells (early G1), p-Rb positive and cyclin B1 negative cells (mid to late G1+S), and p-Rb and cyclin B1 positive cells (G2) was quantified in (b), and at least 200 cells per condition were analyzed (mean ± SD, **P < 0.01; ***P < 0.001; ****P < 0.0001; N = 3). Scale bars, 5 μm.

c, 2xZFN-mEGFP-Nup107 HeLa cells were synchronized by double thymidine block, released and analyzed by live video spinning disc confocal microscopy. Selected

representative frames of the movies are depicted, and time is shown in minutes after the mitotic exit at the timepoint 0. The magnified framed regions are shown in the lower panels. Yellow arrows point to cytosolic NPCs merging with the NE. Scale bars, 5 μm.

d, 2xZFN-mEGFP-Nup107 HeLa cells expressing ER marker plasmid mScarlet-ER were analyzed by live video spinning disk confocal microscopy. The selected representative frames of the movies are depicted, and time is shown in seconds. The magnified framed regions are shown in the lower panels. White arrows point to the movement of cytosolic NPCs along the ER and the incorporation of cytosolic NPCs into the NE along the junction of the ER and the NE. Scale bars, 5 μm.

e, 2xZFN-mEGFP-Nup107 HeLa cells expressing ER marker plasmid mScarlet-ER were treated with Nocodazole (10 μM) and analyzed by live video spinning disk confocal microscopy. The selected representative frames of the movies are depicted, and time is shown in minutes after nocodazole addition at the timepoint 0. The magnified framed regions are shown in the lower panels. White arrows point to fusing AL foci. Scale bars, 5 μm.

f, g, Representative SMLM immunofluorescence images of Nup62 at the nuclear surface in DMSO or nocodazole treated (10 μM, 90 min) HeLa cells. The magnified framed regions are shown in the right panels (f). The nuclear density of NPCs (Nup62) in cells was quantified in (g) (mean ± SD, ****$P < 0.0001$, unpaired two-tailed t test; counted 40 cells per cell line). Scale bars, 5 μm

h-j, Scheme of the experimental setup (h). HeLa cells were synchronized and arrested at S phase by thymidine treatment (16h), treated with nocodazole (10 μM) and fixed at indicated time points. Representative images of cell nuclei are shown in (h) and the nuclear size was quantified in (i, j). At least 200 cells per condition were analyzed (N = 3). Scale bars, 5 μm.

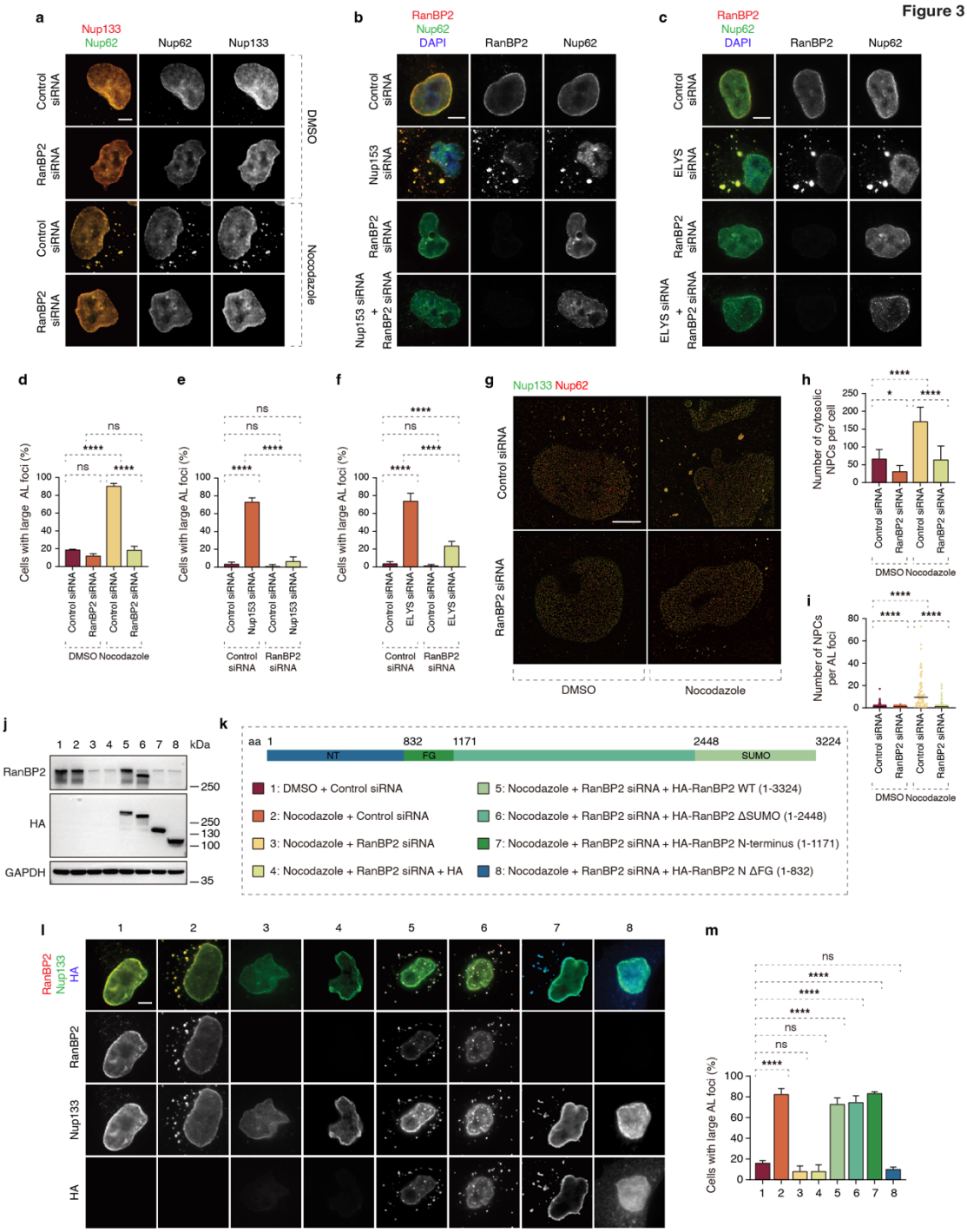

Fig. 3. RanBP2 is required for the formation and maintenance of AL in somatic cells

a, d, Representative images of HeLa cells treated with the indicated siRNAs (48h) and subsequently by nocodazole (10 μM) or DMSO (90 min). Cells were co-labelled with anti-Nup62 (green) and anti-Nup133 (red) antibodies (a) to detect AL-NPC foci. The number of cells with big AL foci were quantified in (d), and at least 1000 cells per condition were analyzed (mean ± SD, ns: not significant, ****P < 0.0001; N = 3). Scale bars, 5 μm.

b, c, e, f, Representative images of HeLa cells treated with the indicated siRNAs (48h). Cells were co-labelled with anti-Nup62 (green) and anti-RanBP2 (red) antibodies (b, c) to detect AL-NPC foci. The percentage of cells with big AL foci were quantified in (e, f), and

1123 at least 300 cells per condition were analyzed (mean ± SD, ns: not significant, **P < 0.01;
1124 ****P < 0.0001; N = 3). Scale bars, 5 μm.
1125 g, h, i, Representative splitSMLM images of HeLa cells treated with the indicated siRNAs
1126 (48h) and subsequently by nocodazole (10 μM) or DMSO (90 min) depicting AL-NPCs in
1127 the cytoplasm. Cells were co-labelled with anti-Nup62 (green) and anti-Nup133 (red)
1128 antibodies (g). The number of single NPC-like complexes per single cell and the number
1129 of single NPC-like complexes in individual AL foci/cluster were quantified in (h, i),
1130 respectively. At least 6 cells per condition were analyzed (mean ± SD, *P < 0.1; ****P <
1131 0.0001; N = 3). Scale bars, 5 μm.
1132 j, k, l, m, Rescue experiments using different RanBP2 fragments. (j) shows the WB analysis
1133 of RanBP2 fragments under different experimental conditions summarized in (k).
1134 Representative images of HeLa cells treated with the indicated siRNAs, transfected with
1135 different RanBP2 fragments and treated with nocodazole (10 μM) or DMSO (90 min). Cells
1136 were co-labelled with anti-Nup133 (green), anti-RanBP2 (red) and anti-HA (blue)
1137 antibodies (l). The number of cells with large AL foci were quantified in (m), and at least
1138 300 cells per condition were analyzed (mean ± SD, ns: not significant, ****P < 0.0001; N =
1139 3). Scale bars, 5 μm.
1140

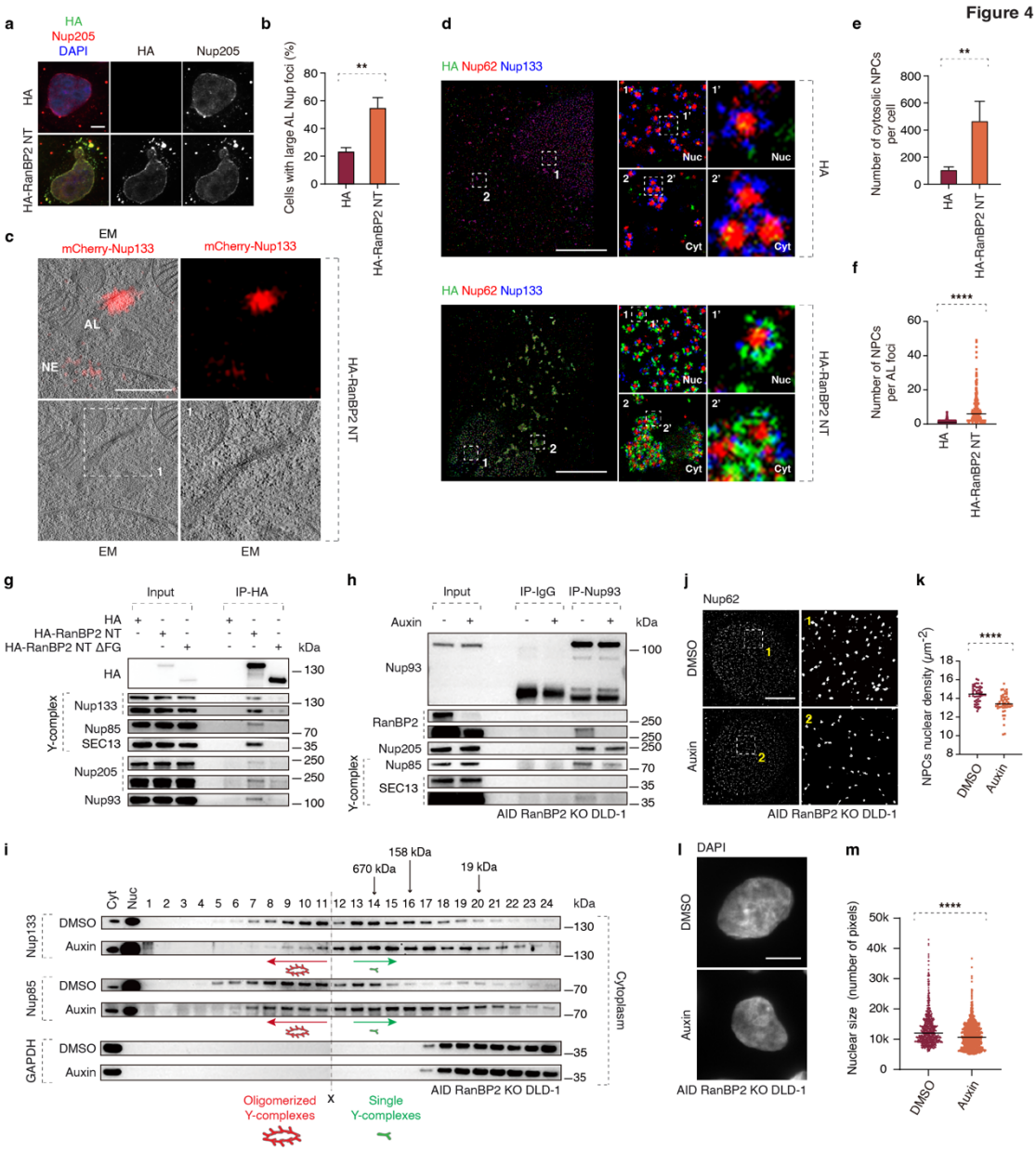

Fig. 4. RanBP2 ensures assembly of AL-NPCs through its N-terminal domain.

a, b, Representative images of HeLa cells transfected with HA or HA-RanBP2 N-terminal (NT) fragment. Cells were co-labelled with DAPI (blue) and anti-Nup205 (red) and anti-HA (green) antibodies (a). The number of cells with large AL foci was quantified in (b), and at least 300 cells per condition were analyzed (mean ± SD, **P < 0.01; N = 3). Scale bars, 5 μm.

c, Representative correlative light and electron microscopy (CLEM) of mCherry-Nup133-KI HeLa cells transfected with HA-RanBP2-NT fragment. The magnified framed regions are shown in the corresponding numbered panels. mCherry fluorescence is concentrated at densely packed AL-NPCs on stacked ER sheets in the cytoplasm, representing AL and is also observed at the NE. Scale bars, 1 μm.

d, e, f, Representative splitSMLM images depicting NPCs on the nuclear surface (Nuc) and NPCs in the cytoplasm (Cyt) in HeLa cells transfected with HA or HA-RanBP2-NT

fragment. Nup133 signal labels the cytoplasmic and nuclear rings of the NPC and the localization of the central channel is visualized by Nup62. The magnified framed regions are shown in the corresponding numbered panels (d). The number of single NPC-like complexes per cell and the number of single NPC-like complexes in a single AL foci/cluster were quantified in (e, f), respectively. At least 6 cells per condition were analyzed (mean ± SD, ***P < 0.001; ****P < 0.0001; N = 3). Scale bars, 5 µm.

g, Lysates of Hela cells expressing HA, HA-RanBP2-NT or HA-RanBP2-N ΔFG were immunoprecipitated using anti-HA magnetic beads (HA-IP) and analyzed by Western blot (at least 3 independent experiments).

h, Auxin-inducible degron (AID) RanBP2 KO DLD-1 cells were treated with auxin for 4h to deplete RanBP2 and lysates were immunoprecipitated using Nup93 antibody or IgG and analyzed by Western blot (at least 3 independent experiments).

i, Auxin-inducible degron (AID) RanBP2 KO DLD-1 cells were treated with DMSO or auxin for 4h to deplete RanBP2 and cytoplasmic fractions were prepared, separated on a Superose 6 gel filtration column and analyzed by Western blotting. Fraction 1 corresponds to the void and the elution of thyroglobulin (670 kDa), g-globulin (158 kDa) and myoglobulin markers 19 kDa are indicated. Green arrows point to fractions preferentially containing single Y-complexes, and red arrows indicate fraction with higher molecular weight, oligomerized Y-complexes. Note that depletion of RanBP2 reduced the abundance of oligomerized Y-complexes.

j, k, Representative SMLM immunofluorescence images of Nup62 at the nuclear surface in AID RanBP2 KO DLD-1 cells treated with DMSO or auxin for 4h to deplete RanBP2. The magnified framed regions are shown in the right panels (j). The nuclear density of NPCs (Nup62) in cells was quantified in (k) (mean ± SD, ****P < 0.0001, unpaired two-tailed t test; counted 50 cells per cell line). Scale bars, 5 µm

l, m, Representative images of cell nuclei in AID RanBP2 KO DLD-1 cells treated with DMSO or auxin for 4h to deplete RanBP2 are shown in (l) and the nuclear size was quantified in (m). At least 700 cells per condition were analyzed (mean ± SD, ****P < 0.0001, unpaired two-tailed t test; N = 3). Scale bars, 5 µm.

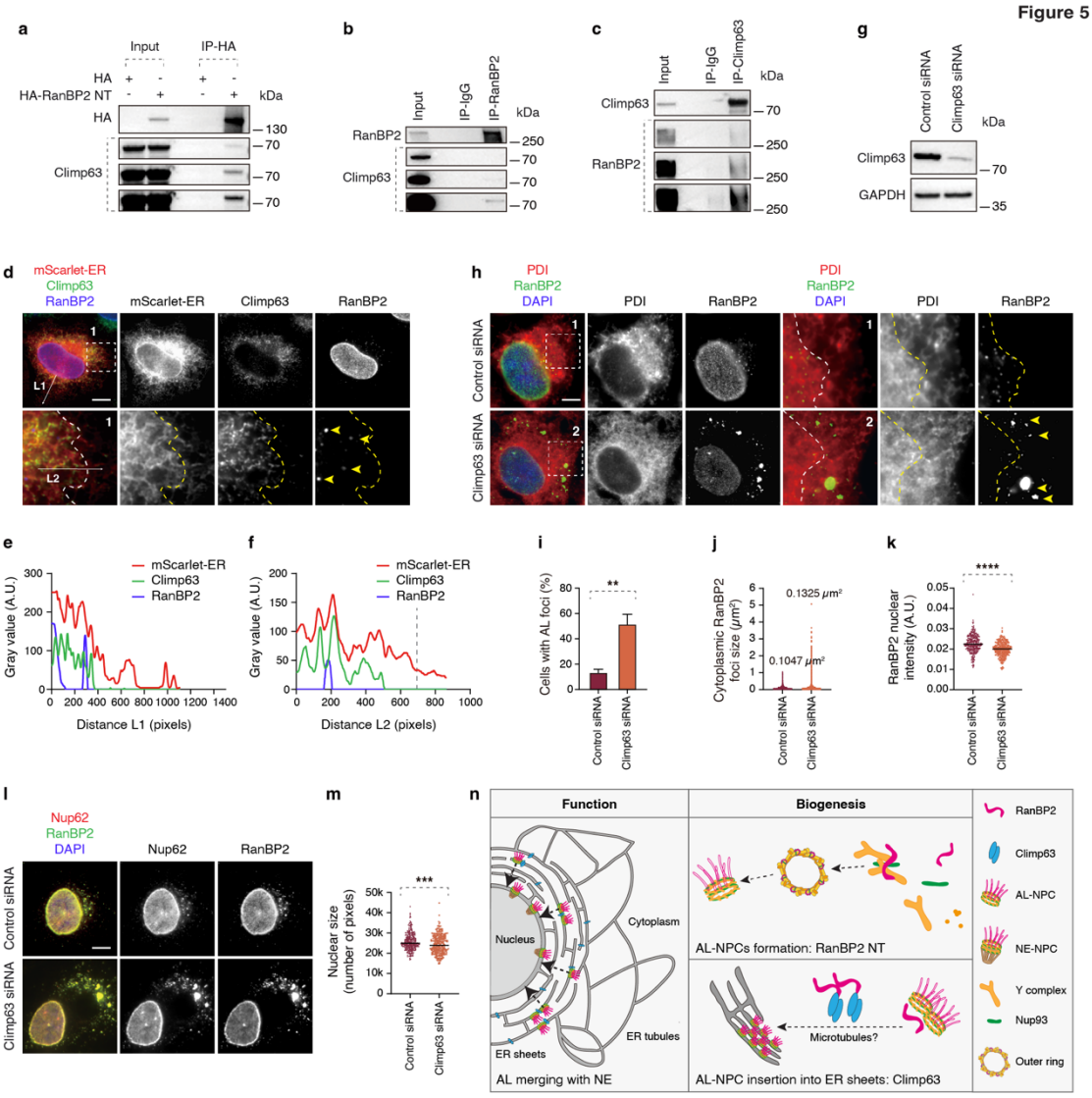

Fig. 5. Climp63 facilitates the localization of AL-NPCs to ER sheets and their integration with the NE

a, Lysates of HeLa cells expressing HA or HA-RanBP2-NT were immunoprecipitated using anti-HA magnetic beads (HA-IP) and analyzed by Western blot (at least 3 independent experiments).

b, Lysates of HeLa cells were immunoprecipitated using RanBP2 antibody or IgG and analyzed by Western blot (at least 3 independent experiments).

c, Lysates of HeLa cells were immunoprecipitated using Climp63 antibody or IgG and analyzed by western blot (at least 3 independent experiments).

d, e, f, Representative images of HeLa cells expressing ER marker plasmid mScarlet-ER. Cells were co-labelled with anti-Climp63 (green) and anti-RanBP2 (blue) antibodies (d). The magnified framed regions are shown in the corresponding numbered panels. The dotted line represents the boundary between ER sheets labeled by Climp63 and more distal ER tubules. Intensity profiles along arrows L1 and L2 showing signals from all three fluorescent channels are shown (e, f).

g-k, Representative images of HeLa cells treated with the indicated siRNAs and analyzed

by Western blot (g). Cells were co-labelled with anti-RanBP2 (green) and anti-PDI (red) antibodies (h). The magnified framed regions are shown in the corresponding numbered panels. The dotted line separates the cytoplasmic area proximal to the nuclei where AL-NPCs are enriched in WT cells. Note that AL-NPCs foci enlarge and are localized away from the nuclei upon Climp63 downregulation. The number of cells with large AL foci were quantified in (i) where at least 400 cells per condition were analyzed (mean ± SD, ns: not significant, ****P < 0.0001; N = 3). The size of cytoplasmic AL foci was quantified in (j) where at least 3500 foci per condition were analyzed (N=3). The NE intensity of RanBP2 was quantified in (k), where at least 280 cells per condition were analyzed (mean ± SD, ns: not significant, ****P < 0.0001; N = 3). Scale bars, 5 µm.

l, m, Representative images of HeLa cells treated with the indicated siRNAs. Cells were co-labelled with anti-RanBP2 (green) anti-Nup62(red) antibodies and DAPI (k). The size of nucleus was quantified in (m) where at least 300 cells per condition were analyzed (mean ± SD, ***P < 0.001, unpaired two-tailed t test; N = 3). Scale bars, 5 µm.

n, A hypothetical model on the universal function and direct biogenesis mechanisms of annulate lamellae (AL). AL are present in the cytoplasm in normally proliferating somatic cells and play a crucial role in supplying the NE with new nuclear pores. This function is important for nucleocytoplasmic transport and for nuclear growth during early interphase. The N-terminal part of RanBP2 is required and sufficient for the formation of AL-NPCs in the cytosol across cellular models and conditions. It ensures oligomerization of NPC scaffold components (Y-complexes) specifically in the cytoplasm. Climp63 ensures the insertion of pre-made AL-NPCs into ER sheets which are more proximal to the NE. This process is important for AL merging with the NE and for nuclear growth.

Additional information

The supplementary materials consist of Supplementary Table 1, Supplementary Video 1-3 and Extended Data Figures 1-20.

Supplementary Table 1. List of reagents used for cloning, siRNA, and CRISPR/Cas9 methods

Table summarizes cloning primers, siRNAs and guide RNAs used in this study.

Supplementary Video 1. AL foci fuse together following MT depolymerization

2xZFN-mEGFP-Nup107 HeLa cells treated with nocodazole were analyzed by live video spinning disk confocal microscopy. Z-stacks (10 μm range, 0.5 μm step) were acquired every 10 minutes and maximum intensity projection images are shown at speed 5 frames per second. A representative cell is depicted and selected representative frames of the movie are shown in the Fig. 1e.

Supplementary Video 2. AL foci display tendency to merge with the NE

2xZFN-mEGFP-Nup107 HeLa cells were synchronized by double thymidine block, released and analyzed by live video spinning disc confocal microscopy. Timepoint 0 indicates the mitotic exit and entry into a new cell cycle. Z-stacks (10 μm range, 0.5 μm step) were acquired every 5 minutes and maximum intensity projection images are shown at speed 5 frames per second. A representative cell is depicted and selected representative frames of the movie are shown in the Fig. 2c.

Supplementary Video 3. AL foci move along ER to merge with the NE

2xZFN-mEGFP-Nup107 HeLa cells expressing ER marker plasmid mScarlet-ER were analyzed by live video spinning disk confocal microscopy. Timepoint 0 indicates the start of the imaging. Frames were acquired every 20s (without Z-stacks) and images are shown at speed 5 frames per second. A representative cell is depicted in the Fig. 2d and a zoomed region of selected representative frames of the video is shown.

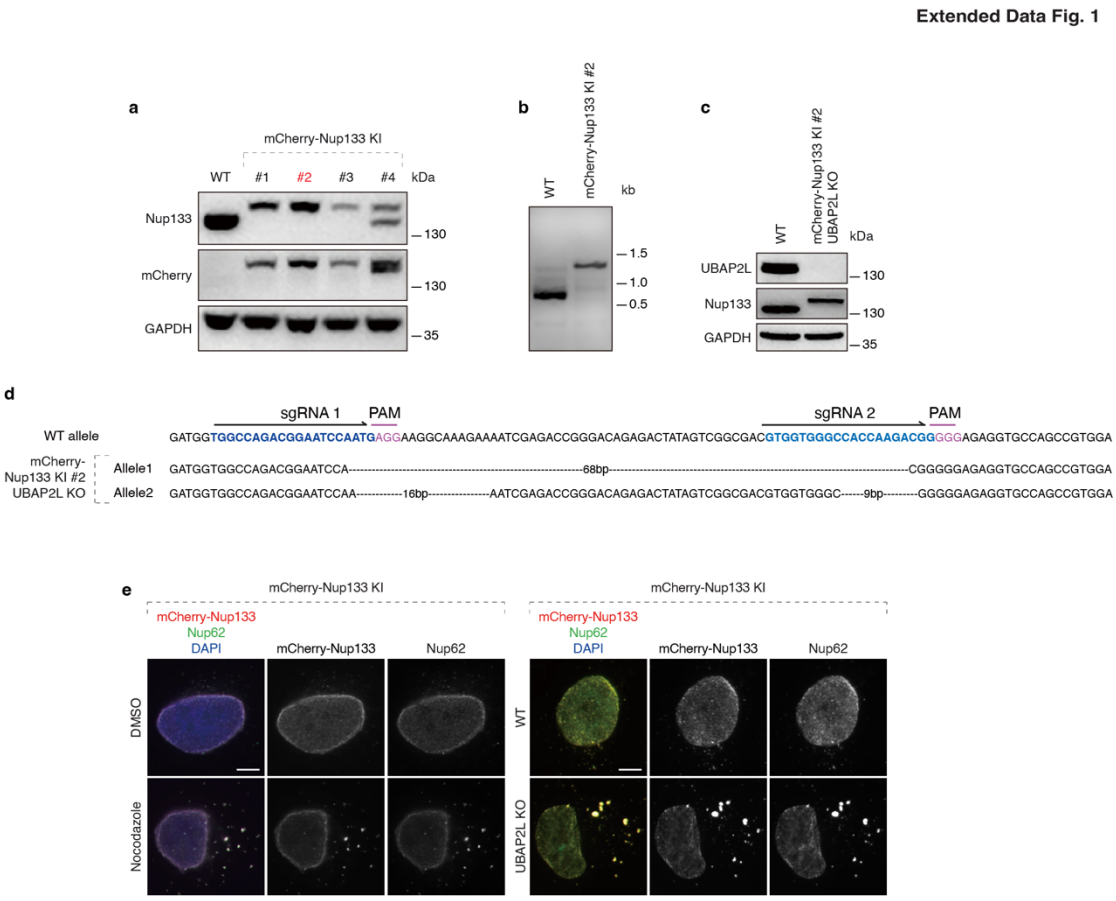

Extended Data Fig. 1. Validation of mCherry-Nup133 knock-in (KI) HeLa and UBAP2L KO mCherry-Nup133 KI HeLa cell lines

a, b, Validation of CRISPR/Cas9-mediated mCherry-Nup133 KI Hela cell clones by Western blot (a) and PCR (b).

c, d, Validation of CRISPR/Cas9-mediated UBAP2L KO mCherry-Nup133 KI HeLa cell clones by Western blot (c) and Sanger sequencing (d).

e, Representative images of mCherry-Nup133 KI HeLa cells treated with DMSO or Nocodazole (10 μM) and representative images of UBAP2L KO mCherry-Nup133 KI HeLa. Cells were co-labelled with DAPI (blue), and anti-Nup62 (green) antibody. Scale bars, 5 μm.

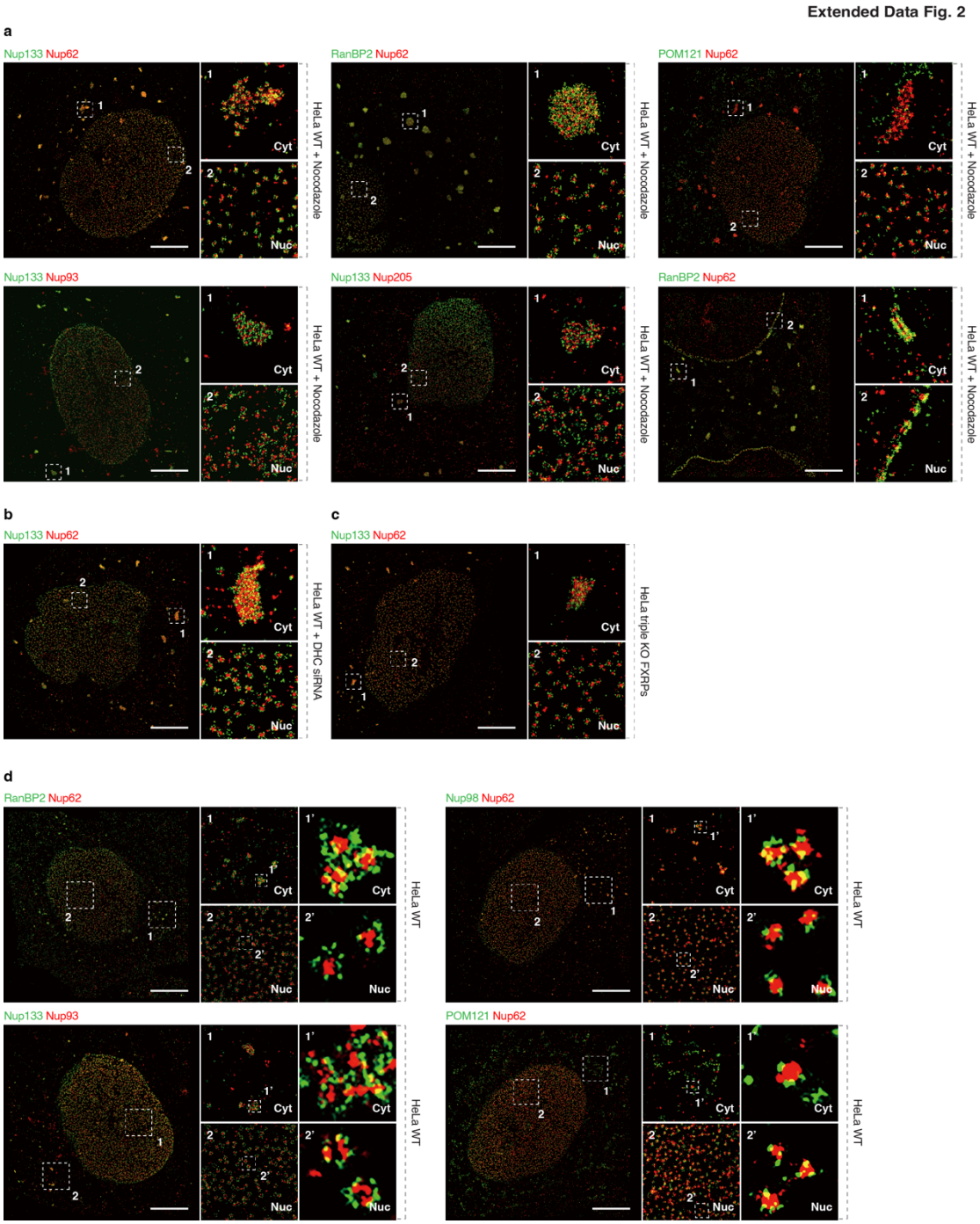

Extended Data Fig. 2. Single molecule localization microscopy identifies the presence of AL in WT and in challenged HeLa cells

a, Representative splitSMLM images depicting NPCs on the nuclear (Nuc) surface and NPCs in the cytoplasm (Cyt) in nocodazole-treated (10 µM, 90 min) HeLa cells. Analyzed Nups from different NPC subcomplexes are indicated above each panel. The magnified framed regions are shown in the corresponding numbered panels. Scale bars, 5 µm.

b, c, Representative splitSMLM images depicting NPCs on the nuclear (Nuc) surface and NPCs in the cytoplasm (Cyt) in HeLa cell treated with the dynein heavy chain siRNAs (48h)

1286 and triple knock-out of FXRPs HeLa cells. Nup133 signal labels the cytoplasmic and
1287 nuclear rings of the NPC and the localization of the central channel is visualized by Nup62.
1288 The magnified framed regions are shown in the corresponding numbered panels. Scale
1289 bars, 5 µm.
1290 d, Representative splitSMLM images depicting NPCs on the nuclear (Nuc) surface and
1291 NPCs in the cytoplasm (Cyt) in WT HeLa cells. Analyzed Nups from different NPC
1292 subcomplexes are indicated above each panel. The magnified framed regions are shown
1293 in the corresponding numbered panels. Scale bars, 5 µm.
1294

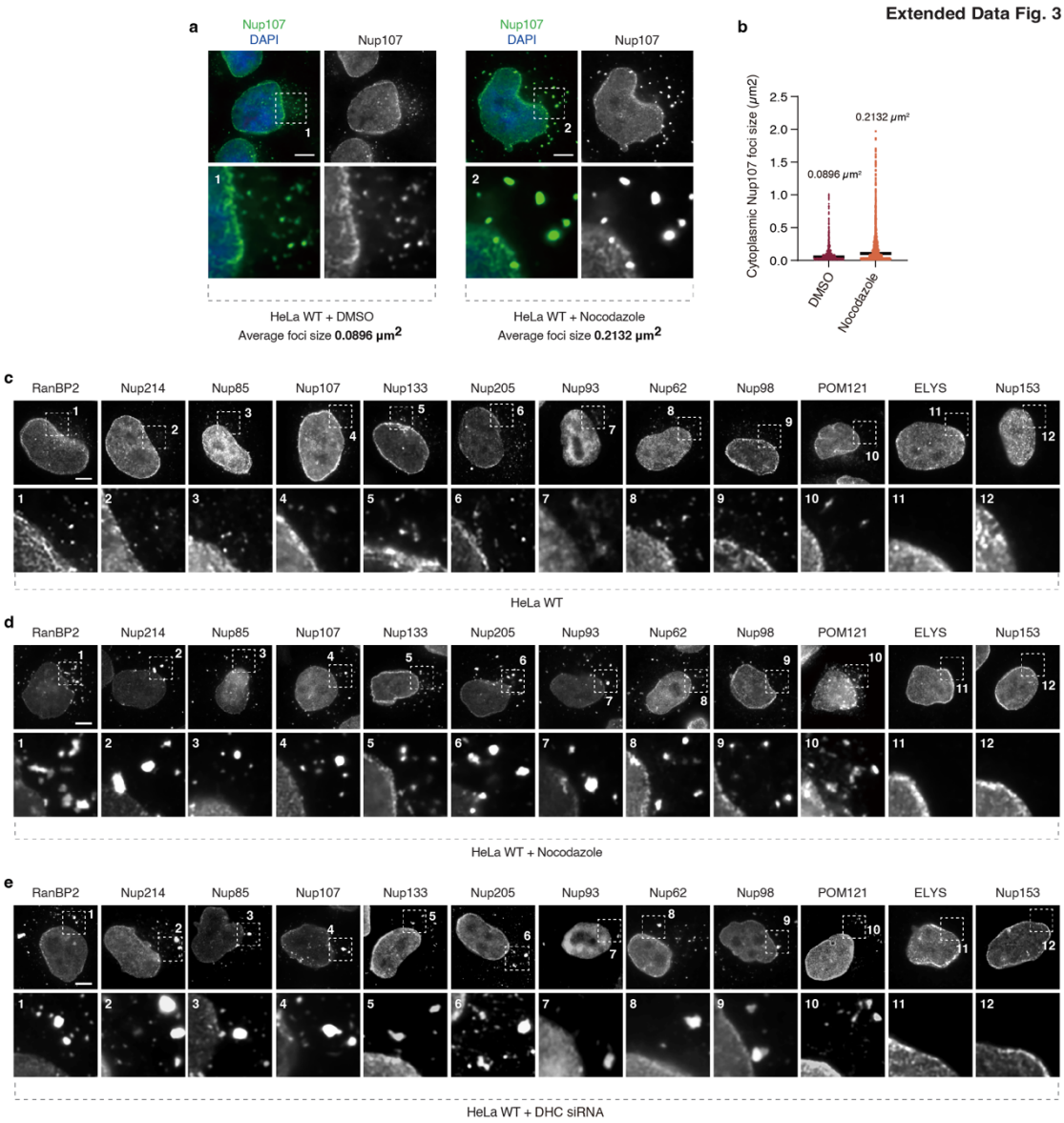

f

		NE-NPCs	AL-NPCs WT	AL-NPCs Nocodazole	AL-NPCs DHC siRNA	AL-NPCs FXR1 siRNA*	AL-NPCs UBAP2L KO*
Cytoplasmic filaments	RanBP2	Y	Y	Y	Y	Y	Y
	Nup214	Y	Y	Y	Y	Y	-
Outer rings	Nup85	Y	Y	Y	Y	Y	Y
	Nup107	Y	Y	Y	Y	Y	Y
	Nup133	Y	Y	Y	Y	Y	Y
	ELYS	**Y**	**N**	**N**	**N**	**N**	**N**
Inner rings	Nup205	Y	Y	Y	Y	-	Y
	Nup93	Y	Y	Y	Y	-	Y
Central channel	Nup62	Y	Y	Y	Y	Y	Y
Linker Nups	Nup98	Y	Y	Y	Y	Y	Y
Transmembrane Nups	POM121	Y	Y	Y	Y	Y	Y
Nuclear basket	Nup153	**Y**	**N**	**N**	**N**	**N**	**N**

Extended Data Fig. 3. Systematic analysis of the size and the composition of AL foci. a, b, Representative images of 2xZFN-mEGFP-Nup107 HeLa cells treated with nocodazole (10 µM) or DMSO (90 min) (a). Cells were co-labelled with DAPI (blue). The magnified framed regions are shown in the corresponding numbered panels. The size of Nup107-positive AL foci in the cytoplasm were quantified in (b), and at least 2000 foci per condition were analyzed (N=3). Scale bars, 5 µm.

1304 c, Representative images of WT HeLa cells labelled with Nups from different NPC
1305 subcomplexes. Analyzed Nups are indicated above each panel. The magnified framed
1306 regions are shown in the corresponding numbered panels. Scale bars, 5 μm.
1307 d, Representative images of nocodazole-treated (10 μM, 90 min) HeLa cells labelled with
1308 Nups from different NPC subcomplexes. Analyzed Nups are indicated above each panel.
1309 The magnified framed regions are shown in the corresponding numbered panels. Scale
1310 bars, 5 μm.
1311 e, Representative images of dynein heavy chain siRNAs-treated (48h) HeLa cells labelled
1312 with Nups from different NPC subcomplexes. Analyzed Nups are indicated above each
1313 panel. The magnified framed regions are shown in the corresponding numbered panels.
1314 Scale bars, 5 μm.
1315 f, Summary of composition of NE-NPCs and AL-NPCs under different conditions. Different
1316 colors represent specific NPC subcomplexes. “Y” indicates presence and “N” indicates
1317 absence of indicated Nups. “-” represents no available data. “*” indicates published
1318 results[35,47,48].
1319
1320

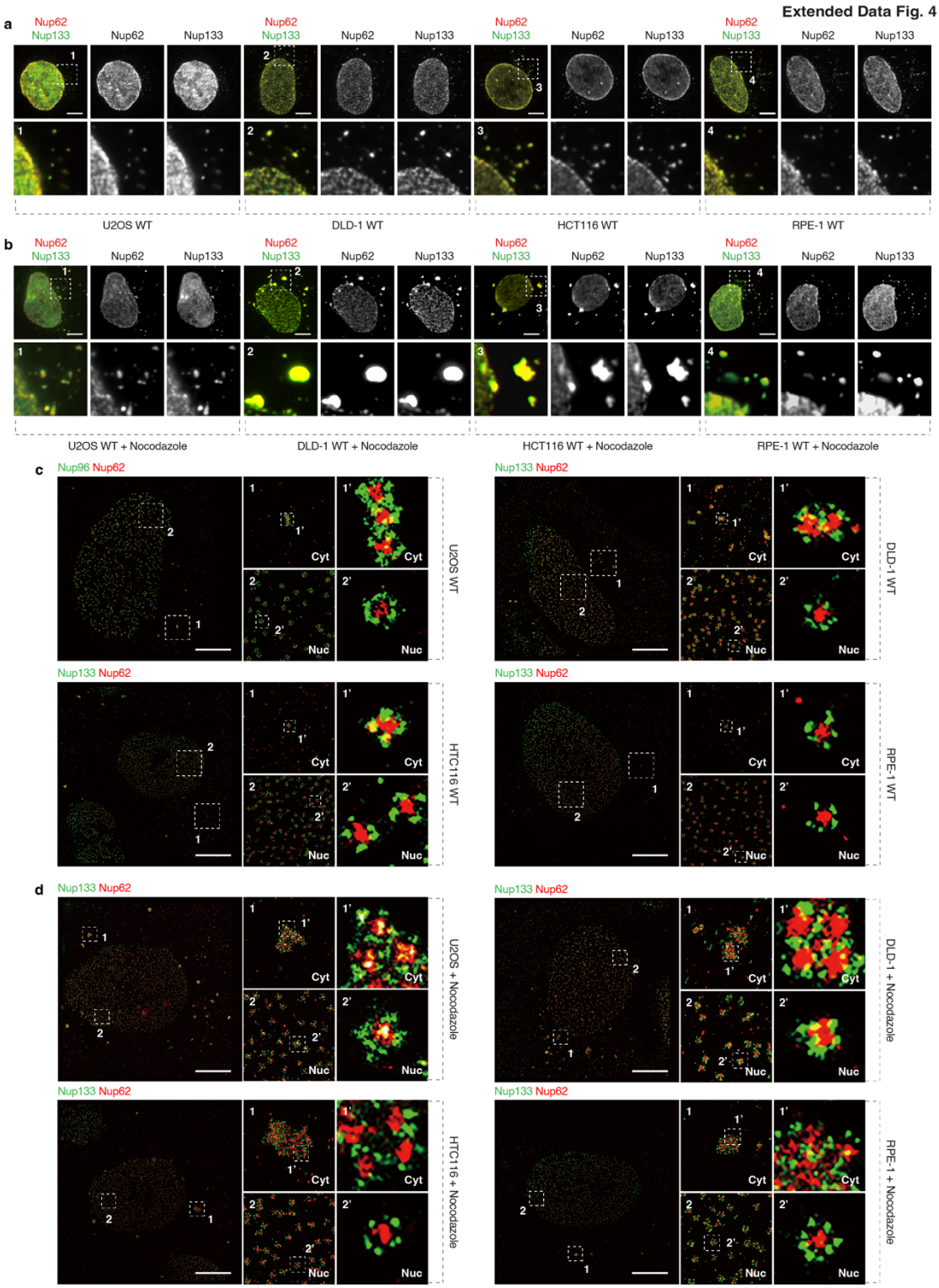

Extended Data Fig. 4. AL exist in a variety of mammalian cells.

a, Representative images of WT U2OS, DLD-1, HTC116 and RPE-1 cells showing AL foci. Cells were co-labelled with anti-Nup62 (red) and anti-Nup133 (green) antibodies to visualize AL-NPCs. Scale bars, 5 μm.

b, Representative images of U2OS, DLD-1, HTC116, RPE-1 cells treated with nocodazole (10 μM, 90 min). Cells were co-labelled with anti-Nup62 (red) and anti-Nup133 (green)

1329 antibodies to visualize AL-NPCs. Scale bars, 5 µm.
1330 c, Representative splitSMLM images depicting NPCs on the nuclear (Nuc) surface and
1331 NPCs in the cytoplasm (Cyt) in WT U2OS, DLD-1, HTC116 and RPE-1 cells. Analyzed
1332 Nups from different NPC subcomplexes are indicated above each panel. The magnified
1333 framed regions are shown in the corresponding numbered panels. Scale bars, 5 µm.
1334 d, Representative splitSMLM images depicting NPCs on the nuclear (Nuc) surface and
1335 NPCs in the cytoplasm (Cyt) in nocodazole-treated (10 µM, 90 min) U2OS, DLD-1, HTC116
1336 and RPE-1 cells. Analyzed Nups from different NPC subcomplexes are indicated above
1337 each panel. The magnified framed regions are shown in the corresponding numbered
1338 panels. Scale bars, 5 µm.
1339

1340

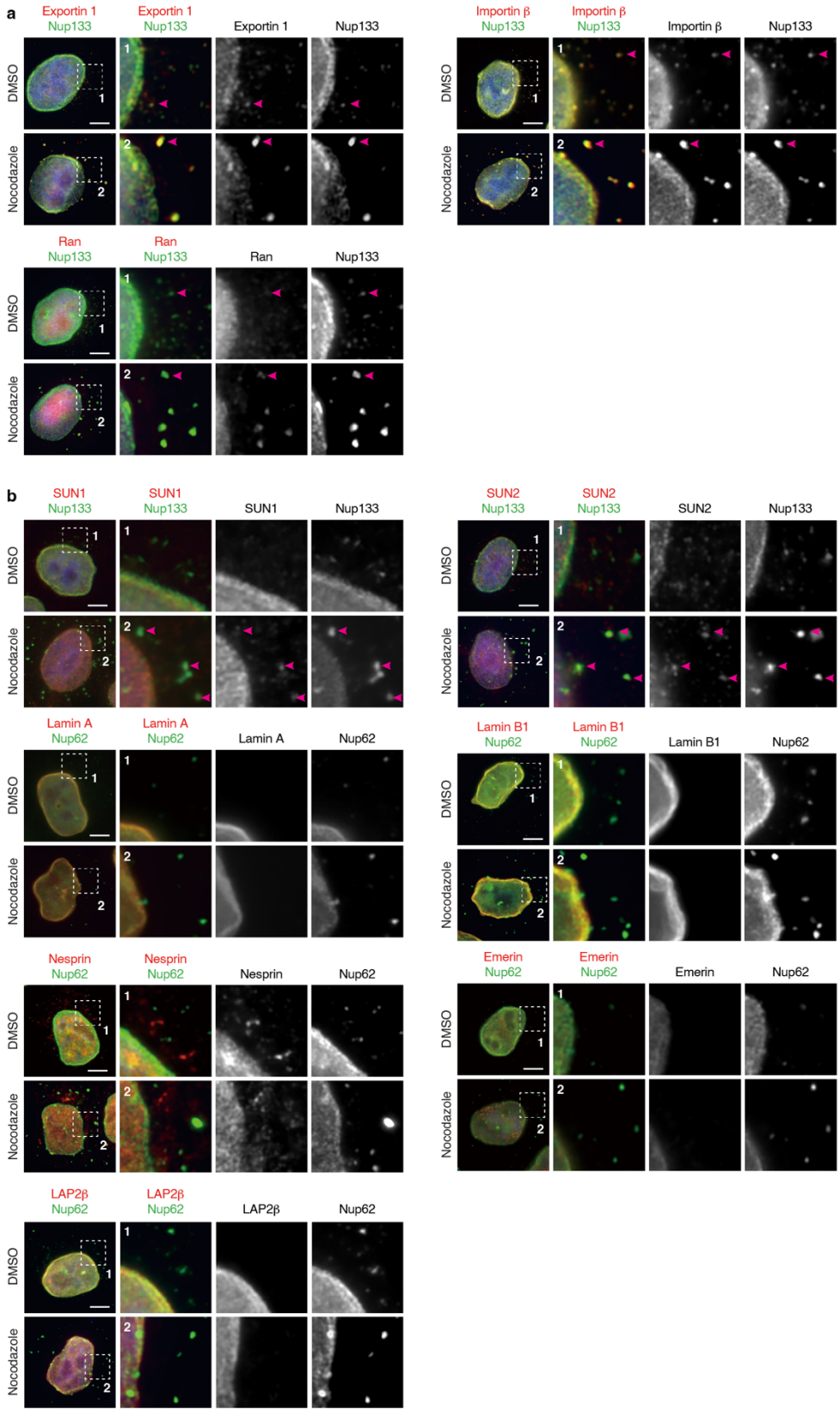

1341
1342

1343 **Extended Data Fig. 5. Systematic analysis of composition of AL-NPC**

1344 a, Representative images showing co-localization of nucleocytoplasmic transport factors

1345 (NTF) with AL-NPC in HeLa cells treated with nocodazole (10 μM) or DMSO (90 min). Cells
1346 were co-labelled with anti-NTF (Exportin-1, Importin β, and Ran) (red) and anti-Nup133
1347 (green) antibodies. The magnified framed regions are shown in the corresponding
1348 numbered panels. Magenta arrows point to co-localized foci. Scale bars, 5 μm.
1349 b, Representative images showing co-localization of NE-related proteins with AL-NPC in
1350 HeLa cells treated with nocodazole (10 μM) or DMSO (90 min). Cells were co-labelled with
1351 anti-NE-related proteins (SUN1, SUN2, Lamin A, Lamin B1, Nesprin, Emerin, and Lap2)
1352 (red) and anti-Nup62 (green) antibodies. The magnified framed regions are shown in the
1353 corresponding numbered panels. Magenta arrows point to co-localized foci. Scale bars, 5
1354 μm.
1355

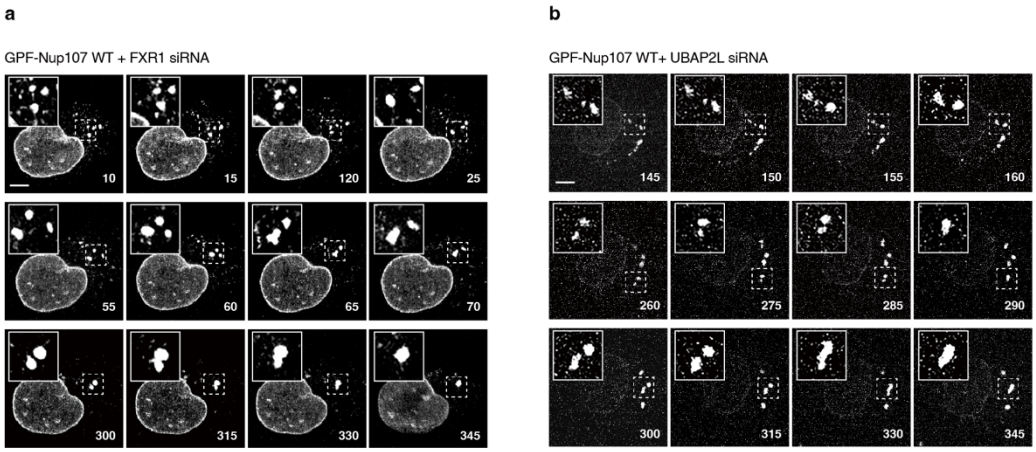

Extended Data Fig. 6. Large AL are formed by fusion of small AL structures.
a, 2xZFN-mEGFP-Nup107 HeLa cells treated with FXR1 siRNA were analyzed by live video spinning disk confocal microscopy. The selected representative frames of the movies are depicted, and time is shown in minutes. The timepoint 0 of the movie corresponds to a 12h release time from double thymidine block. The magnified framed regions are shown in the upper left corner. Scale bars, 5 μm.
b, 2xZFN-mEGFP-Nup107 HeLa cells treated UBAP2L siRNA were analyzed by live video spinning disk confocal microscopy. The selected representative frames of the movies are depicted, and time is shown in minutes. The timepoint 0 of the movie corresponds to a 12h release time from double thymidine block. The magnified framed regions are shown in the upper left corner. Scale bars, 5 μm.

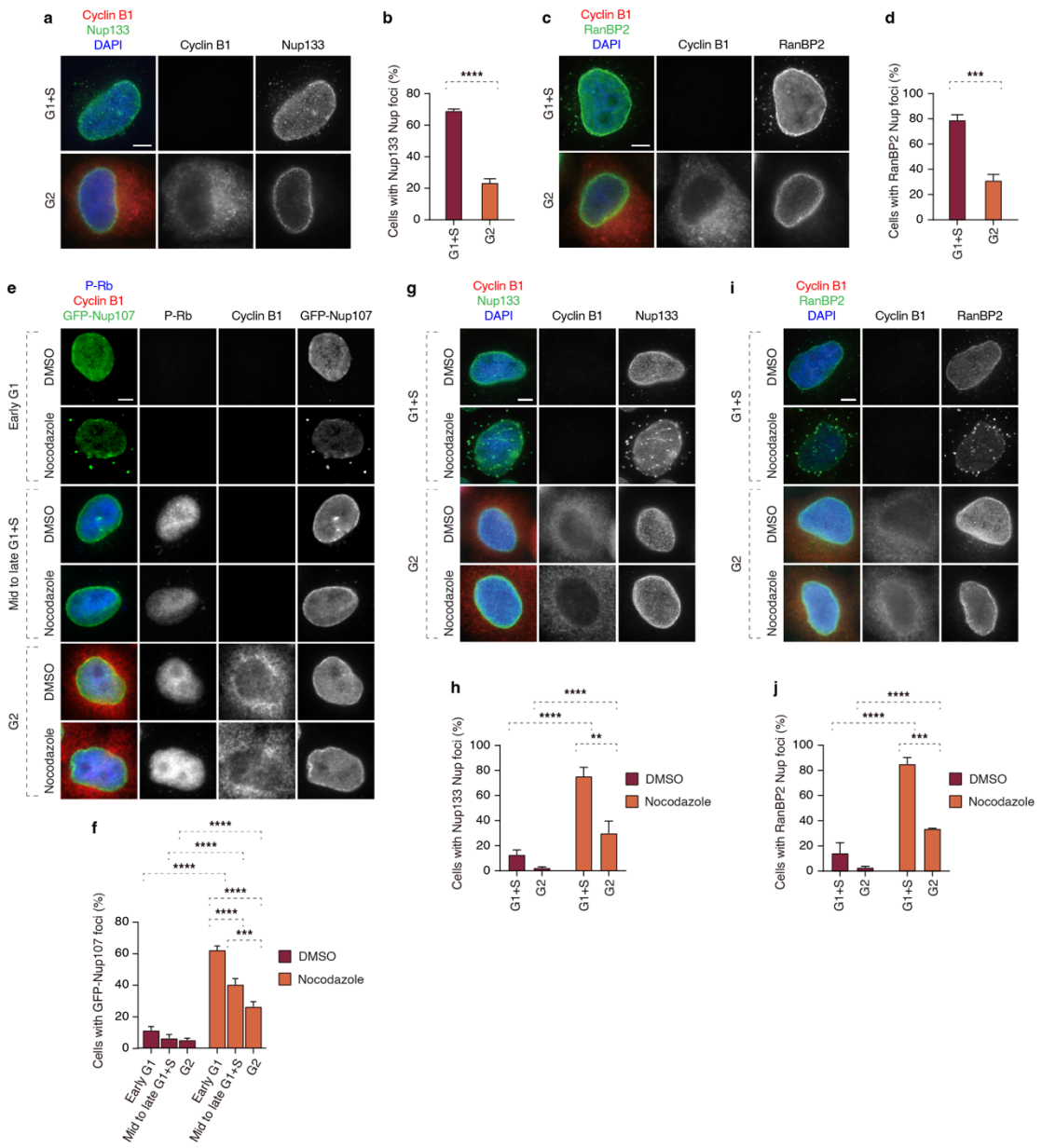

Extended Data Fig. 7. AL foci are present throughout interphase, but predominantly in the G1 and S phases.

a, b, Representative images of asynchronously proliferating HeLa cells co-labelled with anti-Nup133 (green) and anti-cyclin B1 (red) (a) antibodies. The percentage of cells with AL foci in cyclin B1 negative cells (G1+S), and cyclin B1 positive cells (G2) was quantified in (b), and at least 200 cells per condition were analyzed (mean ± SD, ****P < 0.0001; N = 3). Scale bars, 5 µm.

c, d, Representative images of asynchronously proliferating HeLa cells co-labelled with anti-RanBP2 (green) and anti-cyclin B1 (red) (c) antibodies. The percentage of cells with AL foci in cyclin B1 negative cells (G1+S), and cyclin B1 positive cells (G2) was quantified in (d), and at least 200 cells per condition were analyzed (mean ± SD, ***P < 0.001; N =

3). Scale bars, 5 μm.

e, f, Representative images of asynchronously proliferating 2xZFN-mEGFP-Nup107 HeLa cells treated with nocodazole (10 μM) or DMSO (90 min) and co-labelled with anti-p-Rb (blue) and anti-cyclin B1 (red) (e) antibodies. The percentage of cells with large AL foci in p-Rb and cyclin B1 negative cells (early G1), p-Rb positive and cyclin B1 negative cells (mid to late G1+S), and p-Rb and cyclin B1 positive cells (G2) was quantified in (f), and at least 200 cells per condition were analyzed (mean ± SD, ***P < 0.001; ****P < 0.0001; N = 3). Scale bars, 5 μm.

g, h, Representative images of asynchronously proliferating HeLa cells treated with nocodazole (10 μM) or DMSO (90 min) and co-labelled with anti-Nup133 (green) and anti-cyclin B1 (red) (g) antibodies. The percentage of cells with large AL foci in cyclin B1 negative cells (G1+S), and cyclin B1 positive cells (G2) was quantified in (h), and at least 200 cells per condition were analyzed (mean ± SD, **P < 0.01; ****P < 0.0001; N = 3). Scale bars, 5 μm.

i, j, Representative images of asynchronously proliferating HeLa cells treated with nocodazole (10 μM) or DMSO (90 min) and co-labelled with anti-RanBP2 (green) and anti-cyclin B1 (red) (i) antibodies. The percentage of cells with large AL foci in cyclin B1 negative cells (G1+S), and cyclin B1 positive cells (G2) was quantified in (j), and at least 200 cells per condition were analyzed (mean ± SD, ***P < 0.001; ****P < 0.0001; N = 3). Scale bars, 5 μm.

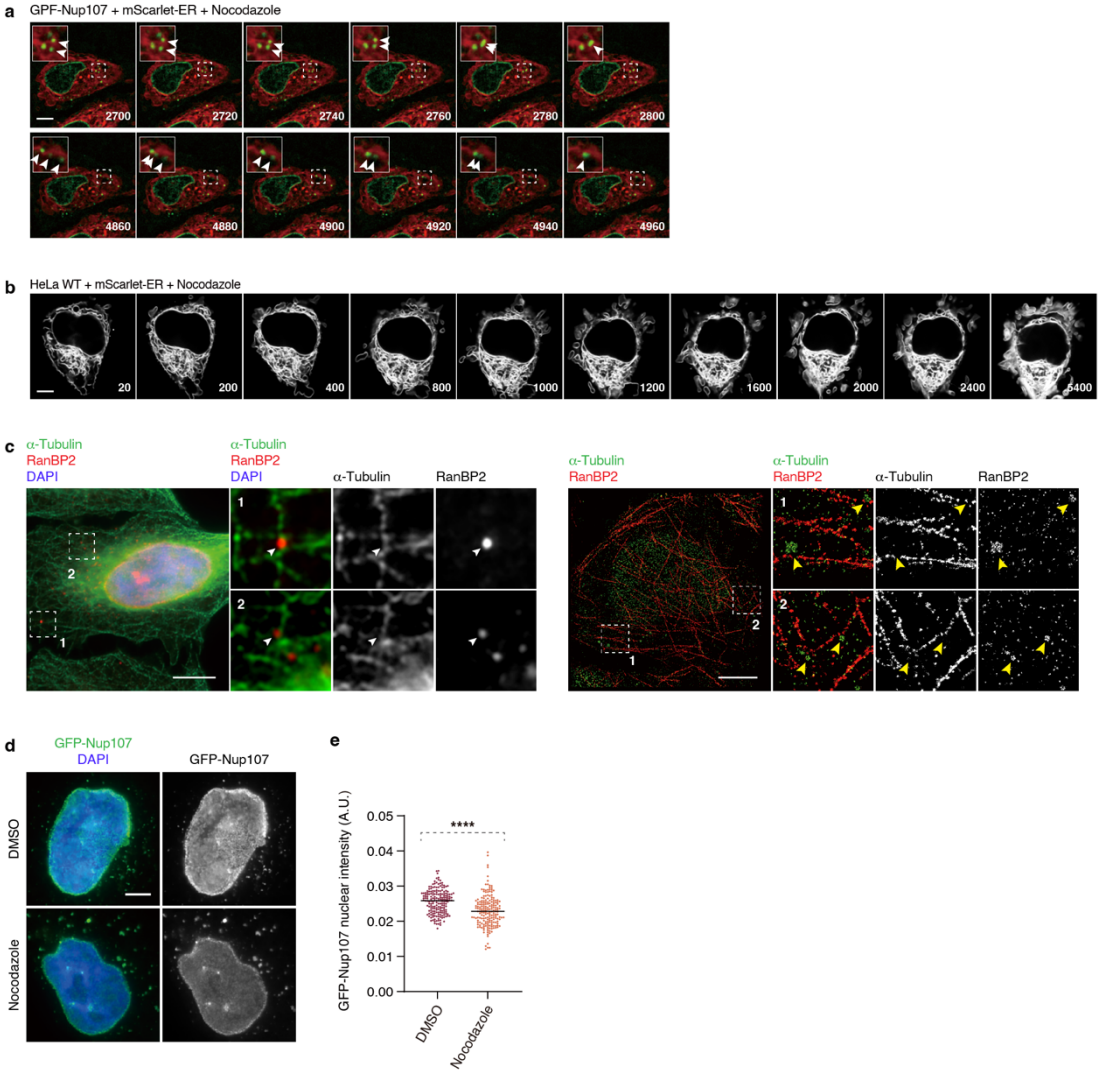

Extended Data Fig. 8. Disruption of ER dynamics inhibits AL integration into NE.
a, 2xZFN-mEGFP-Nup107 HeLa cells expressing ER marker plasmid mScarlet-ER were treated with nocodazole (10 μM) and were analyzed by live video spinning disk confocal microscopy. The selected representative frames of the movies are depicted, and time is shown in second. The timepoint 0 corresponds to nocodazole addition. The magnified framed regions are shown in the upper left corner. Arrowheads point to the AL that fuse together. Scale bars, 5 μm.
b, HeLa cells expressing ER marker plasmid mScarlet-ER were treated with nocodazole (10 μM) and were analyzed by live video spinning disk confocal microscopy. The selected representative frames of the movies are depicted, and time is shown in second. The timepoint 0 corresponds to nocodazole addition. The magnified framed regions are shown in the upper left corner. Scale bars, 5 μm.
c, Representative immunofluorescence (IF) images and splitSMLM images depicting co-localization of AL-NPCs and microtubules in the cytoplasm in WT HeLa cells. For the IF on the left, cells were co-labelled with anti-alpha tubulin (green), anti-RanBP2 (red) antibodies and DAPI. For the splitSMLM on the right, cells were co-labelled with anti-alpha tubulin (red), and anti-RanBP2 (green) antibodies. The magnified framed regions are shown in the

1423 corresponding numbered panels. Arrowheads point to AL-NPC near microtubules. Scale
1424 bars, 5 μm.
1425 d, e, Representative images of 2xZFN-mEGFP-Nup107 HeLa cells treated with
1426 Nocodazole (10 μM) or DMSO (90 min) (d). Cells were co-labelled with DAPI (blue). The
1427 intensity of EGFP-Nup107 in the NE was quantified in (e), and at least 200 cell per
1428 condition were analyzed (mean ± SD, ****$P < 0.0001$; $N = 3$). Scale bars, 5 μm.
1429

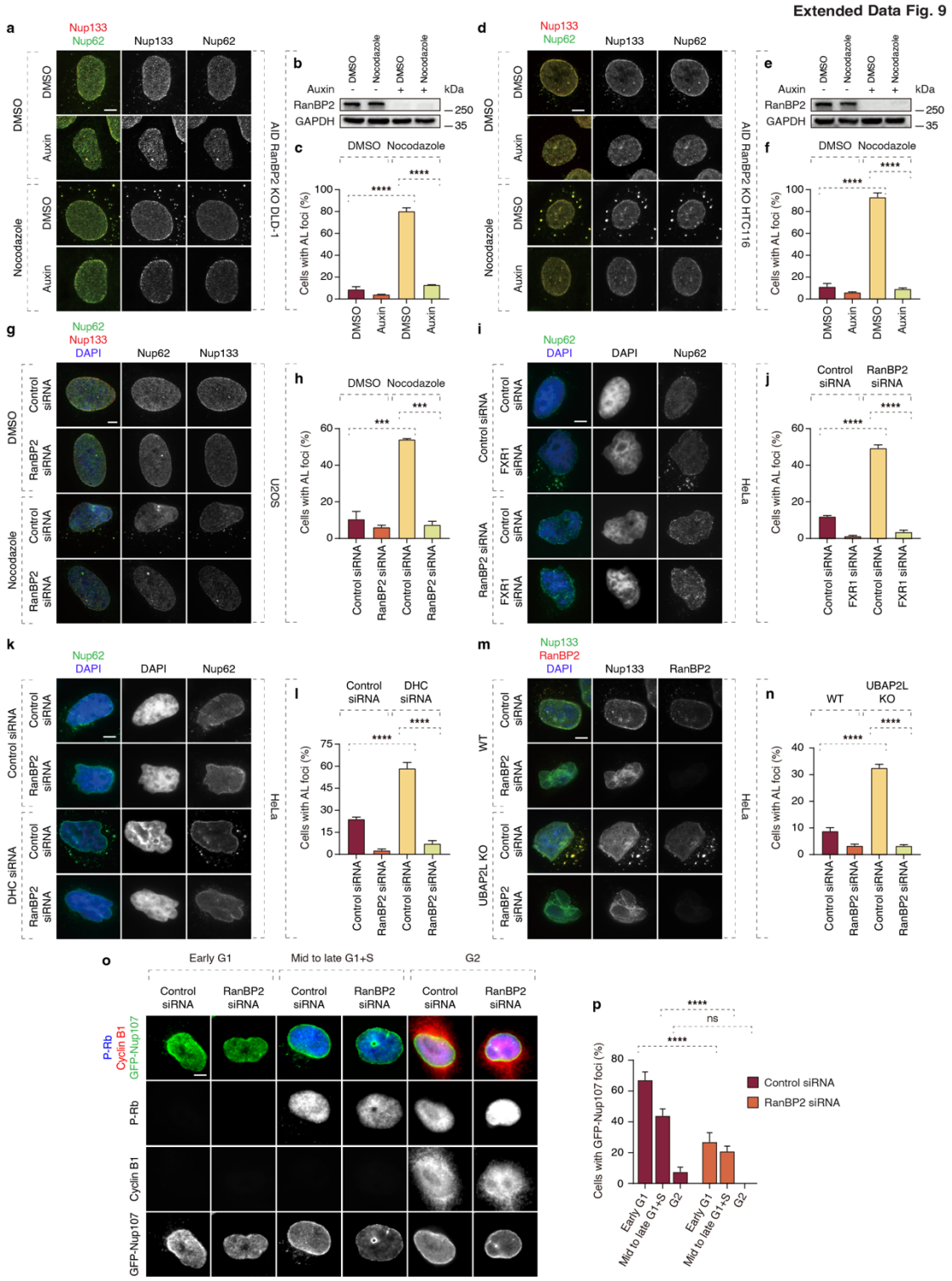

Extended Data Fig. 9. RanBP2 is required for the formation AL in somatic cells. a, b, c, Representative images of auxin-inducible degron (AID)-RanBP2 KO DLD-1 cells treated with the auxin or DMSO (4h) and subsequently with nocodazole (10 μM) or DMSO (90 min). Cells were co-labelled with anti-Nup62 (red) and anti-Nup133 (green) (a) antibodies. (b) Shows the WB analysis of RanBP2 under different conditions shown in (a).

The number of cells with large AL foci were quantified in (c), and at least 1000 cells per condition were analyzed (mean ± SD, ****P < 0.0001; N = 3). Scale bars, 5 μm.

d, e, f, Representative images of AID-RanBP2 KO HTC116 cells treated with auxin or DMSO (4h) and subsequently with nocodazole (10 μM) or DMSO (90 min). Cells were co-labelled with anti-Nup62 (red) and anti-Nup133 (green) (d) antibodies. (e) Shows the WB analysis of RanBP2 under different conditions shown in (d). The number of cells with large AL foci were quantified in (f), and at least 1000 cells per condition were analyzed (mean ± SD, ****P < 0.0001; N = 3). Scale bars, 5 μm.

g, h, Representative images of U2OS cells treated with the indicated siRNAs (48h) and and subsequently with nocodazole (10 μM) or DMSO (90 min). Cells were co-labelled with anti-Nup62 (green) and anti-Nup133 (red) (g) antibodies. The number of cells with large AL foci were quantified in (h), and at least 1000 cells per condition were analysed (mean ± SD, ***P < 0.001; N = 3). Scale bars, 5 μm.

i, j, Representative images of HeLa cells treated with the indicated siRNAs (48h). Cells were co-labelled with anti-Nup62 (green) antibodies and DAPI (blue) (i). The number of cells with large AL foci were quantified in (j), and at least 1000 cells per condition were analyzed (mean ± SD, ****P < 0.0001; N = 3). Scale bars, 5 μm.

k, l, Representative images of HeLa cells treated with the indicated siRNAs (48h). Cells were co-labelled with anti-Nup62 (green) antibodies and DAPI (blue) (k). The number of cells with large AL foci were quantified in (l), and at least 1000 cells per condition were analyzed (mean ± SD, ****P < 0.0001; N = 3). Scale bars, 5 μm.

m, n, Representative images of UBAP2L KO and WT HeLa cells treated with the indicated siRNAs (48h). Cells were co-labelled with anti-Nup133 (green) and anti-RanBP2 (red) (m) antibodies. The number of cells with large AL foci were quantified in (n), and at least 1000 cells per condition were analyzed (mean ± SD, ****P < 0.0001; N = 3). Scale bars, 5 μm.

o, p, Representative images of asynchronously proliferating 2xZFN-mEGFP-Nup107 HeLa cells treated with the indicated siRNAs (48h) and co-labelled with anti-p-Rb (blue) and anti-cyclin B1 (red) (o) antibodies. The percentage of cells with AL foci in p-Rb and cyclin B1 negative cells (early G1) , p-Rb positive and cyclin B1 negative cells (mid to late G1+S), and p-Rb and cyclin B1 positive cells (G2) was quantified in (p), and at least 200 cells per condition were analyzed (mean ± SD, ****P < 0.0001; N = 3). Scale bars, 5 μm.

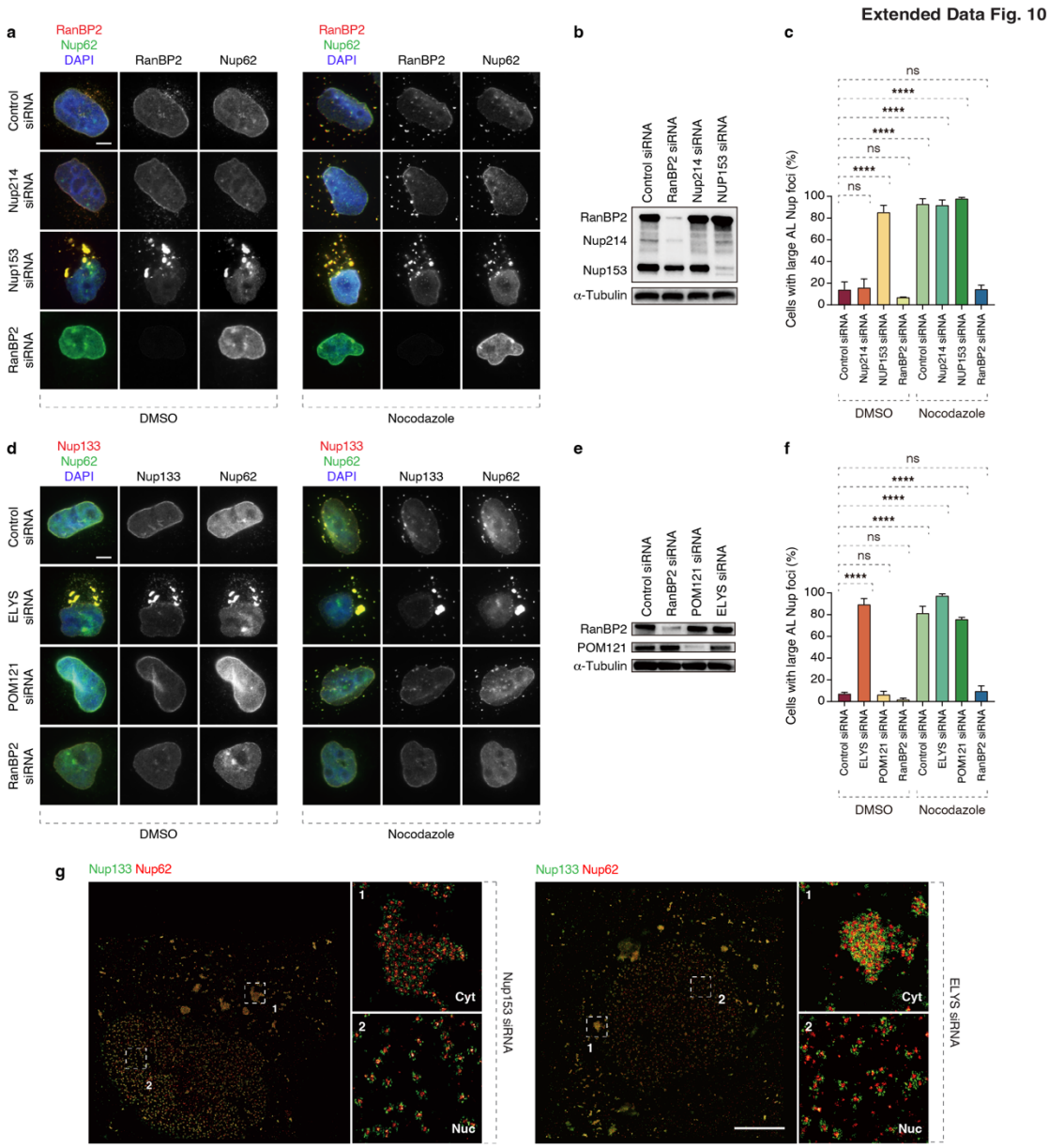

Extended Data Fig. 10. RanBP2 but not Nup153, Nup214, POM121 and ELYS is required for the formation of AL in somatic cells.

a, b, c Representative images of HeLa cells treated with the indicated siRNAs (48h) and subsequently with nocodazole (10 μM) or DMSO (90 min). Cells were co-labelled with anti-Nup62 (green) and anti-RanBP2 (red) (a) antibodies. (b) Shows the WB analysis of RanBP2, Nup214 and Nup153 under different conditions shown in (a). The number of cells with large AL foci were quantified in (c), and at least 1000 cells per condition were analysed (mean ± SD, ns: not significant, ****P < 0.0001; N = 3). Scale bars, 5 μm.

d, e, f Representative images of HeLa cells treated with the indicated siRNAs (48h) and subsequently with nocodazole (10 μM) or DMSO (90 min). Cells were co-labelled with anti-Nup62 (green) and anti-Nup133 (red) (d) antibodies. (e) Shows the WB analysis of RanBP2, and POM121 under different conditions shown in (d). The number of cells with large AL foci were quantified in (f), and at least 1000 cells per condition were analysed

1485 (mean ± SD, ns: not significant, ****P < 0.0001; N = 3). Scale bars, 5 µm.
1486 g, Representative splitSMLM images depicting NPCs on the nuclear (Nuc) surface and
1487 NPCs in the cytoplasm (Cyt) in Nup153 siRNA or ELYS siRNA-treated (48h) HeLa cells.
1488 Nup133 signal labels the cytoplasmic and nuclear rings of the NPC, the localization of the
1489 central channel is visualized by Nup62. The magnified framed regions are shown in the
1490 corresponding numbered panels. Scale bars, 5 µm.
1491

1492

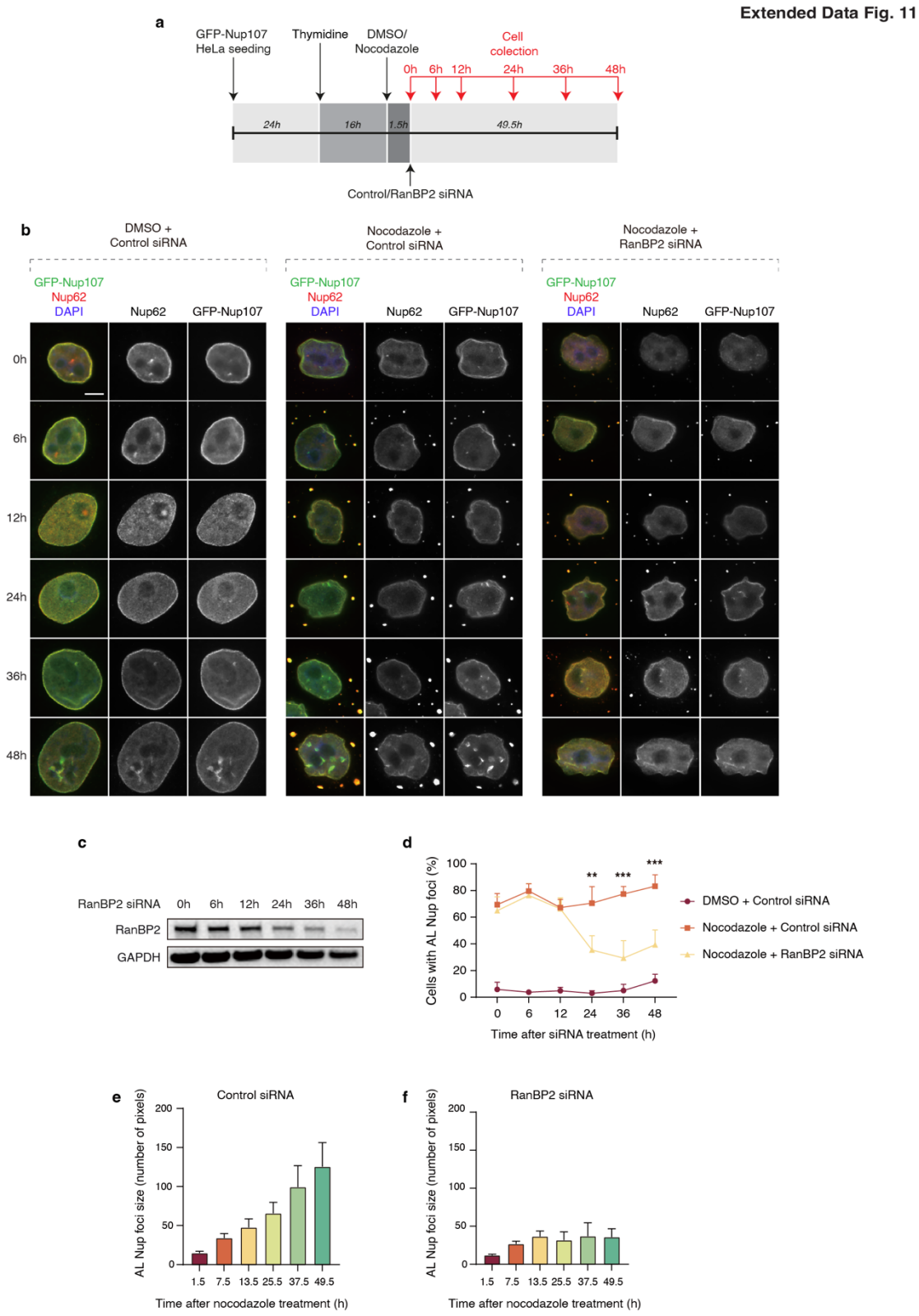

1493

1494

1495 **Extended Data Fig. 11. RanBP2 is required for the maintenance of AL in HeLa cells.**
1496 a-f, Scheme of the experimental setup (a). HeLa cells were synchronized and arrested in
1497 S phase by thymidine treatment (16h), treated with nocodazole (10 μM) and subsequently

1498 with the indicated siRNAs, and fixed at indicated timeopoints. Representative images of
1499 cells are shown in (b). (c) Shows the WB analysis of RanBP2 at indicated timepoints. The
1500 number of cells with large AL foci were quantified in (d) and the size of AL foci was
1501 quantified in (e, f). At least 200 cells and 1500 foci per condition were analyzed (mean ±
1502 SD, ****P < 0.0001; N = 3). Scale bars, 5 μm.

1503

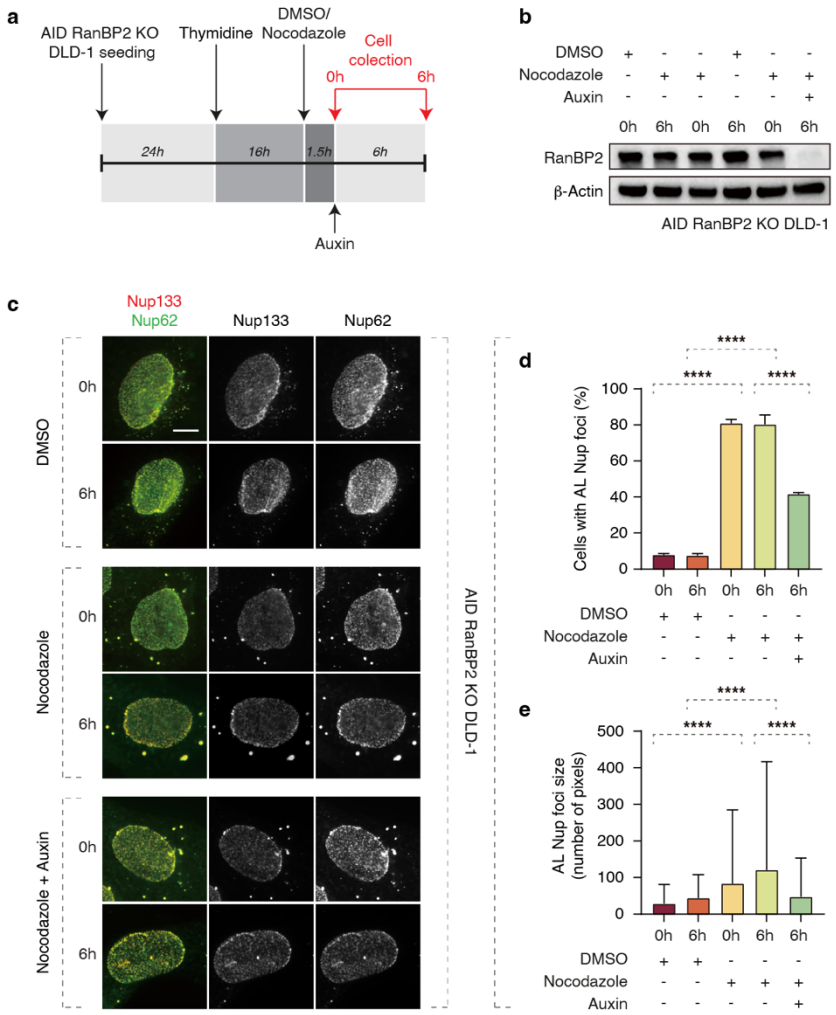

Extended Data Fig. 12. RanBP2 is required for the maintenance of AL in DLD-1 cells. a-e, Scheme of the experimental setup (a). AID-RanBP2 KO DLD-1 cells were synchronized and arrested at S phase by thymidine treatment (16h), treated with nocodazole (10 μM) and with auxin. Representative images of cells are shown in (c). (b) Shows the WB analysis of RanBP2 under different conditions shown in (c). The number of cells with large AL foci were quantified in (d) and the size of AL foci was quantified in (e). At least 200 cells and 1500 foci per condition were analyzed (mean ± SD, ****P < 0.0001; N = 3). Scale bars, 5 μm.

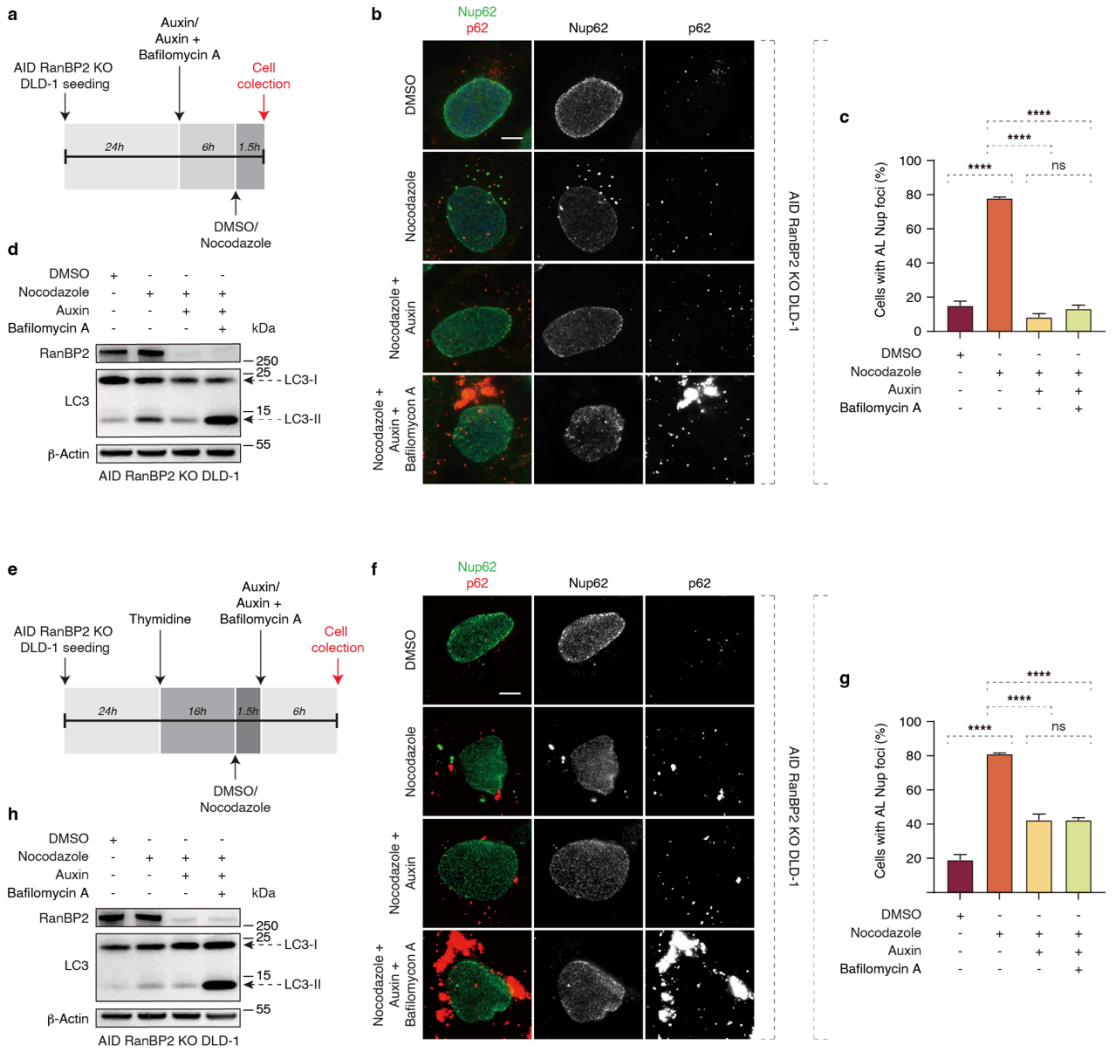

Extended Data Fig. 13. The role of RanBP2 in the formation and maintenance of AL is independent of autophagy.

a-d, Scheme of the experimental setup (a). AID-RanBP2 KO DLD-1 cells were treated with nocodazole (10 μM), auxin and bafilomycin at indicated timepoints. Cells were co-labelled with anti-Nup62 (green) and anti-p62 (red) antibodies. Representative images of cells are shown in (b). The number of cells with large AL foci were quantified in (c). (d) Shows the WB analysis of RanBP2 and LC3 under different conditions shown in (a). At least 200 cells per condition were analyzed (mean ± SD, ns: not significant, ****P < 0.0001; N = 3). Scale bars, 5 μm.

e-h, Scheme of the experimental setup (e). AID-RanBP3 KO DLD-1 cells were synchronized and arrested inS phase by thymidine treatment (16h). Subsequently, the cells were treated with nocodazole (10 μM), auxin and bafilomycin at indicated timepoints. Cells were co-labelled with anti-Nup62 (green) and anti-p62 (red) antibodies. Representative images of cells are shown in (f). The number of cells with large AL foci were quantified in (g). (h) Shows the WB analysis of RanBP2 and LC3 under different conditions shown in (e). At least 200 cells per condition were analyzed (mean ± SD, ns: not significant, ****P < 0.0001; N = 3). Scale bars, 5 μm.

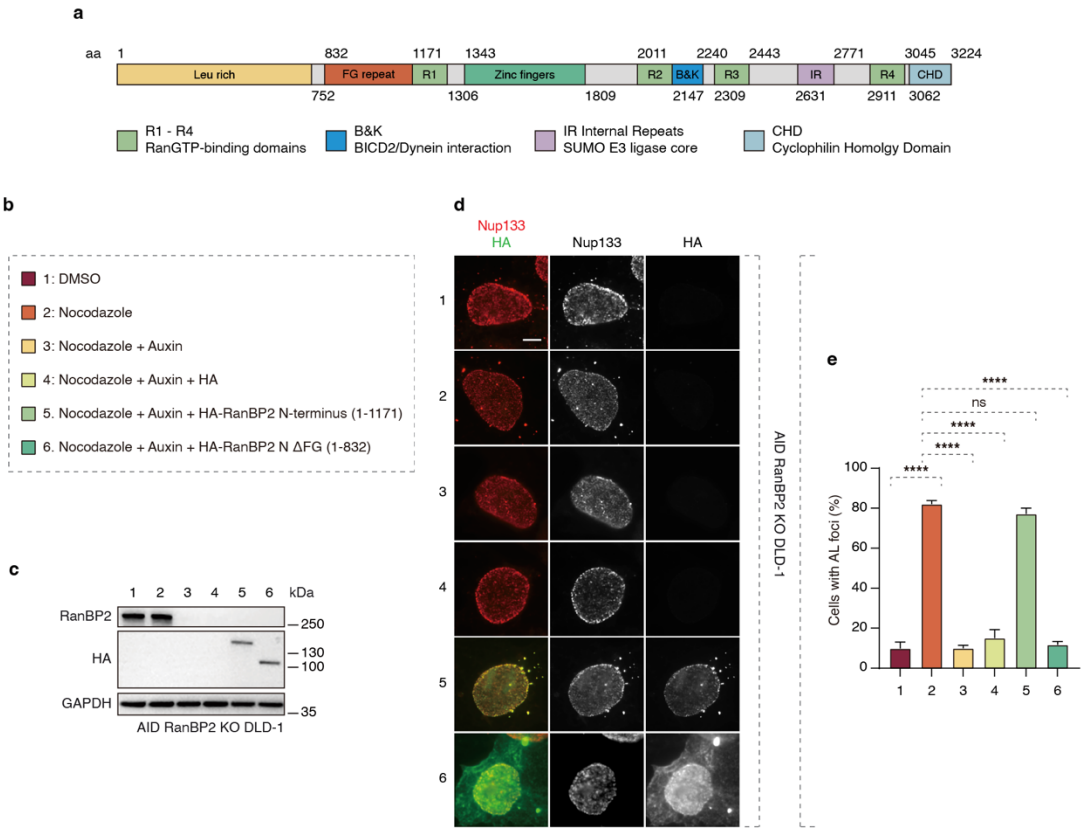

Extended Data Fig. 14. RanBP2 is specifically required for AL formation through its N-terminal FG repeat region,

a, Scheme of domain organization of RanBP2 protein. b-d, Different conditions of rescue experiments by indicated RanBP2 fragments (b). (c) Shows the WB analysis of RanBP2 fragments under different conditions indicated in (b). Representative images of AID-RanBP2 KO DLD-1 cells treated with the DMSO or auxin, transfected with different RanBP2 fragments and treated with nocodazole (10 μM) or DMSO (90 min). Cells were co-labelled with anti-Nup133 (red) and anti-HA (green) (d) antibodies. The number of cells with large AL foci was quantified in (e), and at least 300 cells per condition were analyzed (mean ± SD, ns: not significant, ****P < 0.0001; N = 3). Scale bars, 5 μm.

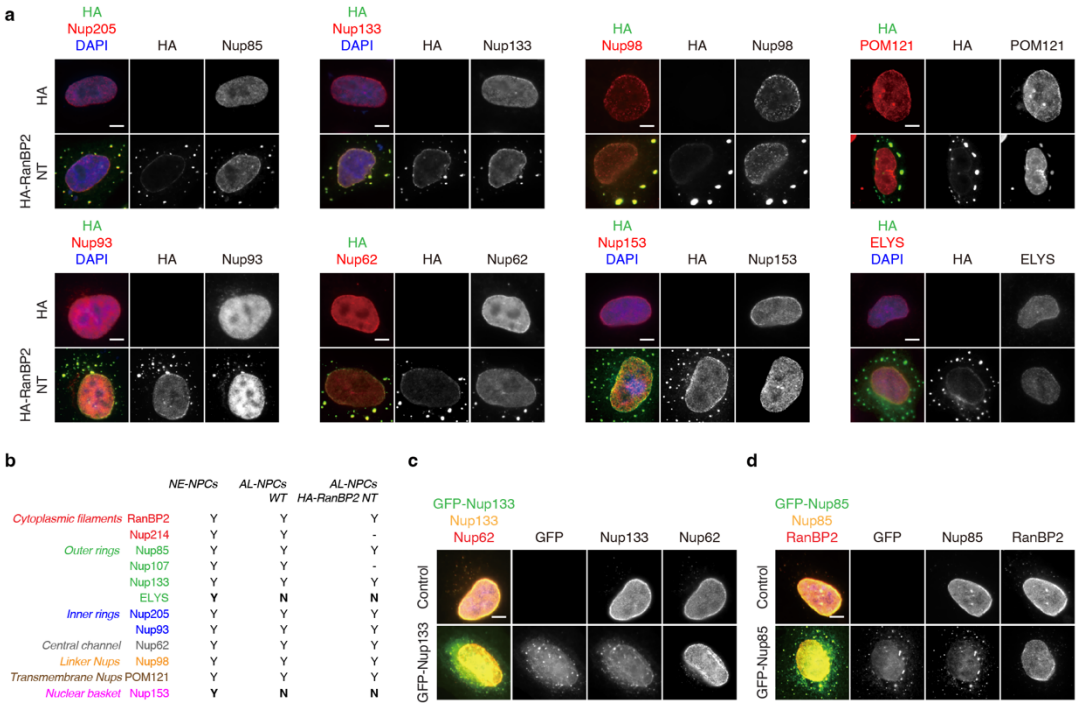

		NE-NPCs	AL-NPCs WT	AL-NPCs HA-RanBP2 NT
Cytoplasmic filaments	RanBP2	Y	Y	Y
	Nup214	Y	Y	-
Outer rings	Nup85	Y	Y	Y
	Nup107	Y	Y	-
	Nup133	Y	Y	Y
	ELYS	**Y**	**N**	**N**
Inner rings	Nup205	Y	Y	Y
	Nup93	Y	Y	Y
Central channel	Nup62	Y	Y	Y
Linker Nups	Nup98	Y	Y	Y
Transmembrane Nups	POM121	Y	Y	Y
Nuclear basket	Nup153	**Y**	**N**	**N**

Extended Data Fig. 15. Ectopic expression of NT RanBP2 is sufficient for AL formation.

a, Representative images of HeLa cells transfected with HA or HA-RanBP2 N-terminal (NT) fragment and labelled for Nups from different NPC subcomplexes as indicated. Cells were co-labelled with DAPI (blue), anti-Nups (red) and anti-HA (green) antibodies. Scale bars, 5 µm.

b, Summary of nucleoporin composition in NE-NPCs, ALC-NPCs and AL-NPCs-induced by RanBP2-NT expression. Different colors correspond to spefic NPC subcomplexes. “Y” indicates presence and “N” indicates absence of specific Nups and “-” indicates no available data.

c, Representative images of HeLa cells transfected with GFP-Nup133. Cells were co-labelled with Nup133 (yellow), and anti-Nup62 (red) antibodies. Scale bars, 5 µm.

d, Representative images of HeLa cells transfected with GFP-Nup85. Cells were co-labelled with Nup85 (yellow), and anti-RanBP2 (red) antibodies. Scale bars, 5 µm. Note that expression of RanBP2-NT but not Nup133 or Nup85 is sufficient to induce AL foci where multiple Nups localize to.

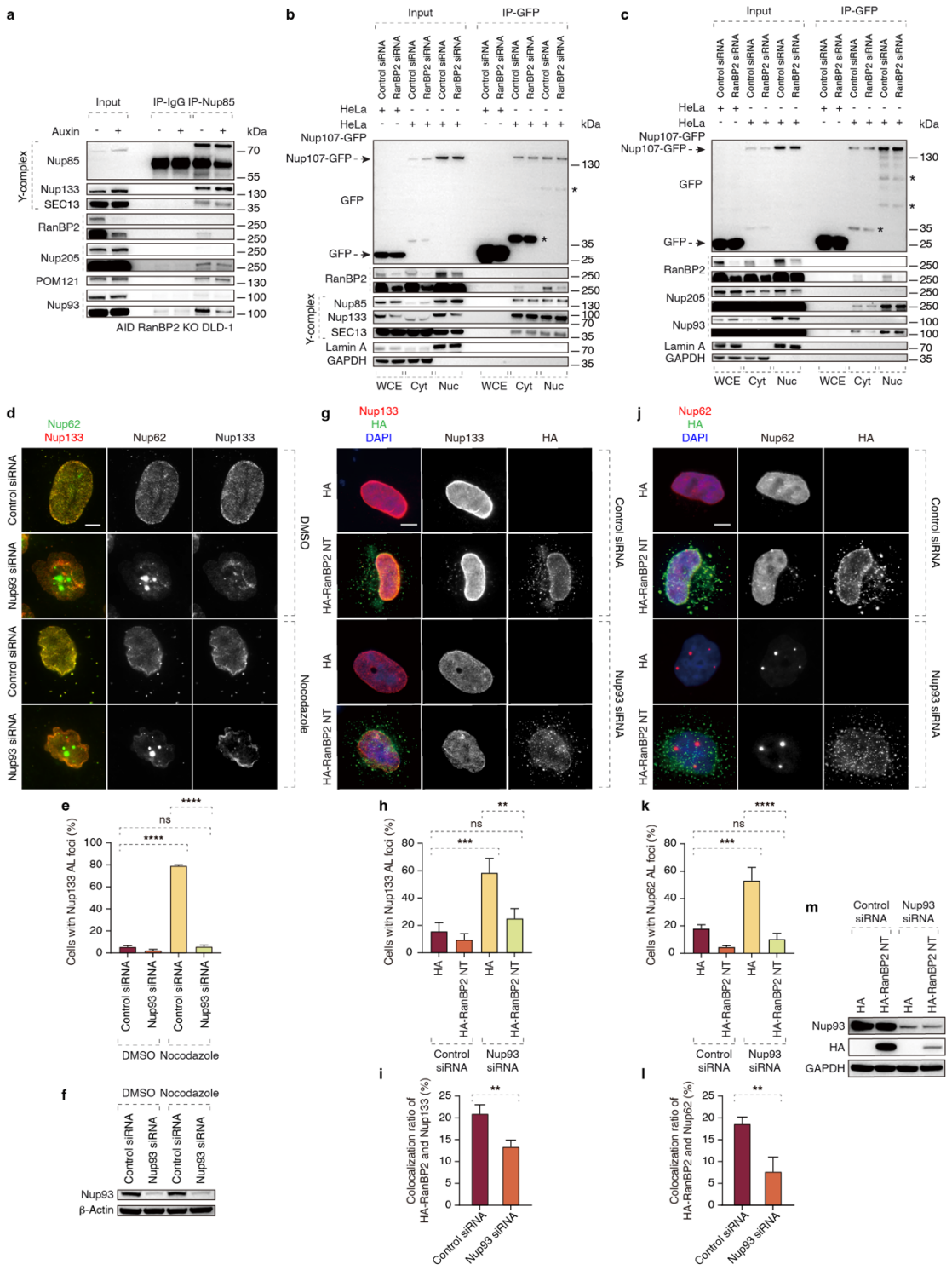

Extended Data Fig. 16. RanBP2 facilitates the assembly of cytosolic NPCs by promoting the interaction between Nup93 and the Y complex.

a, AID-RanBP2 KO DLD-1 cells treated with auxin to induce depletion of RanBP2 and lysates were prepared and immunoprecipitated using Nup85 antibody or IgG and analyzed by Western blot (at least 3 independent experiments).

b, c, Cytoplasmic or nuclear extracts of Hela cells expressing GFP or 2xZFN-mEGFP-

1576 Nup107 were immunoprecipitated using GFP-Trap A beads (GFP-IP) and analyzed by
1577 Western blot (at least 3 independent experiments).
1578 d, e, f, Representative images of HeLa cells treated with the indicated siRNAs (48h) and
1579 subsequently with nocodazole (10 μM) or DMSO (90 min). Cells were co-labelled with anti-
1580 Nup62 (green) and anti-Nup133 (red) (d) antibodies. The number of cells with large AL foci
1581 was quantified in (e) and at least 1000 cells per condition were analyzed (mean ± SD, ns:
1582 not significant, ****P < 0.0001; N = 3). (f) Shows the Western blot analysis of Nup93 under
1583 indicated conditions. Scale bars, 5 μm.
1584 g-m, Representative images of HeLa cells treated with the indicated siRNAs and
1585 transfected with HA or HA-RanBP2-NT fragment. Cells were co-labelled with anti-Nup133
1586 (red), anti-HA (green) antibodies and DAPI (blue) (g), or co-labelled with anti-Nup62 (red),
1587 anti-HA (green) antibodies and DAPI (blue) (j). The number of cells with large AL foci was
1588 quantified in (h, k) and the co-localization ratio of HA-RanBP2-NT and Nup62 was
1589 quantified in (i, l), and at least 300 cells per condition were analyzed (mean ± SD, **P <
1590 0.01; ***P < 0.001; N = 3). Scale bars, 5 μm. (m) Shows the WB analysis of Nup93 and
1591 HA-RanBP2-NT under indicated conditions.
1592

a

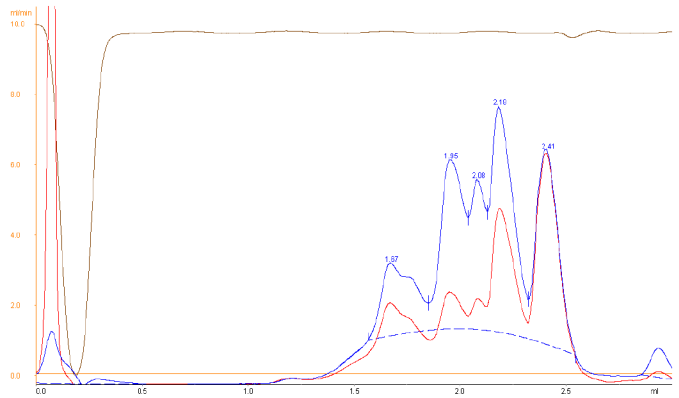

Component	Stoke's radius (A)	MW (Da)	Log MW	Volume (ml)
Thyroglobulin (bovine)	**86**	670,000	5.826	
g-globulin (bovine)	**51**	158,000	5.198	1.95
Ovalbumin (chicken)	**28**	44,000	4.643	2.08
Myoglobulin (horse)	**19**	17,000	4.23	2.18
Vitamin B12	**8.5**	1,350	3.13	2.41

b

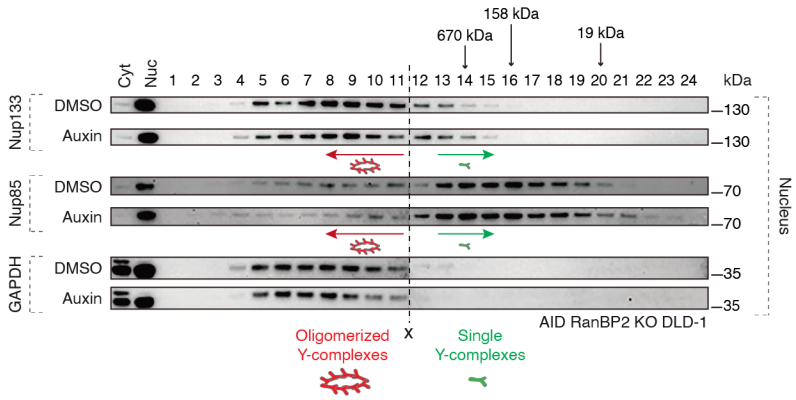

Extended Data Fig. 17. Deletion of RanBP2 does not inhibit the formation of Y complex oligomers in the nuclear extracts.

a, Calibration of the Superose 6 column was carried out with thyroglobulin (bovine), g-globulin (bovine), ovalbumin (chicken), myoglobulin (horse) and vitamin B12. The calibration profile and the molecular weights of the protein markers are indicated

b, Auxin-inducible degron (AID) RanBP2 KO DLD-1 cells were treated with DMSO or auxin for 4h to deplete RanBP2 and cytoplasmic fractions were prepared, separated on a Superose 6 gel filtration column and analyzed by Western blotting. Fraction 1 corresponds to the void and the elution of thyroglobulin (670 kDa), g-globulin (158 kDa) and myoglobulin markers 19 kDa are indicated. Green arrows point to fractions preferentially containing single Y-complexes, and red arrows indicate fraction with higher molecular weight, oligomerized Y-complexes. Note that depletion of RanBP2 did not affects the abundance of oligomerized Y-complexes.

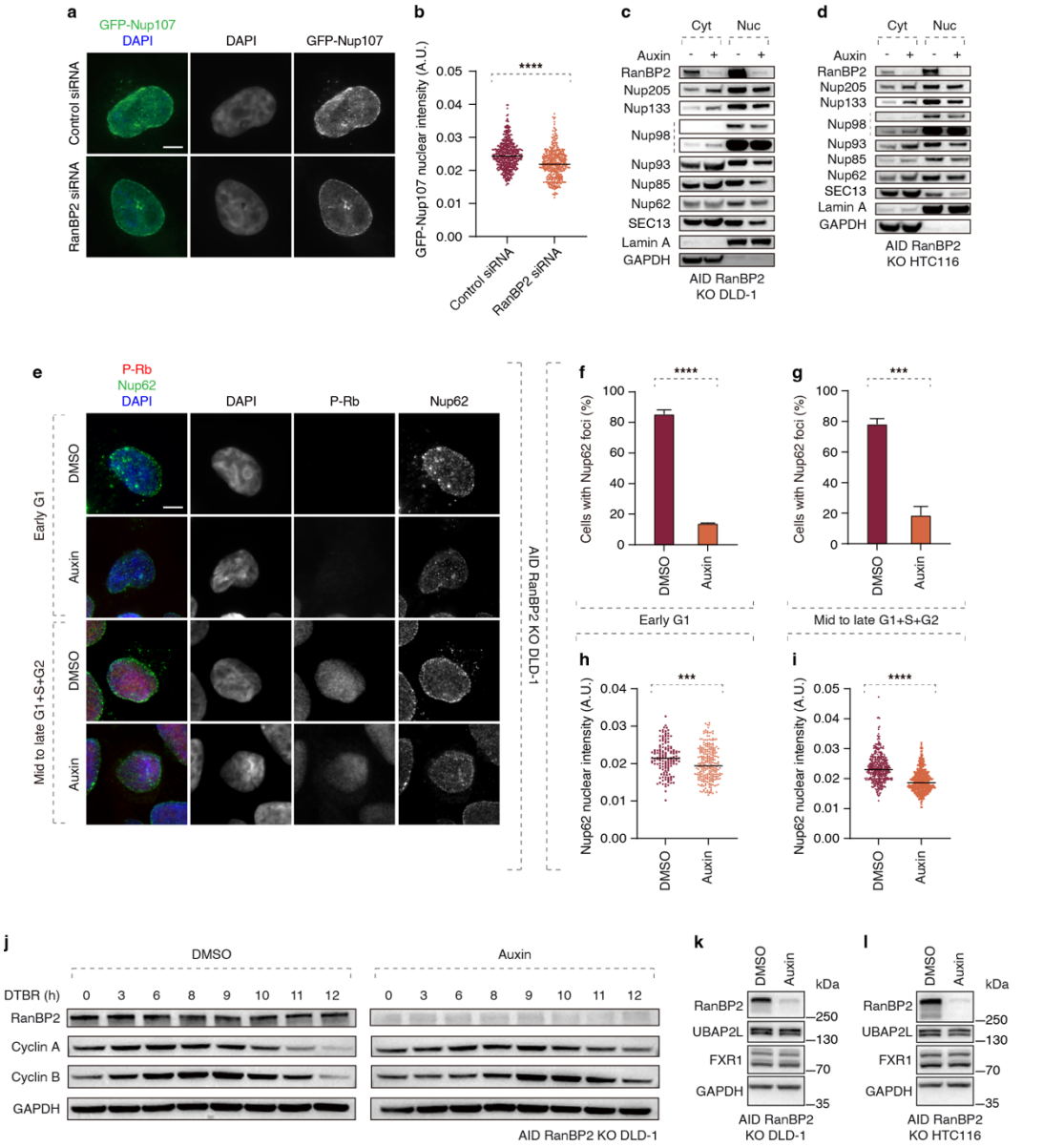

Extended Data Fig. 18. RanBP2 preserves the density of NPCs on the NE during interphase

a, b, Representative images of 2xZFN-mEGFP-Nup107 HeLa cells treated with RanBP2 siRNA (48h) (a). Cells were co-labelled with DAPI (blue). The intensity of GFP-Nup107 at the NE was quantified in (b), and at least 400 cell per condition were analyzed (mean ± SD, ****P < 0.0001; N = 3). Scale bars, 5 µm.

c, Auxin-inducible degron (AID) RanBP2 KO DLD-1 cells were treated with DMSO or auxin for 4h to deplete RanBP2 and cytoplasmic (Cyt) and nuclear (Nuc) fractions were prepared and levels of Nups were analyzed by Western blot (at least 3 independent experiments).

d, AID RanBP2 KO HTC116 cells were treated with DMSO or auxin for 4h to deplete RanBP2 and cytoplasmic (Cyt) and nuclear (Nuc) fractions were prepared and levels of

Nups were analyzed by Western blot (at least 3 independent experiments).

e-i, Representative immunofluorescence images depicting the localization of Nup62 in AID RanBP2 KO DLD-1 cells in different cell cycle stages. p-Rb was used to distinguish cells in early G1 (p-Rb–negative cells) and mid-late G1, S, and G2 (p-Rb–positive cells) stages. Nuclei were stained with DAPI (e). The percentage of cells with the AL foci in early G1 (f), and mid-late G1, S, G2 (g) was quantified. At least 300 cells per condition were analyzed (mean ± SD, ***P < 0.001; ****P < 0.0001; unpaired two-tailed t test, n = 3 independent experiments). The NE intensity of Nup62 in early G1 cells (h), and mid-late G1, S, G2 cells (i) was quantified. At least 150 cells per condition were analyzed (mean ± SD, ***P < 0.001; ****P < 0.0001; unpaired two-tailed t test, n = 3 independent experiments). Scale bars, 5 μm.

j, Protein levels of mitotic cyclins were analyzed by Western blot in AID RanBP2 KO DLD-1 cells treated with DMSO or auxin to induce depletion of RanPB2 and synchronized by double thymidine and block release at indicated timepoints.

k, l, Protein levels of FXR1 and UBAP2L were analyzed by Western blot in AID RanBP2 KO DLD-1 cells treated with DMSO or auxin to induce depletion of RanPB2 (4h) and synchronized in early interphase.

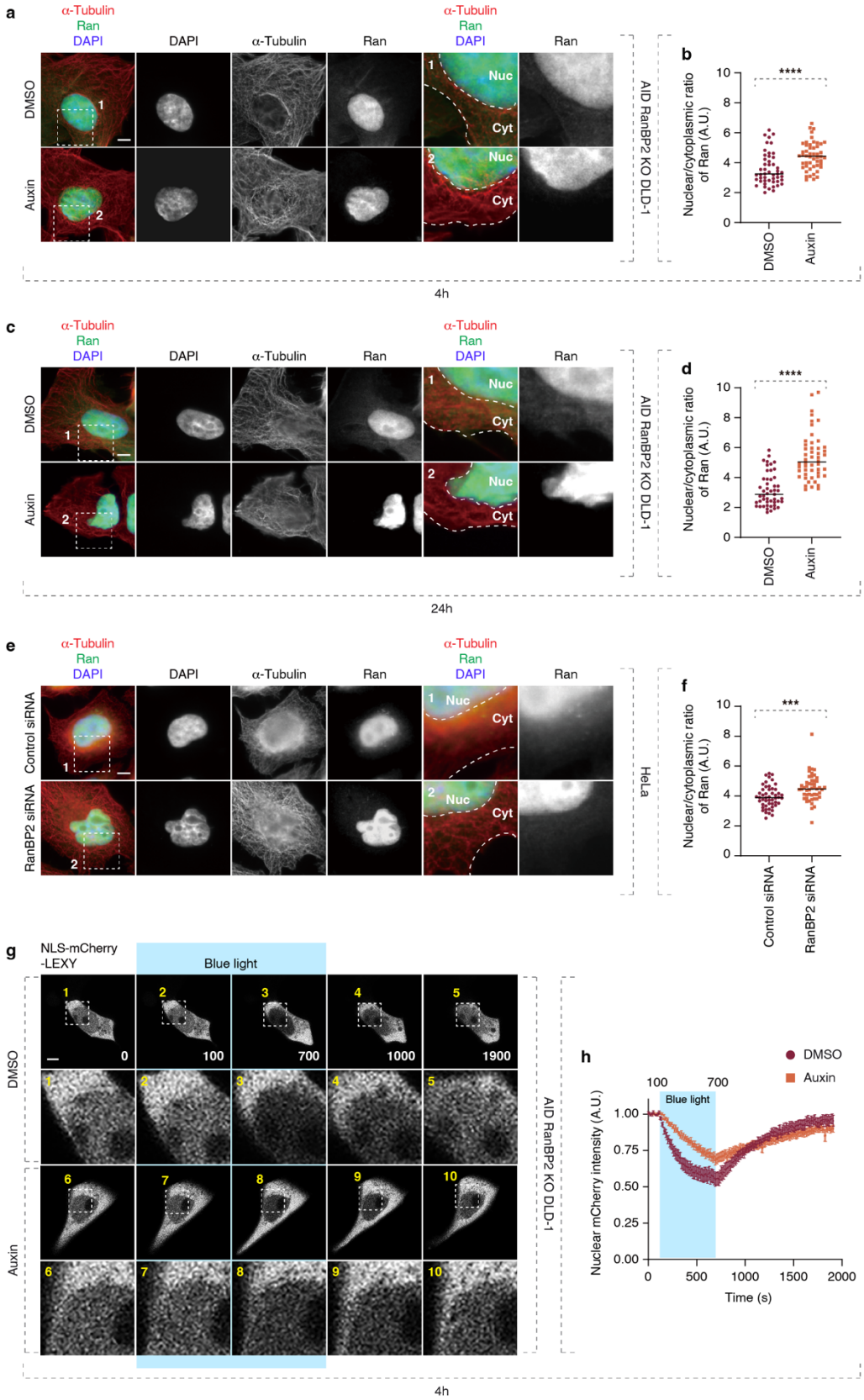

Extended Data Fig. 19. RanBP2 preserves nuclear pore function.

a, b, Representative immunofluorescence images depicting the nuclear (Nuc) and

cytoplasmic (Cyt) localization of Ran in asynchronously proliferating AID RanBP2 KO DLD-1 cells treated with DMSO or auxin (4h) to induce depletion of RanPB2. Cells were co-labelled with anti-Ran (green), anti-Tubulin (red) antibodies and DAPI (a). The magnified framed regions are shown in the corresponding numbered panels. The nuclear/cytoplasmic (N/C) ratio of Ran was quantified in (b). At least 100 cells per condition were analyzed (mean ± SD, ****P < 0.0001; unpaired two-tailed t test, n = 3 independent experiments). Scale bar, 5 μm.

c, d, Representative immunofluorescence images depicting the nuclear (Nuc) and cytoplasmic (Cyt) localization of Ran in asynchronously proliferating AID RanBP2 KO DLD-1 cells treated with DMSO or auxin (24h) to induce depletion of RanPB2. Cells were co-labelled with anti-Ran (green), anti-Tubulin (red) antibodies and DAPI (c). The magnified framed regions are shown in the corresponding numbered panels. The N/C ratio of Ran was quantified in (d). At least 100 cells per condition were analyzed (mean ± SD, ****P < 0.0001; unpaired two-tailed t test, n = 3 independent experiments). Scale bar, 5 μm.

e, f, Representative immunofluorescence images depicting the nuclear (Nuc) and cytoplasmic (Cyt) localization of Ran in asynchronously proliferating WT and RanBP2 KD (RanBP2 siRNA 48h) HeLa cells. Cells were co-labelled with anti-Ran (green), anti-Tubulin (red) antibodies and DAPI (e). The magnified framed regions are shown in the corresponding numbered panels. The N/C ratio of Ran was quantified (f). At least 100 cells per condition were analyzed (mean ± SD, ***P < 0.001; unpaired two-tailed t test, n = 3 independent experiments). Scale bar, 5 μm.

g, h, Representative immunofluorescence images depicting nuclear fluorescence NLS-mCherry-LEXY shuttling reporter expressed in AID RanBP2 KO DLD-1 cells treated with DMSO or auxin (4h) to induce depletion of RanPB2 (g). Cells were incubated in the dark for 100 s before blue light irradiation for 600 s was applied, which was followed by a 1200 s dark-recovery phase. Time is indicated in seconds. Relative nuclear fluorescence was quantified in (h). At least 10 cells per condition were analyzed (mean ± SD, n = 3 independent experiments).

1673

Extended Data Fig. 20

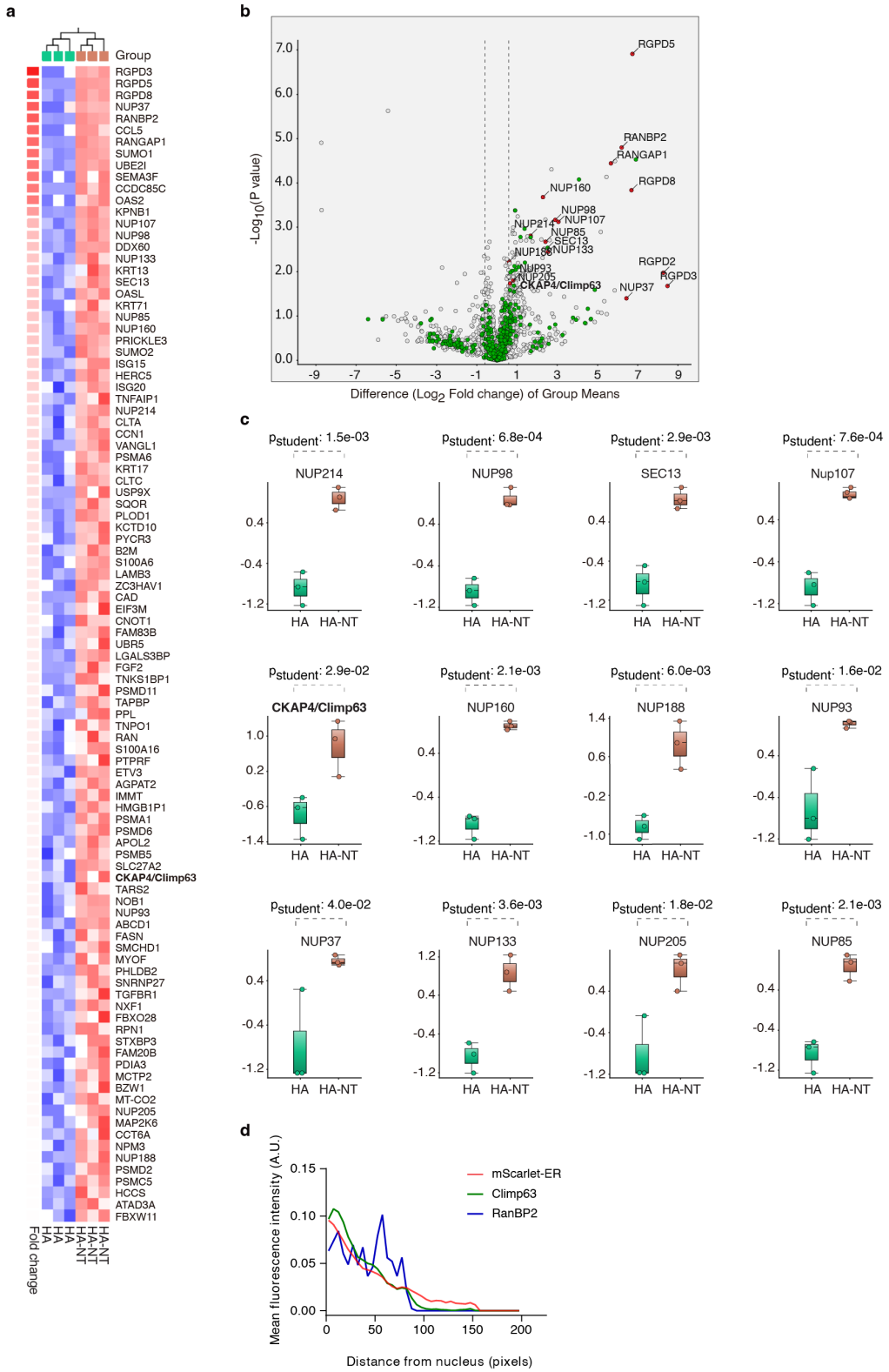

1674

1675

1676 **Extended Data Fig. 20. RanBP2-dependent AL interactome.**

1677 a, b, Liquid chromatography-mass spectrometry (LC-MS) was used to identify proteins

1678 interacting with HA-tagged NT-RanBP2 and the HA-tag as a negative control. A heatmap

displays the proteins that showed a change greater than 1.5-fold with a p-value of less than 0.05 between the two groups (a). Volcano plot for the comparison between the two groups (b). The cutoff values fold change >1.5 and FDR < 0.05 were utilized to identify differentially interacting protein. Red represents a group of NPC-related proteins and green depicted ER-related factors. Box plots of selected Nups and Climp63 (CKAP4).

d, Intensity profiles per distance from the nucleus of three fluorescent channels shown in Fig. 5d corresponding to ER marker plasmid mScarlet-ER, Climp63 (green) RanBP2 (blue).